

MICROCOPY RESOLUTION TEST CHART
NATIONAL BUREAU OF STANDARDS 1963 A

8

AD-A180 131

Prevention of Primary Mirror Contamination by Helium Purging

R. R. HERM, B. R. JOHNSON, and S. J. YOUNG
Chemistry and Physics Laboratory
Laboratory Operations
The Aerospace Corporation
El Segundo, CA 90245

27 February 1987

Prepared for
SPACE DIVISION
AIR FORCE SYSTEMS COMMAND
Los Angeles Air Force Station
P.O. Box 92960, Worldway Postal Center
Los Angeles, CA 90009-2960

DTIC
ELECTRONIC
MAY 11 1987

APPROVED FOR PUBLIC RELEASE
DISTRIBUTION UNLIMITED

This report was submitted by The Aerospace Corporation, El Segundo, CA 90245, under Contract No. F04701-85-C-0086-P00016 with the Space Division, P.O. Box 92960, Worldway Postal Center, Los Angeles, CA 90009-2960. It was reviewed and approved for The Aerospace Corporation by S. Feuerstein, Director, Chemistry and Physics Laboratory.

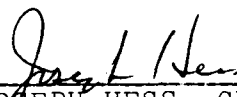
Capt Kevin O'Brien, SD/CNS, was the project officer for the Mission-Oriented Investigation and Experimentation (MOIE) Program.

This report has been reviewed by the Public Affairs Office (PAS) and is releasable to the National Technical Information Service (NTIS). At NTIS, it will be available to the general public, including foreign nationals.

This technical report has been reviewed and is approved for publication. Publication of this report does not constitute Air Force approval of the report's findings or conclusions. It is published only for the exchange and stimulation of ideas.



KEVIN O'BRIEN, Capt, USAF
MOIE Project Officer
SD/CNS



JOSEPH HESS, GM-15
Director, AFSTC West Coast Ofc
AFSTC/WCO OL-AB

REPORT DOCUMENTATION PAGE

1a. REPORT SECURITY CLASSIFICATION Unclassified		1d. RESTRICTIVE MARKINGS AD - A180131	
2a. SECURITY CLASSIFICATION AUTHORITY		3. DISTRIBUTION/AVAILABILITY OF REPORT Approved for public release; distribution unlimited.	
2b. DECLASSIFICATION/DOWNGRADING SCHEDULE		5. MONITORING ORGANIZATION REPORT NUMBER(S) SD-TR-87-17	
4. PERFORMING ORGANIZATION REPORT NUMBER(S) TR-0086A(2945-08)-1		7a. NAME OF MONITORING ORGANIZATION Space Division	
6a. NAME OF PERFORMING ORGANIZATION The Aerospace Corporation Laboratory Operations	6b. OFFICE SYMBOL (If applicable)	7b. ADDRESS (City, State and ZIP Code) Los Angeles Air Force Station Los Angeles, CA 90009-2960	
6c. ADDRESS (City, State and ZIP Code) El Segundo, CA 90245		9. PROCUREMENT INSTRUMENT IDENTIFICATION NUMBER F04701-85-C-0086-P00016	
8a. NAME OF FUNDING/SPONSORING ORGANIZATION Space Division	8b. OFFICE SYMBOL (If applicable)	10. SOURCE OF FUNDING NOS.	
8c. ADDRESS (City, State and ZIP Code) Los Angeles, CA 90009-2960		PROGRAM ELEMENT NO.	TASK NO.
11. TITLE (Include Security Classification) Prevention of Primary (see 11 over)		PROJECT NO.	WORK UNIT NO.
12. PERSONAL AUTHOR(S) Herm. Ronald R., Johnson, Bernard R., Young, Stephen J.			
13a. TYPE OF REPORT	13b. TIME COVERED FROM _____ TO _____	14. DATE OF REPORT (Yr., Mo., Day) 1987 February 27	15. PAGE COUNT 107
16. SUPPLEMENTARY NOTATION			
17. COSATI CODES		18. SUBJECT TERMS (Continue on reverse if necessary and identify by block number)	
FIELD	GROUP	SUB. GR.	
			Cryogenic Optics, Molecular Gas Dynamics
			Helium Purge Monte Carlo Calculation
			Mirror Contamination; Spacecraft Contamination
19. ABSTRACT (Continue on reverse if necessary and identify by block number) Telescopes mounted on space platforms may be subject to performance degradation by the condensation of gaseous species on cryogenically cooled optical surfaces. Attenuations of the flux of impinging contaminants by a purging counterflow of helium (He) gas at the telescope entrance aperture have been calculated by a Monte Carlo procedure that follows individual trajectories selected at random. The calculations involve no significant approximations and should be quite accurate. In particular, multiple-collision trajectories are treated, employing the best available information on the atomic and molecular collision cross sections. Extensive calculations on protection of the Shuttle-mounted CIRRIS I and CIRRIS IA telescopes are presented which illustrate the extent of protection afforded.			
20. DISTRIBUTION/AVAILABILITY OF ABSTRACT UNCLASSIFIED/UNLIMITED <input type="checkbox"/> SAME AS RPT. <input checked="" type="checkbox"/> DTIC USERS <input type="checkbox"/>		21. ABSTRACT SECURITY CLASSIFICATION Unclassified	
22a. NAME OF RESPONSIBLE INDIVIDUAL		22b. TELEPHONE NUMBER (Include Area Code)	22c. OFFICE SYMBOL

11. (Continued) Mirror Contamination by Helium Purging

CONTENTS

I. INTRODUCTION..... 5

II. PROCEDURE..... 7

 A. Helium Flow Field..... 9

 B. Collision Cross Sections..... 10

 C. Monte Carlo Calculations..... 14

III. ESTIMATED CONTAMINATION LEVEL..... 21

 A. Cryodeposit Buildup Rate..... 26

 B. Significant Cryodeposit Thickness..... 32

IV. MONTE CARLO HELIUM-PURGE EFFICIENCY RESULTS..... 35

V. CONTAMINANT BUILDUP RATE AND CONCLUSIONS..... 51

REFERENCES..... 61

APPENDIX..... 65

DTIC
COPY
INSPECTED
7

Accession For

NTIS	<input checked="" type="checkbox"/>
DTIC	<input type="checkbox"/>
Unannounced	<input type="checkbox"/>
Justification	<input type="checkbox"/>

AT

FIGURES

1.	Purge Geometry for CIRRIIS I.....	8
2.	Measured and Modeled Centerline Number Densities for Subscale Ar Ring Injection.....	11
3.	Calculated Total Cross Sections for Scattering of He from H ₂ O, CO ₂ , N ₂ , O, and CO as a Function of Relative Collision Speed v.....	13
4.	Plots of $P_c = (2\pi/\sigma) \int_0^\theta \sigma(\theta') \sin\theta' d\theta'$ for He + CO ₂ for Three Relative Collision Speeds v.....	17
5.	Parametric Fit (Scattering Parameter) of $\cos \theta = 1 - 2P_c^n$ for He + H ₂ O, He + N ₂ , and He + CO ₂	19
6.	Histogram of H ₂ O Deposition along the CIRRIIS I Sensor Wall.....	36
7.	Normal View of Sensor Apertures.....	33
8.	Transmission of H ₂ O Contaminant as a Function of He Flow Rate \dot{m} , for Runs 34, 43, 44, 56, and 57.....	39
9.	Transmission of H ₂ O Contaminant as a Function of Steady-State He Density in the Sensor, for Runs 44 through 47.....	40
10.	Transmission of H ₂ O Contaminant as a Function of He Flow Rate for Two Impingment Speeds v_c , for Runs 33 through 36, 43, and 44.....	42
11.	Transmission of H ₂ O versus v_c , for Runs 33, 34, 37, 38, 50, and 58.....	43
12.	Transmission versus v_c for H ₂ O and N ₂	44
13.	Thermally Averaged $\bar{\tau}$ for H ₂ O, Obtained by Averaging the $\tau(v_c)$ Behavior Shown in Fig. 11 over a Thermal Speed Distribution.....	46
14.	Transmission and Acceptance versus γ for H ₂ O, for Runs 33 and 64 through 67.....	47
15.	Acceptance versus γ for N ₂ , for Runs 39, 52, 53, 59 through 63, and 69.....	48

FIGURES (Continued)

16.	Buildup of H ₂ O Contaminant-Film Thickness, Calculated from Eq. (17) for the STS-4 Worst-Case Environment Specified in Eq. (13) and Shown as \bar{t}	52
17.	The Acceptance η for N ₂ versus v_c for Runs 39, 49, 52, and 53.....	53
18.	Steady-State N ₂ Density within CIRRIS IA versus β from Eq. (12) for $f_{N_2}(\beta)$ from Eq. (14) and $B_{N_2}'(\beta)$ from Eq. (22).....	54
19.	Growth Rate of N ₂ on the CIRRIS IA Primary Mirror, Calculated from Eq. (20), for the n_{ss} Dependence Plotted in Fig. 18.....	55

TABLES

1.	Estimates of H ₂ O Flux Impinging on the CIRRIS IA Aperture.....	23
2.	Summary of All He Purge Efficiency Calculations.....	28
3.	Worst-Case Estimates of H ₂ O and N ₂ Growth Rates on the CIRRIS IA Primary Mirror Due to the 25-lb-Thrust VCS Engine.....	57
4.	Best Estimates of N ₂ Growth Rates on the CIRRIS IA Primary Mirror Due to the 25-lb-Thrust VCS Engine.....	58

I. INTRODUCTION

The interference by molecular contaminants in the environment to the proper performance of space-based infrared telescopes mounted on the Shuttle Orbiter has been discussed by a number of authors.¹ Contaminants include natural atmospheric species, primarily oxygen (O) atoms at Shuttle altitudes, as well as molecules released by the Shuttle. These include water (H₂O), nitrogen (N₂), oxygen (O₂), carbon monoxide (CO), carbon dioxide (CO₂), other trace molecular species, and hydrogen (H₂) and helium (He), although these latter two will not normally interfere with the telescope's operation. Potential interference effects include background radiation from excited molecules (and possibly from interactions of O atoms with surfaces, i.e., "Shuttle glow"), as well as degradation in optical performance due to condensation on sensitive optical components, specifically the cryogenically cooled primary mirror. The objective of the work reported here was to analyze the degree to which a purge flow of incondensable He gas could protect against such contamination of the primary mirror of the AFGL CIRRIS (Air Force Geophysics Laboratory Cryogenic Infrared Radiance Instrument for Shuttle) telescope.

Either He or neon (Ne) could potentially be used as the incondensable purge gas. Although Ne should have better efficiency by virtue of its higher mass, He has been the gas chosen in virtually all discussions, analyses, and implementations of the purge concept to date. One practical reason in the case of CIRRIS is the use of a liquid He cryogen so that the He gas is already available at flow rates^a \dot{m} up to 0.02 g/sec. Early analyses of the He purge concept, reviewed in Refs. 2 through 4, demonstrated its feasibility, but were too approximate to calculate or measure its efficiency reliably. These early analyses had to assume a simple hard-sphere differential

^aActually, the rate of gaseous He boil-off from the cryogen is considerably faster, but only 10% of that gas is used in the He purge flow in the current CIRRIS design.

scattering cross section. Accurate differential cross sections $\sigma(\theta)$ for the scattering of He atoms by O atoms reported in Ref. 3 show properties very different from the simple hard-sphere approximations. References 4 and 5 provide the only analyses that use the accurate He-O scattering cross sections calculated in Ref. 3. Because it formulates the problem in terms of scattered O atoms that miss the mirror rather than those that hit it, Ref. 4 avoids the unrealistic limit of only partial purge efficiency, even in the limit of infinite He density which appears in Ref. 5. However, both calculations employ a single-collision approximation and are, consequently, invalid at high purge-flow conditions.

The goal of the present study is to calculate the He purge-flow efficiency without the limitations of the previous studies. Specifically, a Monte Carlo calculation is made of the efficiency of the He purge, as a function of He gas flow rate \dot{m} , in protecting the primary mirror. The calculation is valid for any arbitrary number of collisions between He atoms and an incoming contaminant atom or molecule. The best available information is used to calculate highly reliable scattering cross-section functions, and purge protection is calculated for impinging contaminant molecules released from the Shuttle Orbiter, as well as for impinging atmospheric O atoms.

II. PROCEDURE

Calculations were done for the CIRRIS I and CIRRIS IA telescopes. The geometry, taken from Ref. 4, is shown in Fig. 1 for CIRRIS I. The computer code developed in this study can treat the case of He injection within the telescope, or He ejection from orifices in front of the telescope that make any angle ω with the sensor axis. All calculations reported here were done for the purge apparatus used on CIRRIS I and CIRRIS IA, an injector ring, with $\omega = 30^\circ$, about the circumference of the sensor entrance aperture. A plane wave of incident contaminant molecules of mass m_c approaches the sensor with speed v_c at an angle γ to the sensor axis. The purpose of the He purge gas is to deflect incoming contaminants that would otherwise hit the mirror at the rear of the sensor. Detailed analyses are presented for N_2 and H_2O , the two most troublesome contaminant species. Contaminant molecules may collide with He gas within the telescope and in the "plume," i.e., in front of the telescope. However, He density falls off rapidly in the plume with increasing distance from the sensor. In these calculations, collisions were considered within a hemispherical plume region of 100 cm radius centered on the sensor aperture.

The temperature of the CIRRIS primary mirror is 20 K; an analysis presented later in this report indicates that even N_2 will condense at this temperature. The temperature of the walls of the CIRRIS telescope varies from about 20 K near the primary mirror to about 40 K near the sensor aperture. Contaminants such as N_2 , which condense only at very low temperature, will not condense along the telescope wall except at the back near the primary mirror. On the other hand, the vapor pressure of H_2O is negligible even at 40 K. Accordingly, it was assumed that an impinging H_2O molecule sticks to the first surface it hits, mirror or wall. This same assumption has been made in all previous treatments of the He purge concept. It should be noted that a record of the profile of contaminant deposition along the sensor wall was kept for all calculations reported here. Consequently, it would be possible in the

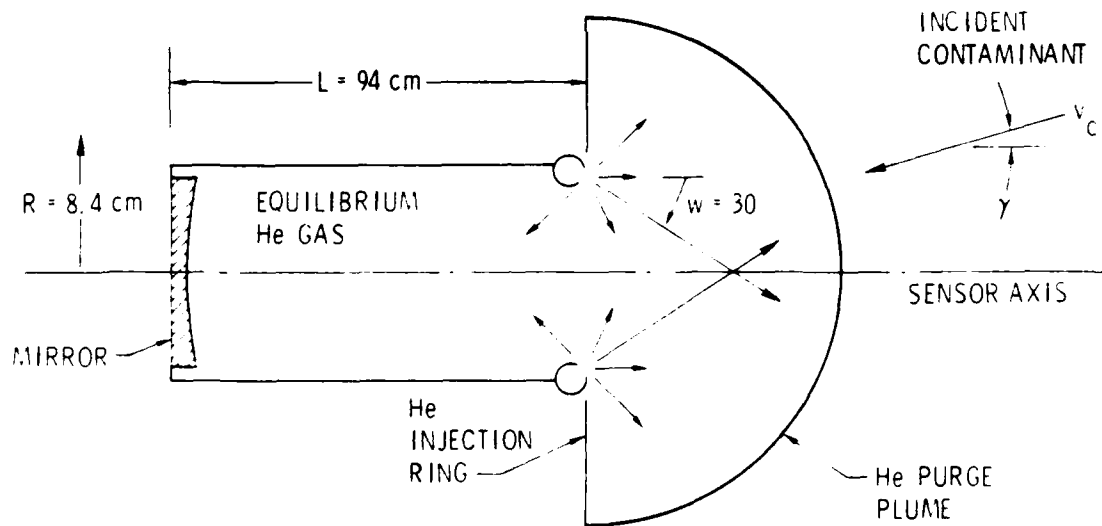


Fig. 1. Purge Geometry for CIRRS I

future to examine sensitivity to this assumption of a sticking coefficient of unity by allowing contaminants to reflect, after partial accommodation, from various wall positions.

A. HELIUM FLOW FIELD

The spatial dependence of the He number density and velocity distributions are necessary input functions for the calculations of the He purge efficiency. These functions were modeled by assuming thermal effusion of He from the ejection ring shown in Fig. 1. Perturbations of the flow field that resulted from He-He collisions outside of the ejection ring were ignored. Possible perturbations of the He flow field, which resulted from collisions with contaminants or atmospheric species, were also ignored. This latter condition should be an excellent approximation at the Shuttle Orbiter altitude, 380 km, planned by CIRRIS, although it could break down at much lower orbital altitudes.

The temperature of the He in the ejection ring in CIRRIS IA may vary from ~ 220 to 273 K. This relatively high temperature results because boil-off from the liquid-He cryogen is used as a coolant for an electronics box before it enters the ejector ring. Most of the calculations were carried out for a He ejection temperature T_{He} of 273 K. However, some calculations were carried out for a much lower ejection temperature, $T_{He} = 20$ K, in order to examine the sensitivity of He purge efficiency to ejection temperature.

At any point in the plume, the He number density was computed by summing the effusion contribution from sources on the circumference of the ejection ring and effusion from the sensor entrance aperture. The He number density within the sensor, assumed to be a constant within the sensor volume, was calculated by equating rates of effusion into and out of the sensor aperture. In order to save computer time and render the purge problem computationally tractable, all effusing He was assumed to move at an average thermal speed of

$$\bar{v}_{He} = (8 kT/m_{He})^{1/2} \quad (1)$$

Within the plume, the distribution in directions of He motion was obtained by summing all effusion contributions. As noted above, there is a distribution in temperatures within the sensor. In treating the He flow field, however, this was treated as one temperature, T_w . The distribution in speeds within the plume could be bimodal, corresponding to the sensor and ejection-ring temperatures. The speed distribution anywhere within the sensor consisted of He moving at \vec{v}_{He} from Eq. (1), with a random distribution in directions.

Figure 2 shows a comparison between the predictions of this number density model and measurements reported in Ref. 4 for a 0.0405-g/sec ring ejection of 300 K argon (Ar) gas in a 1/1.78-scale CIRRIS I model. The agreement at large distances is encouraging because model and measurements are steady-state results for the same mass flow rate \dot{m} , so that the integrals of the net outward flux, over any bound surface containing the aperture, have to be equal. The discrepancy at smaller distances might be due to noneffusive real source flow, purge-purge collisions in the real flow, as well as experimental error. The approximation of effusive flow from the orifices in the ejector ring would result in the largest uncertainty in He densities in this region, i.e., within and immediately in front of the sensor aperture. In order to examine the sensitivity of purge efficiency results to He flow-field uncertainties, calculations were actually carried out as a function of the steady-state density, denoted N_{He} , of He within the sensor. Additional sensitivity studies could be carried out by examining noneffusive source flow velocity distributions. However, this was not pursued because the effect should be very small in comparison to uncertainties introduced by the approximate treatment of the CIRRIS IA geometry, which is discussed later.

B. COLLISION CROSS SECTIONS

A contaminant or atmospheric species changes speed, usually slowing down, each time it collides with a He atom. The collision cross sections are needed for a wide range of relative collision speeds, $v = |\vec{v}_c - \vec{v}_{He}|$, in order to follow many collisions between incoming contaminants and He purge atoms. Differential and total cross sections

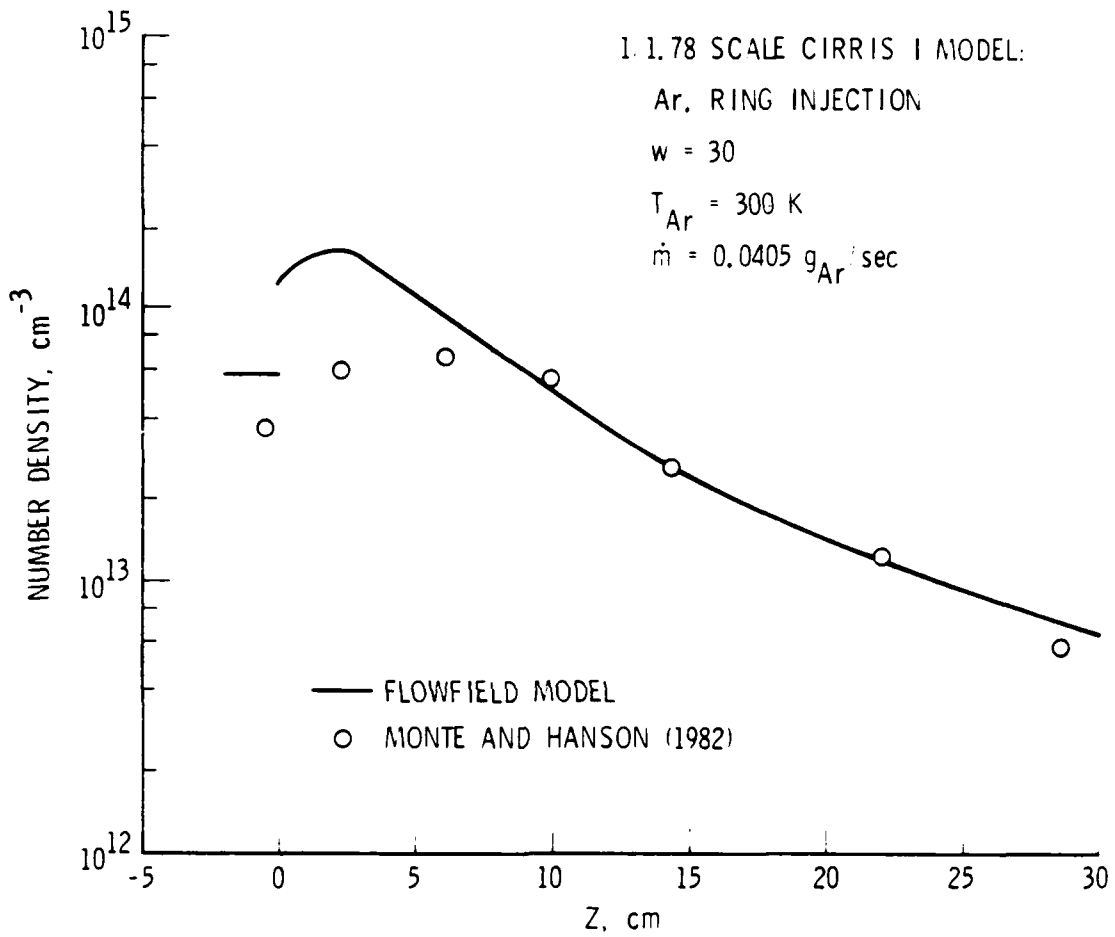


Fig. 2. Measured (Ref. 4) and Modeled (see text) Centerline Number Densities for Subscale Ar Ring Injection. $Z > 0$ measures distance in front of sensor aperture. Results for $Z < 0$ indicate values within the sensor.

$$\sigma(v) = 2\pi \int_0^{\pi} \sigma(\theta, v) \sin\theta d\theta \quad (2)$$

for the scattering of O atoms from He atoms were calculated in Ref. 3 by solving the quantum mechanical Schrodinger equation for the best information available in the literature on the central force interaction potential $V(r)$. Sensitivity analyses reported in Ref. 3 illustrate inconsequential errors in $\sigma(\theta, v)$ and $\sigma(v)$ that result from the assumption of a single central force potential and from possible errors in the potential function. The literature indicates that the interaction potentials between He and the molecules CO,⁶ N₂,⁶ and H₂O⁷ are only weakly anisotropic. To an excellent approximation, they can be analyzed as isotropic systems; i.e., the interaction potential is assumed to depend only on r and not on the orientation (central field approximation) of the molecule. The total and differential scattering cross sections for these "isotropic cases" (i.e., He + N₂, He + CO, and He + H₂O) were calculated quantum mechanically by means of the standard techniques described in Ref. 3. Results for the total scattering cross section are shown in Fig. 3. Appendix A provides plots of the differential cross sections and describes the interaction potentials used.

The He + CO₂⁸ system is strongly anisotropic, and the "central field approximation" could not be used in the present study. The differential cross section in this case was calculated by means of the infinite order sudden (IOS) approximation.⁹ The interaction potential $V(r, \alpha)$ is a function of the separation distance r and the angle α between the line of center and the axis of the CO₂ molecule. In the IOS approximation, α is regarded as a parameter and not a dynamical variable. For a fixed value of the parameter α , the potential is a function only of r and is thus "isotropic." This "isotropic" scattering problem, for a fixed α , is then solved by the partial-wave method to obtain a differential cross section $\sigma(\theta, \alpha)$, which is also a function of the parameter α . It has been shown elsewhere⁹ that the desired "total" (elastic plus inelastic) differential scattering cross section is, to an excellent approximation, given simply by the orientation average over α :

$$\sigma(\theta) = \frac{1}{2} \int_0^{\pi} \sigma(\theta, \alpha) \sin(\alpha) d\alpha \quad (3)$$

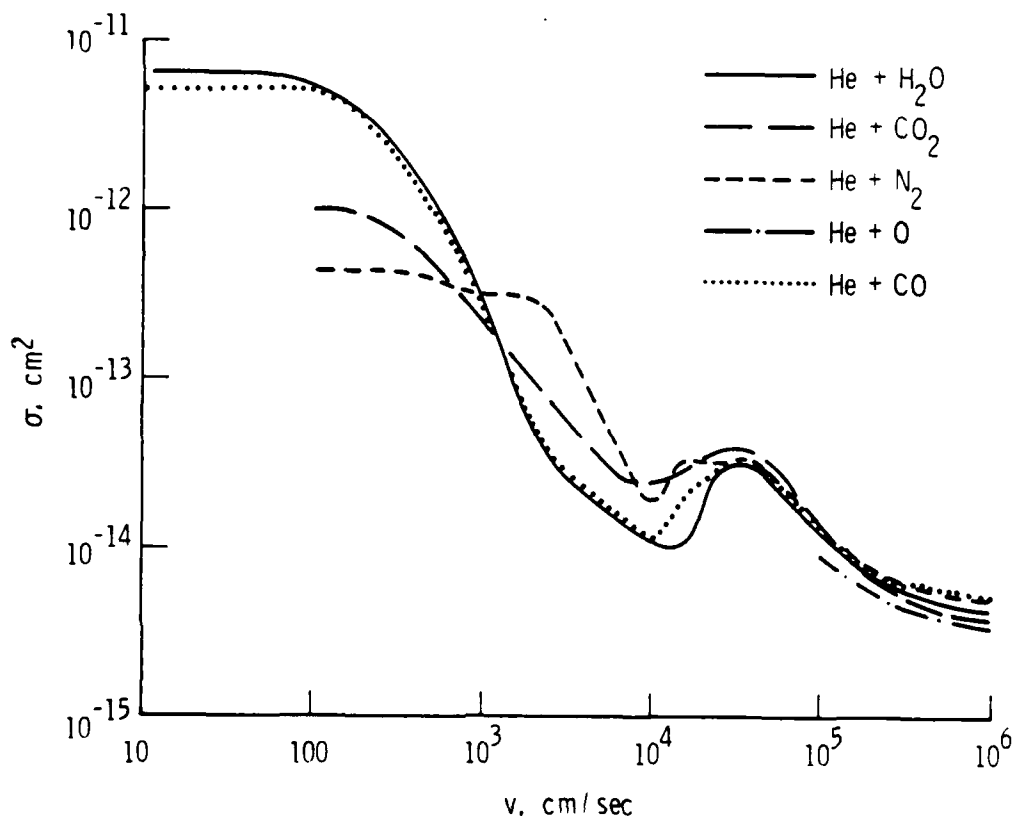


Fig. 3. Calculated Total Cross Sections for Scattering of He from H_2O , CO_2 , N_2 , O , and CO as a Function of Relative Collision Speed v

In the present work, the above integral was calculated numerically by means of the trapezoidal rule, with an integration spacing of $\Delta\alpha = 22.5^\circ$. By making use of symmetry, the integration range was reduced from 0 to π to 0 to $\pi/2$. Thus, four separate partial-wave calculations to compute $\sigma(\theta, \alpha_1)$ for $\alpha_1 = 22.5^\circ, 45^\circ, 67.5^\circ,$ and 90° ($\alpha = 0^\circ$ need not be calculated because of the $\sin\alpha$ factor) were calculated to obtain each differential scattering cross-section curve for He + CO₂, shown in Appendix A. Again, the total scattering cross-section results are shown in Fig. 3.

C. MONTE CARLO CALCULATIONS

A Monte Carlo calculation was made for contaminant molecules impinging at angle γ with speed v_c (see Fig. 1). The transmission

$$\tau = \frac{\text{number of contaminants striking mirror with He flow}}{\text{number of contaminants entering sensor without He flow}} \quad (4)$$

is the quantity of interest in analyzing readily condensible contaminants, such as H₂O. For contaminants that condense only at the primary mirror, viz N₂, the quantity of interest is the sensor acceptance

$$\eta = \frac{\text{number of contaminants entering sensor with He flow}}{\text{number of contaminants entering sensor without He flow}} \quad (5)$$

The Monte Carlo technique is a well-known procedure¹⁰⁻¹³ wherein unspecified parameters are chosen at random, and a large number of individual trajectories of contaminants are followed as they transverse the He flow field, in order to provide a statistically reliable result.

Specifically, the calculation placed a control surface normal to the impingement direction in front of the sensor at a point where the He plume density was $\sim 1\%$ of its centerline value at the sensor aperture. The area of the control surface through which the contaminants impinged was typically twice that of the sensor aperture, in order to allow for scattering of contaminants into, as well as out of, the sensor aperture. A record was kept for each calculation of the number of trajectories where the He actually

scattered an impinging contaminant into the sensor aperture. This was always a small fraction of the trajectories, a fact confirming that the control surface area was sufficient to account for this effect. This was further verified in a few calculations where other control areas were used.

The spatial position of the contaminant, as it crossed normal to the control surface, was chosen at random. The contaminant was allowed to move along a straight-line trajectory s for a distance l before a collision took place. The free path length l was calculated from the randomly chosen variable, $0 < x < 1$, as

$$\frac{1}{v_c} \int_0^l \langle v\sigma(v) \rangle n(\vec{r}) ds = -\ln x \quad (6)$$

where

$$\langle v\sigma(v) \rangle = \int_0^{\infty} v\sigma(v) \rho(v) dv \quad (7)$$

is the numerical average of the total collision rate constant over the probability density distribution in relative collision speed, viz, $\int_0^{\infty} \rho(v) dv = 1$. The quantity $\rho(v)$ has two forms -- one for outside the sensor, where the He velocity field is determined by effusive flow from the ejector ring and sensor aperture, and one for inside the sensor, where the He velocity field is random in direction. In both cases, $\rho(v)$ is for the mean-speed distribution approximation $f(v_{He}) = \delta(v_{He} - \bar{v}_{He})$. If the resultant straight-line trajectory corresponded to hitting the sensor wall, hitting the mirror, or exiting the He plume to free space, the result was recorded and the motion of the next incoming contaminant was followed.

If the solution for l resulted in a position in the He plume or in the He gas within the sensor, a collision had taken place. After the collision, the contaminant left this position on a new straight-line trajectory with a new velocity \vec{v}'_c , i.e., in a new direction and at a new speed, and the procedure was repeated to find a new trajectory length. First, however, the new contaminant velocity \vec{v}'_c was calculated from the old known contaminant

velocity \vec{v}_c by invoking conservation of energy and linear momentum in the collision. For this calculation it was necessary to specify the precollision direction of motion of the He atom involved in the collision, as well as the center-of-mass scattering angles, θ and ϕ , produced by the collision. A value for the azimuthal angle ϕ was chosen randomly, i.e.,

$$\phi = 2\pi x \quad (8)$$

The polar scattering angle θ was chosen by randomly selecting a cumulative scattering probability, i.e., by solving

$$P_c(\theta) = \frac{2\pi}{\sigma} \int_0^\theta \sigma(\theta') \sin\theta' d\theta' = x \quad (9)$$

for θ when x , as usual, is randomly chosen between 0 and 1. Rigorously, the He direction should be chosen randomly. This was done for collisions within the sensor. For collisions within the plume, however, the He direction was taken as the most probable one for that particular spatial position in order to reduce computation time. The effect of this approximation on the computation should be negligible.

In this manner, trajectories of a large number of impinging contaminants were followed to arrive at statistically significant results for τ and η . Each trajectory was made up of an arbitrary number of straight-line trajectories, with intervals between collisions determined randomly. After each collision, the new contaminant velocity was determined randomly, consistent with conservation of linear momentum and energy.

Equation (9) indicates that the differential cross section only enters the Monte Carlo calculation of τ through the cumulative scattering probability distribution $P_c(\theta)$. Figure 4 shows plots of this function for He + CO₂ for three different collision velocities. For all of the Monte Carlo calculations reported here, $P_c(\theta)$ was fit to

$$\cos\theta = 1 - 2P_c(\theta)^n, \quad n > 1 \quad (10)$$

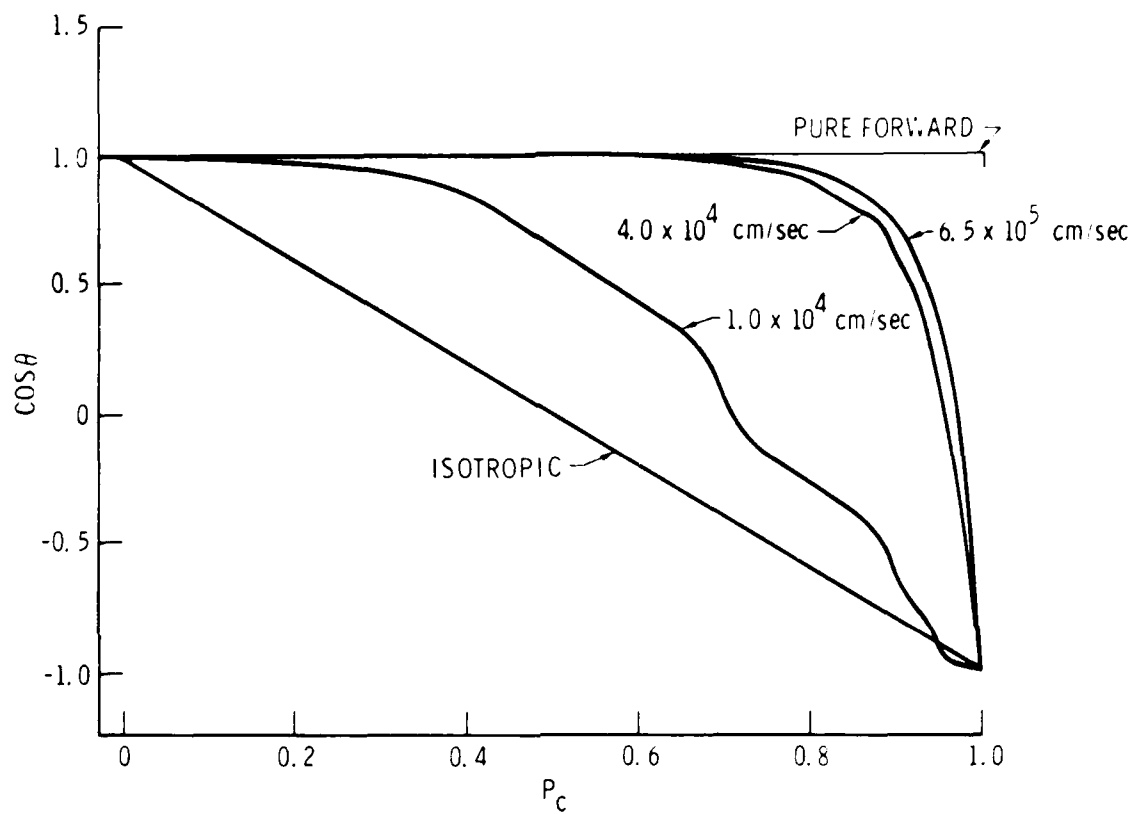


Fig. 4. Plots of $P_c = (2\pi/\sigma) \int_0^\theta \sigma(\theta') \sin\theta' d\theta'$ for He + CO₂ for Three Relative Collision Speeds v

As n goes to unity, the scattering would approach isotropic, hard-sphere scattering. As n goes to infinity, the scattering is more and more closely confined to a region around 0° . These two limiting scattering behaviors, isotropic and pure forward, are also shown in Fig. 4. Figure 5 shows the dependence of n on collision speed for He + H₂O, He + N₂, and He + CO₂, inferred by fitting the data in the Appendix to Eq. (10). The fact that n is much greater than unity over the range of collision speeds of interest here illustrates the failure of the hard-sphere scattering approximation for this particular problem.

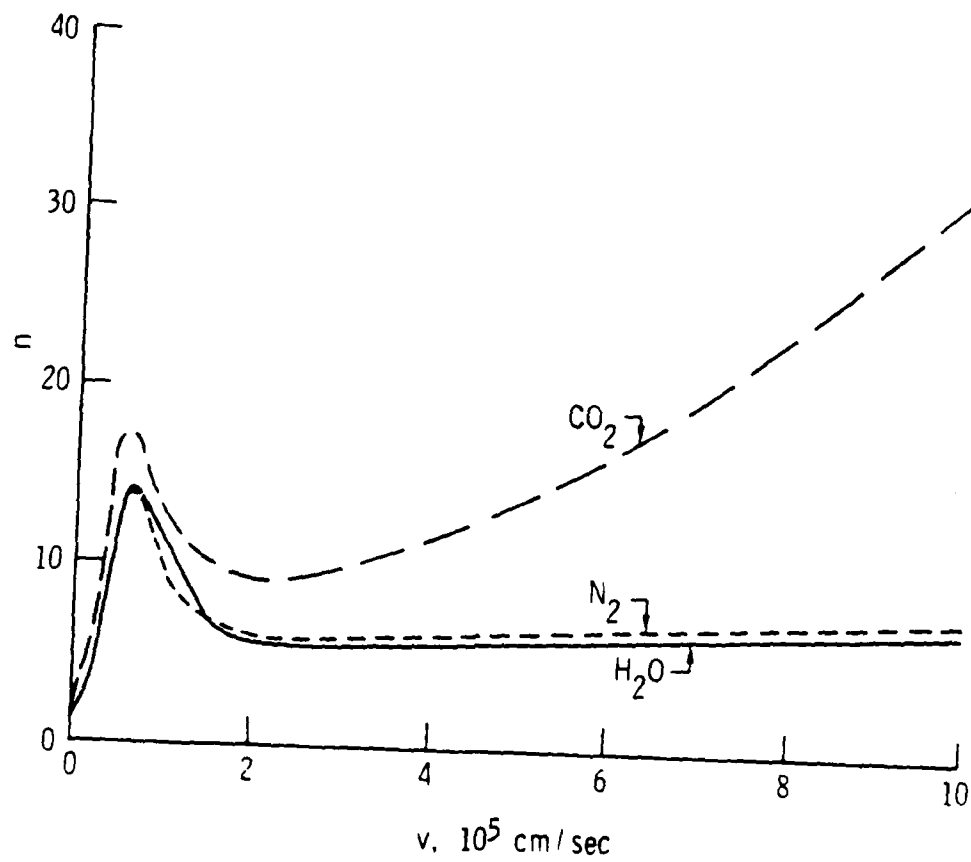


Fig. 5. Parametric Fit (Scattering Parameter) of $\cos \theta = 1 - 2p_c^n$ (see text) for He + H₂O, He + N₂, and He + CO₂

III. ESTIMATED CONTAMINATION LEVEL

The characteristics of the expected contaminants are necessary input conditions for the He-purge transmission calculations. At an orbital altitude of 380 km and a velocity of $v_0 = 7.7 \times 10^5$ cm/sec, O atoms will be the most abundant atmospheric species. For standard atmospheric conditions, they will be present at a density of $n = 1.7 \times 10^8$ cm⁻³, corresponding to a flux of $F = v_0 n = 1.4 \times 10^{14}$ cm⁻² sec⁻¹. However, they could reach the CIRRIS primary mirror only for a telescope line of sight that makes a small angle β with the direction of the orbital velocity \vec{v}_0 , whereas the CIRRIS IA mission plans specify¹⁴ that $\beta > 90^\circ$. For these large values of β , the O atoms incident along the telescope axis will be negligible. Indeed, it can be shown¹⁵ that the incident flux decreases very rapidly with increasing β as

$$f = K \{ a(2a^2 + 3) [\text{erf}(a) + 1] \exp(-c^2 \sin^2 \beta) + (2/\pi^{1/2}) (a^2 + 1) \exp(-c^2) \} \quad (11)$$

where $K = 1.6 \times 10^{12}$ O atoms cm⁻² sr⁻¹ sec⁻¹, $a = c \cos \beta$, and $c = 7.0$ is the ratio of v_0 to the most probable O atom thermal speed. At $\beta = 0^\circ$, $f = 2.2 \times 10^{15}$ O atoms cm⁻² sr⁻¹ sec⁻¹, whereas $f < 5 \times 10^{-8}$ O atoms cm⁻² sr⁻¹ sec⁻¹ for any β between 90° and 180° , i.e., attenuated by more than 23 orders of magnitude. It should also be noted that, by virtue of the comparable masses and similar cross-section behaviors indicated in the Appendix, He purge results that are calculated here for H₂O would be approximately valid for O atoms as well.

Reference 16 reports results from a mass spectrometer flown on the Shuttle Orbiter. The inlet of the mass spectrometer was collimated to a narrow field of view, 0.1 sr, of the space environment so that molecules outgassing from Orbiter surfaces could not reach it by a straight-line trajectory. Contaminants entering the CIRRIS telescope are under the same geometric constraint; contaminants enter either instrument only by virtue of some other transport mechanism, such as self-scattering or scattering from atmospheric

O atoms. Detected contaminants reported in Ref. 16 include H₂, He, diborane, (B₂H₆), methane (CH₄), N₂, CO, O, monomethyl hydrazine (CH₃N₂H₃), H₂O, CO₂, nitric oxide (NO), O₂, hydrogen chloride (HCl), and propane (C₃H₆). With the possible exception of N₂, which is discussed later, H₂O was the dominant species. This same predominance of contaminant H₂O was also observed¹⁷ by a different mass spectrometer instrument on one Shuttle flight; in this case, however, outgassed molecules could reach the mass spectrometer directly by collisionless, straight-line trajectories.

Table 1 lists the H₂O contamination levels reported in Ref. 16 for Space Transportation System (STS) flights 3 and 4. The source of this H₂O was outgassing from Shuttle Orbiter surfaces. Typically, outgassing rates are high immediately after launch and decay over a period of many hours to a steady value. Values listed in Table 1 are approximate 100-hr averages for the sensor perpendicular to the wind direction, i.e., for $\beta = 90^\circ$. There have also been a number of predictions of the expected Orbiter contaminant environment. Two representative predicted values^{18,19} are also included in Table 1 to indicate that the measured values conformed to reasonable expectations.

Thus, CIRRIS IA will probably have to contend with a contaminant H₂O environment similar to that present on STS flight 3, i.e., $\sim 3 \times 10^{11}$ H₂O molecules cm⁻² sr⁻¹ sec⁻¹. However, there is no doubt that the contaminant H₂O environment was worse on STS-4 because of the hail and rain experienced by Columbia during the STS-4 prelaunch preparation. It is therefore prudent to take the STS-4 environment, $\sim 7 \times 10^{12}$ H₂O molecules cm⁻² sr⁻¹ sec⁻¹, as the postulated worst-case environment for the CIRRIS IA mission.

Transmission through the He purge flow depends on the speed v_c of the incident contaminant. This, in turn, depends on the mechanism that transports the contaminant from its source to the sensor aperture. For a contaminant of mass m_c that escapes from the Shuttle Orbiter and scatters off an atmospheric O atom of mass m_0 back toward the sensor

$$v_c \approx 2[m_0/(m_0 + m_c)] v_0 \cos\beta \quad (12)$$

Table 1. Estimates of H₂O Flux Impinging on the CIRRIS IA Aperture^a

Source		H ₂ O Flux (cm ⁻² sr ⁻¹ sec ⁻¹)
<u>Outgassing - STS-3</u>		
Ref. 16	Mass Spectrometer Measurement	3 × 10 ¹¹
Ref. 18	Calculation	1 × 10 ¹¹
Ref. 19	Calculation	2 × 10 ¹⁰
<u>Outgassing - STS-4</u>		
Ref. 16	Mass Spectrometer Measurement	7 × 10 ¹²
<u>Vernier Engine Firing</u>		
Ref. 17	Mass Spectrometer Measurement ^b	0.4 - 4 × 10 ¹⁴
Ref. 18	Calculation	1 × 10 ¹⁴
Ref. 19	Calculation	1 × 10 ¹³

^aThese are approximate values for a sensor line of sight perpendicular to the wind. Actual values reported in Refs. 16 through 19 were scaled to those at 380 km by assuming contaminant return flux to be proportional to atmospheric density.

^bCalculated by assuming a 2π-steradian field of acceptance for the mass spectrometer.

for $0^\circ < \beta < 90^\circ$. This expression fails, of course, near $\beta = 90^\circ$, where it predicts that v_c goes to zero. The contaminant flux from this mechanism would also be β dependent, peaking at $\beta = 0^\circ$ and dropping to zero at $\beta = 90^\circ$. Reference 16 does provide some qualitative data on this β dependence. The values in Table 1 from Ref. 16 refer to some $\beta \approx 90^\circ$. Data in Ref. 16 actually indicate that the H_2O return flux varies by a factor of ~ 80 between $\beta = 0^\circ$ and 90° . Calculations reported in Ref. 19 are in reasonable agreement, giving a factor of ~ 25 for this variation in H_2O return flux. The variation in H_2O return flux with β is probably a sharp function of β . In the absence of any better information, and in order to make a conservative estimate of the H_2O return flux, however, the H_2O return flux used to estimate H_2O film build-up on the CIRRIS IA primary mirror is taken to be

$$f_{H_2O}(\beta) = f_{H_2O}(\beta = 90^\circ) [1 + (79 \cos\beta)], \quad 0^\circ < \beta < 90^\circ$$

and

$$f_{H_2O}(\beta) = f_{H_2O}(\beta = 90^\circ), \quad \beta > 90^\circ \quad (13)$$

where $f_{H_2O}(90^\circ) = 7 \times 10^{12} H_2O \text{ molecules cm}^{-2} \text{ sr}^{-1} \text{ sec}^{-1}$ (STS-4 result). For $\beta > 90^\circ$, the return flux is due to self-scatter of two or more collisions with the wind, and it should return with speeds comparable to or less than thermal speeds of outgassed molecules. Thus, for angles $\beta > 90^\circ$, v_c is taken as $\sim 6 \times 10^4 \text{ cm/sec}$, the average thermal speed of H_2O at 300 K.

The CIRRIS IA mission plan currently specifies that no engine in the Orbiter may fire while the telescope is uncapped. This includes the small 25-lb-thrust vernier control system (VCS) engines. In order to estimate the consequences if this requirement were relaxed, the contaminant environment produced by these engines has also been considered. The largest source of uncertainty is the return speed of molecules that are produced when these engines fire, as there are neither measurements nor calculations of this parameter. Along the axis of the plume, the flow velocity is $\sim 3.5 \times 10^5 \text{ cm/sec}$. However, molecules that return to the Orbiter bay probably originate

from the wings of the plume flow field. Here, plume flow velocity may be less than the flow velocity along the axis. Again, however, there are neither measurements nor calculations of velocities in this region of the plume of this engine. In any case, plume molecules can return to the Orbiter Bay because of collisions with the atmosphere at a wide range of speeds v_c that correspond to the range in possible geometries of motor location and thrust direction in relation to the Orbiter's attitude and the sensor's line of sight.

For H_2O , a reasonable range of return speeds is $v_c \approx 0.6 - 5 \times 10^5$ cm/sec. Reference 17 measured density spikes of H_2O and N_2 , but not of CO or CO_2 , associated with firings of these VCS engines. The corresponding return fluxes are listed in Table 1; the range in values quoted corresponds to the range of uncertainties in v_c . Recently, Ehlers²⁰ reported calculations of the return flux as a function of VCS engine location. His calculations exhibit a large variation in return flux, by approximately a factor of 40, as the angle between the Orbiter's velocity and the instrument's line of sight varies between 10° and 90° , in approximate agreement with the factor estimated in Table 1. When converted to an altitude of 380 km, however, the absolute magnitude of his calculated return fluxes are lower by approximately a factor of ten than the estimate given in Table 1. Here again, the estimate in Table 1 is used to calculate the rate of cryodeposit buildup in order to provide the more conservative, worst-case analysis. However, it is important to note that the observations reported in Ref. 17 included contributions from the vernier engines on the rear of the Orbiter. The plumes of these motors impact, at least partially, on the wings of the Shuttle. Thus, it is quite possible that data from Ref. 17 represent an unrealistic worst case for the CIRRIIS mission because direct scattering of plume molecules from the Orbiter wing could have contributed significantly to the observations reported in Ref. 17, whereas it could not contribute return flux along the CIRRIIS line of sight. For this reason, cryodeposit buildup rates based on Ehlers'²⁰ return fluxes are also discussed later.

In addition to H_2O , N_2 is probably also an important contaminant molecule in the vicinity of the Orbiter. However, the information on the return flux of this contaminant is very limited. Owing to an instrumental

background at mass 28, Ref. 16 reported no data on N_2 return flux except at small β angles, where impingement of atmospheric N_2 is important. Reference 17 reports N_2 and H_2O densities that are in a ratio of ~ 0.02 in the absence of a VCS firing, and ~ 1 in the transient spike in the presence of a VCS firing. In the absence of a VCS firing, it is not clear what fraction of either of these N_2 or H_2O signals corresponds to a return flux. In a recent paper recommending environment estimates for the Orbiter bay, Scialdone²¹ recommends an on-orbit N_2/H_2O ratio of ~ 40 , in clear disagreement with results measured in Ref. 17. Thus, in the absence of data on the N_2 return flux, the value adopted here is the calculated flux reported in Ref. 19 for $\beta = 90^\circ$. This was adjusted to a corresponding flux at the CIRRIIS altitude of 380 km by correcting linearly for differing atmospheric densities to give

$$f_{N_2}(\beta) = 1 \times 10^{11} N_2 \text{ molecules cm}^{-2} \text{ sr}^{-1} \text{ sec}^{-1}, \beta > 90^\circ \quad (14a)$$

Here, v_c is taken as 4.6×10^4 cm/sec, the average thermal velocity of N_2 at 300 K. This should represent a conservative overestimate of the actual N_2 return flux, because Ref. 19 calculated it for an N_2 release corresponding to the maximum possible atmospheric cabin leakage rate that NASA specifications permit. Again, the β dependence of this N_2 flux is assumed to have the forms

$$f_{N_2}(\beta) = f_{N_2}(\beta = 90^\circ) \{1 + 49 \cos\beta\}, 0^\circ < \beta < 90^\circ \quad (14b)$$

Once more, this is a conservative overestimate, with the $\beta = 0^\circ/\beta = 90^\circ$ ratio exceeding that calculated in Ref. 19 by a factor of ~ 2 .

A. CRYODEPOSIT BUILDUP RATE

For a contaminant like H_2O , which sticks to the sensor walls, film buildup on the primary mirror is due solely to molecules that strike the mirror first. Consider H_2O impinging through a point on a hemisphere of radius r that is centered on the sensor aperture. The solid angle subtended by the sensor aperture is $A \cos\gamma/r^2$, where A is the aperture area. Then, the number of H_2O molecules that pass through a small area on this hemisphere and would enter the sensor in the absence of any He flow is given by

$$f(\gamma, \phi) (A \cos \gamma / r^2) r^2 \sin \gamma d\gamma d\phi$$

For the case considered here, where the areas of the mirror and the sensor aperture are the same, the average number of H₂O molecules condensing per second per cm² of mirror becomes

$$C = \int_0^{2\pi} \int_0^{\pi/2} \tau(\gamma) f(\gamma, \phi) \sin \gamma d\gamma d\phi \quad (15)$$

As discussed in Table 2, the factor of cos γ is included in the $\tau(\gamma)$ values that are calculated.

Clearly, $f(\gamma, \phi)$ can be calculated from the $f(\beta)$ expressed in Eqs. (13) and (14). In view of the approximate nature of this assumed cos β functional dependence, however, the angular flux dependence was ignored in evaluating Eq. (15) to obtain

$$C = f \tau(0) B \quad (15a)$$

where

$$B = \frac{2\pi}{\tau(0)} \int_0^{\pi/2} \tau(\gamma) \sin \gamma d\gamma \quad (16)$$

Nevertheless, the value of f in Eq. (15a) will be calculated for the particular value of the angle β between \vec{v}_0 and the sensor line of sight. Then, the rate of contaminant film buildup, in cm/sec, is given by

$$\dot{t} = CM/6 \times 10^{23} \rho \quad (17)$$

where M is the molecular weight and ρ is the density.

As will be discussed later, N₂ represents the opposite case of a molecular contaminant having a temperature-dependent vapor pressure that prevents condensation on the warmer sensor walls but that allows condensation

Table 2. Summary of All He Purge Efficiency Calculations^a

Run	Species	v_c 10 ⁵ cm/sec	γ , deg	\dot{m} , g/sec	T_{He} , K	T_w^b , K	N_{He} , 10 ¹³ /cm ³	N	N_m	N_w	N_{O1}	N_{I0}	t^c	η^d
1 ^e	0	8.0	0	0.006	20	20	52.4	1000	0	339	0	483		
2							1.82		24	397	1	458	0.048±0.010	
3							0		70	347	3	412	0.140±0.017	
4				N/A			1.82		163	342	0	342	0.323±0.025	
5				0.006			0		65	346	3	418	0.130±0.016	
6				N/A			1.82		176	319	2	317	0.352±0.027	
7 ^f							0.67		450	550	0	550	0.450±0.021	
8 ^g	H ₂ O			0.006			1.82		47	364	6	448	0.094±0.014	
9			3						50	465	10	439	0.067±0.010	
10			6						45	467	19	428	0.030±0.005	
11			9						16	452	9	406	0.0017±0.0004	
12			6					2000	57	653	31	377	0.038±0.005	
13			0	0.01			3.03		27	679	5	979	0.027±0.005	
14			6						25	860	13	862	0.0083±0.0017	
15			0	0.02			6.07		7	407	3	979	0.0070±0.0027	
16		0.6		0.006			1.82	700	0	29	0	342	<0.003	
17	CO ₂	8.0		0.01			3.03	2000	495	460	23	518	0.495±0.022	
18		0.6		0.006			1.82	700	5	206	0	347	0.014±0.006	
19		4.3		0.02			6.07	2000	154	760	14	852	0.154±0.012	
20		0.38						700	0	0	0	337	<0.003	
21	N ₂	0.48	0	0.02	20	20	6.07	700	0	0	0	331	<0.003	<0.003
22		5.8						2000	32	558	7	903	0.033±0.006	
23	H ₂ O	8.0		0.006			7.89	1000	23	367	3	470	0.046±0.010	
24				0.01			13.2		12	344	4	486	0.024±0.007	
25				0.02			26.3		0	185	0	512	<0.002	
26								2000	1	371		984	0.001±0.001	
30				0.006			0	1000	41	350	3	433	0.082±0.013	
27 ^h		0.6		0.02					0	0	0	472	<0.002	
28	N ₂	0.48							0	1		512		0.002±0.002

Table 2. Summary of All He Purge Efficiency Calculations^a (Continued)

Run	Species	V_c , 10 ⁵ cm ³ /sec	γ , deg	\dot{m} , g/sec	T_{He} , K	T_{He}^b , K	T_{He}^b , K	N_{He} , 10 ¹³ /cm ³	N	N_m	N_w	N_{o1}	N_{i0}	τ^c	η^d
29	CO ₂	0.38	0	0.02	20	20	0	1000	0	5	0	464	0.002		
31	H ₂ O	8.0					3.63	2000	126	653	17	871	0.126±0.011		
32							0	1000	87	311	12	426	0.174±0.019		
33					273	77			213	278	13	307	0.426±0.029		
34		0.6							4	36	1	480	0.008±0.004		
35				0.074					0	0	0	501	0.002		
36		8.0							41	309	3	448	0.082±0.012		
37		1.2		0.02					25	155	1	477	0.050±0.010		
38		3.0							94	285	3	403	0.188±0.019		
39	N ₂	0.48							1	19	0	486	0.002±0.002	0.040±0.009	
40	CO ₂	0.38							5	70		496	0.010±0.005		
41		0.38	0	0.032	273	77	0	1000	0	14	0	512	0.002		
42	N ₂	0.48								1		510	0.001±0.001		
43	H ₂ O	0.6								6		500			
44				0.01					18	119		478	0.076±0.009		
45							1.82		15	123		515	0.030±0.008		
46							12.0		1	106		514	0.002±0.002		
47							6.0		5	111		507	0.010±0.005		
48	N ₂	0.48		0.02			0		1	26		479	0.002±0.002	0.054±0.010	
49		0.6							6	46		473	0.012±0.005	0.104±0.014	
50 ¹	H ₂ O								1	26		273	0.004±0.004		
52	N ₂	1.0							24	188	5	472	0.048±0.010	0.424±0.029	
53		5.8							258	225	19	248	0.516±0.032	0.966±0.044	
54	H ₂ O	8.0							62	310	6	423	0.124±0.016		
55									44	367	5	453	0.088±0.013		
56		0.6		0.002					73	224	2	433	0.146±0.017		
57				0.005					10	109	0	517	0.020±0.006		
58		1.2		0.02					15	99	2	232	0.060±0.016		
59	N ₂	5.8	30						1	464	1	0	0.0017±0.0017	0.805±0.037	

Table 2. Summary of All He Purge Efficiency Calculations^a (Continued)

Run	Spectes	v_c^c 10 ⁵ cm/sec	γ , deg	\bar{m} , g/sec	T_{He} , K	T_w^b , K	N_{He}^b , 10 ¹³ /cm ³	N	N_m	N_w	N_{oi}	N_{io}	τ^c	n^d
60	N ₂	5.8	60	0.02	273	77	0	1000	0	446	0	0	<0.001	0.446±0.021
61		0.48	30						10				<0.0017	0.017±0.005
62			60						5				<0.001	0.005±0.002
63			80						5				<0.00035	0.0017±0.0008
64	H ₂ O	8.0	20						32	421		32	0.060±0.010	
65			30						6	445	6	0	0.010±0.004	
66			40				1500		1	666	1	0	0.001±0.001	
67			10				1000		126	371	57	125	0.250±0.020	
68		0.6							1	30	0	204	0.002±0.002	
69	N ₂	1.0	60						0	111	0	0	<0.001	0.111±0.011

^a \bar{m} , v_c , γ , N_{He} , T_{He} , T_w , τ , and n have been defined in the text. Other symbols are as follows:

N - number of trajectories sampled

N_m - number of trajectories that terminate on mirror

N_w - number of trajectories that terminate on wall

N_{oi} - number of trajectories that would have missed mirror with no He flow, but hit with He flow

N_{io} - number of trajectories that would have hit mirror with no He flow, but missed with He flow

Other counts of interest are as follows:

$N_m + N_w + N_{io}$ - number of trajectories entering sensor

$N_{ii} = N_m - N_{oi}$ - number of trajectories that would have hit mirror with no He flow and hit with He flow

$N_{oo} = N - N_m - N_{io}$ - number of trajectories that would have missed mirror with no He flow and missed with He flow

^b As noted in the text, sensor wall temperature varies between ~20 and 40 K. Calculations were done for T_w (the effective temperature of He within the sensor) of 20 and 77 K, which bounds this range. Note that T_w does not enter the calculation when $N_{He} = 0$.

Table 2. Summary of All He Purge Efficiency Calculations^a (Continued)

$C_t = f \cos y (N_u \pm N_m^{1/2})/M$ is the transmittance [Eq. (4)] and its standard deviation. Note that a $N^{1/2}$ contribution to the standard deviation in τ and n was ignored. The factor f accounts for the size chosen for the control area. Its value is 7, with the following exceptions:

Run	f
9	1.351
10	0.667
11	0.105
12	1.334
14	0.667
50	4
58	4

When $N_m = 0$, $\tau = f \cos y/M$ defines a one-standard-deviation upper bound on τ .

$d = n = f \cos y \frac{(N_u + N_m) \pm (N_u + N_m)^{1/2}}{M}$ is the acceptance [Eq. (5)] and its standard deviation.

^aRuns 1 through 6 are early preliminary CIRIS I calculations, with $\omega = 60$ and various combinations of the injection and barrel pressure as follows:

Run	Condition
1	Injection plume + barrel plume + barrel
2	Injection plume + barrel plume + barrel
3	Injection plume + barrel plume alone
4	Barrel alone
5	Injection plume alone
6	Barrel + barrel plume alone

^bRun 7 tests results reported in Ref. 7. $R = 16.127$ cm, $L = 206$ cm, and hard-sphere scattering were used for this run only.

^cRuns 8 through 26 and 30 employ CIRIS I geometry. $R = 8.4$ cm, $L = 96$ cm.

^dRuns 27 through 29 and 31 through 69 employ CIRIS IA geometry. $R = 16.25$ cm, $L = 96$ cm.

^eRun 51 was not applicable to this problem and is deleted.

on the primary mirror. In this case, a steady-state N_2 density develops in the sensor according to

$$n_{ss} = 2 f n(0) B' / \bar{v} \quad (18)$$

where

$$B' = \frac{2\pi}{n(0)} \int_0^{\pi/2} n(\gamma) \sin\gamma d\gamma \quad (19)$$

\bar{v} is the average N_2 thermal speed of 1×10^4 cm/sec at 20 K, and a factor of 2 enters because N_2 enters only one end of the telescope but is removed at both ends. In this case, the cryodeposit growth rate, in cm/sec, is given by

$$\dot{t} = 0.25 n_{ss} \bar{v} M / 6 \times 10^{23} \rho \quad (20)$$

for $n_{ss} > n_{ss}^0$

and

$$\dot{t} = 0$$

for $n_{ss} < n_{ss}^0$

where $n_{ss}^0 = 4.8 \times 10^6 \text{ cm}^{-3}$ is the number density²² corresponding to the vapor pressure of N_2 at 20 K, the temperature of the primary mirror.

B. SIGNIFICANT CRYODEPOSIT THICKNESS

Clearly, some small contamination buildup on the primary mirror can be tolerated. However, the critical thickness associated with the onset of significant degradation in sensor optical performance is not well defined. A careful definition of this critical thickness would itself require a study comparable in effort to the present analysis of He purge efficiency. This section is restricted to a review of the very limited published information on this question and to a rough estimate of the thickness of cryodeposit films which might begin to affect the optical performance of the CIRRIIS telescope.

Both absorption and scattering by the contaminant film can adversely affect optical performance. Absorption is well understood. The thickness of an ice deposit, for example, should be less than $\sim 0.1 \mu\text{m}$ (1000 Å) in order to prevent significant absorption of radiation within the

H₂O absorption bands.²³ However, the scatter properties of condensed films are only poorly characterized. For the SIRE (Satellite Infrared Experiment) sensor, which had off-axis rejection requirements similar to those of CIRRIS, it was estimated that cryodeposit thicknesses up to 2 μm would produce insignificant scatter.² A similar estimate of 1 μm for the SIRTf (Shuttle Infrared Telescope Facility) is given in Ref. 1. However, the basis of these estimates is not documented; they probably refer to a homogeneous smooth deposit. Reference 24 specifies a bidirectional reflectance distribution function (BRDF) scatter performance for the primary mirror of CIRRIS of 10^{-4} sr^{-1} at $\theta = 1^\circ$, with a θ^{-2} rolloff. These authors mention, but do not reference, measurements that indicate that 2 to 10 μm of contaminant buildup can cause a degradation by a factor of 10 to 100 in this mirror's scatter performance.

Reference 25 reports measurements at $\lambda = 10.6 \mu\text{m}$ of BRDF mirror scatter increase produced by ~ 1 to $20\text{-}\mu\text{m}$ cryodeposits of various species. Oxygen deposits consistently caused an increase in scatter with increased deposit thickness. For example, the data indicate that an O₂ deposit of 1.7 μm would degrade the BRDF to the CIRRIS specification of $1.8 \times 10^{-5} \text{ sr}^{-1}$ at 2.3° . In contrast, N₂ deposits as thick as $\sim 25 \mu\text{m}$ did not ordinarily produce any measureable BRDF change. In a few cases, however, BRDF increased by ~ 10 to 100. This was presumably associated with the formation of an N₂ frost, as opposed to that of a transparent, continuous, homogeneous smooth film.

In one case, the scatter from an N₂ film increased markedly after partial evaporation, perhaps because of some recrystallization that greatly increased scatter centers. Subsequent N₂ deposition onto this film increased the scattering markedly. This worst-case N₂ behavior would indicate that the N₂ cryodeposit must not exceed $\sim 0.05 \mu\text{m}$ (500 Å) in order to meet the CIRRIS BRDF requirement. Because better information is not available, this is the safe limit recommended here for contaminants other than H₂O that do not absorb appreciably. It is probably a conservative limit because it is based upon the worst N₂ behavior observed. Moreover, it is also subject to considerable uncertainty because it is arrived at from an assumption that BRDF increase is

proportional to cryodeposit thickness t from molecular dimensions to dimensions comparable to the wavelength λ of the incident radiation. In reality, there are neither data nor theories to support such a linear, or other particular functional, extrapolation.

Reference 25 also reports five measurements of water vapor depositions, with $t \approx 3$ to $5 \mu\text{m}$, on mirrors at temperatures from 27 to 74 K. Three of these measurements revealed no increased mirror scatter. However, two other cases revealed a mirror scatter increase $> 10^5$, i.e., one much larger than that due to the N_2 frost. A linear thickness extrapolation of this behavior gives an H_2O thickness limit of $\sim 6 \times 10^{-5} \mu\text{m}$ (0.6 Å) before the CIRRIS BRDF requirement is exceeded. However, this linearly extrapolated thickness limit seems unrealistically small, which indicates the failure of a linear extrapolation in at least this case. Before any contamination, the best available, state-of-the-art, super-polished mirrors, with BRDF at $\lambda = 10 \mu\text{m}$, considerably better than the CIRRIS requirement, have²⁶ root-mean-square (RMS) roughnesses of 10 to 50 Å. Electromagnetic boundary-value theoretical expressions given in Ref. 26 for mirror BRDF can be used to estimate RMS surface roughness limits for H_2O , which should be highly reflective at wavelengths where it absorbs strongly. These theoretical expressions depend a great deal on the surface roughness correlation length as well. They would indicate a $\sim 0.01 \mu\text{m}$ surface roughness for a correlation length assumed to be much less than a wavelength $\approx 0.1 \mu\text{m}$ at $\lambda = 2.7 \mu\text{m}$ (a wavelength near the short-wavelength edge of the CIRRIS band where water is highly absorbing), in order to meet the CIRRIS BRDF requirement at one degree. In the absence of any better information, a critical thickness limit estimate of $0.01 \mu\text{m}$ (100 Å) is adopted here for H_2O deposition on the CIRRIS primary mirror.

IV. MONTE CARLO HELIUM-PURGE EFFICIENCY RESULTS

A summary of all of the Monte Carlo calculations is given in Table 2. The He purge efficiency depends on a number of variables, viz sensor geometry, molecular identity, impact speed v_c , impact direction γ , He mass flow rate \dot{m} , number density of He within the sensor N_{He} , and temperatures of the He effusion sources T_{He} and T_w . In general, these results show the following general trends in transmission of contaminants through the He purge:

- (a) τ decreases monotonically with increasing \dot{m} or γ or N_{He} ;
- (b) τ increases monotonically with increasing v_c or T_{He} ;
- (c) τ (CIRRIS IA) $>$ τ (CIRRIS I); and
- (d) τ (CO_2) $>$ τ (N_2) $>$ τ (H_2O), other variables being equal.

These trends are discussed in more detail in the remainder of this section.

One striking feature of the results listed in Table 2 is that the purge flow of He provides very significant protection against impinging contaminants in some cases. This is most striking for CIRRIS I. In many of these cases, no contaminants reached the mirror and only an upper limit could be set on τ . An example is the case of H_2O impinging at $v_c = 6 \times 10^4$ cm/sec, with $\dot{m} = 0.02$ g $_{He}$ /sec and $\tau < 0.002$ (run 27). Indeed, $\tau < 0.001 \pm 0.001$ for this case because this was the value calculated for a much higher impingement speed, $v = 8 \times 10^5$ cm/sec (run 26). In fact, an examination of wall deposition numbers in the different calculations indicates that $\tau \lll 0.001$ for thermal H_2O at $\dot{m} = 0.02$ g $_{He}$ /sec, perhaps by orders of magnitude. Figure 6, for example, shows results for H_2O impinging at orbital velocity. Out of 2000 trajectories followed, one reached the mirror, whereas 371 others deposited along the sensor wall with an approximate exponential decay. In contrast, not a single one out of a total of 1000 trajectories even entered the aperture for thermal H_2O in run 27. Thus, in some cases the He purge flow does indeed sweep aside completely the impinging thermal contaminants. The assumption discussed earlier of a unit sticking coefficient is clearly inconsequential for these cases.

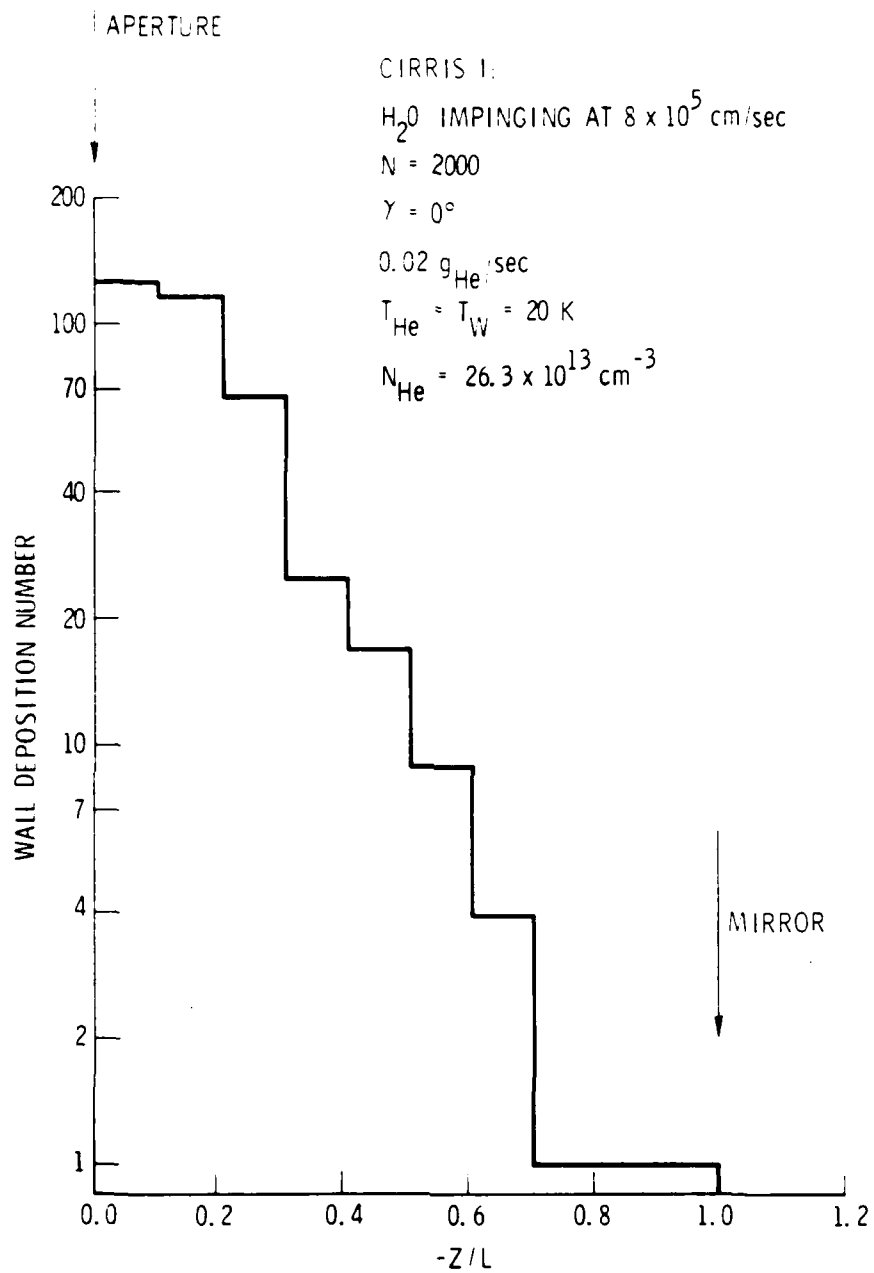


Fig. 6. Histogram of H_2O Deposition along the CIRRIS I Sensor Wall

The remainder of the discussion presented here concentrates on CIRRIS IA, the instrument that will be used on an upcoming flight. Both CIRRIS I and CIRRIS IA were modeled as telescopes with a separation $l = 94$ cm between the sensor aperture and the primary mirror. Figure 7 compares the CIRRIS I and IA entrance apertures. The CIRRIS IA aperture is approximately elliptical, with an area $A = 345$ cm², whereas the CIRRIS I aperture was circular, with $A = 222$ cm². Because the Monte Carlo trajectory program required a circular aperture, the CIRRIS IA aperture was modeled in these calculations as circular, with a diameter equal to the major diameter of the ellipse and an area $A = 829$ cm². At a given flow rate \dot{m} , the He attenuates incoming contaminants more efficiently for CIRRIS I than for CIRRIS IA, because there is less sensor aperture area to protect and because deflections through smaller angles, on average, will cause the contaminant to miss the sensor aperture or strike the inside sensor wall. Thus, the CIRRIS IA results presented here, based upon the much larger circular aperture area, are conservative in underestimating the actual attenuation that is due to the He gas. In view of the values of the three areas, in fact, the results presented here for CIRRIS IA should be very conservative, with the real CIRRIS IA behavior closer to that of CIRRIS I than are the computed results for CIRRIS IA.

Figure 8 illustrates some of these remarks. The transmission is a strong function of He flow rate. The He provides considerably more protection for the CIRRIS I geometry than for the CIRRIS IA geometry. Even for CIRRIS IA, however, at the planned flow rates of 0.02 g_{He}/sec, the He flow still provides significant protection against H₂O impinging at low speed.

Increasing the He ejection temperature T_{He} should increase the He momentum while decreasing the steady-state density in front of the sensor. The effect on impinging contaminants can be seen in Table 2 by comparing runs 27 versus 34, 32 versus 33, and 28 versus 39. Apparently the density change is more important. In all cases, $T_{He} = 20$ K was considerably more effective than $T_{He} = 273$ K, and had a particularly big effect on the N₂ acceptance.

Figure 9 illustrates that H₂O transmission shows appreciable dependence on the steady-state density of He within the sensor. The model of

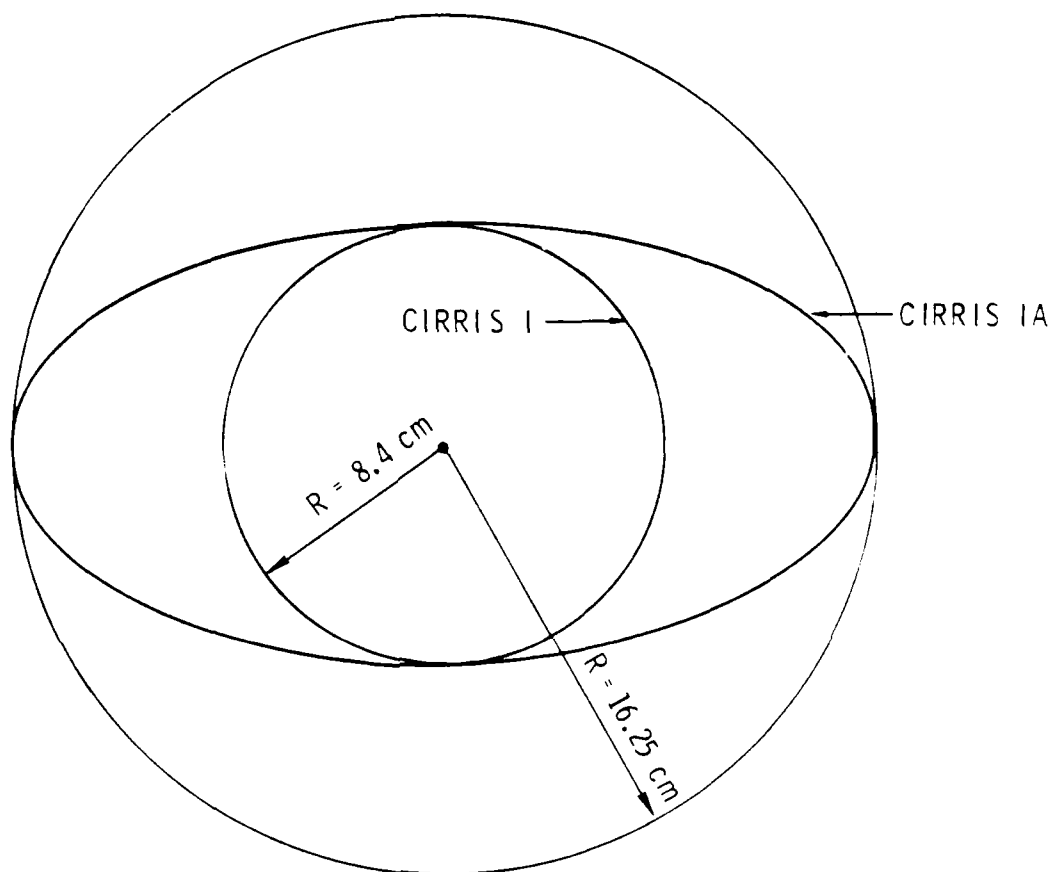


Fig. 7. Normal View of Sensor Apertures. The CIRRIS I aperture is circular, $R = 8.4$ cm. However, the CIRRIS IA elliptical aperture was modeled by a larger circular aperture, $R = 16.25$ cm.

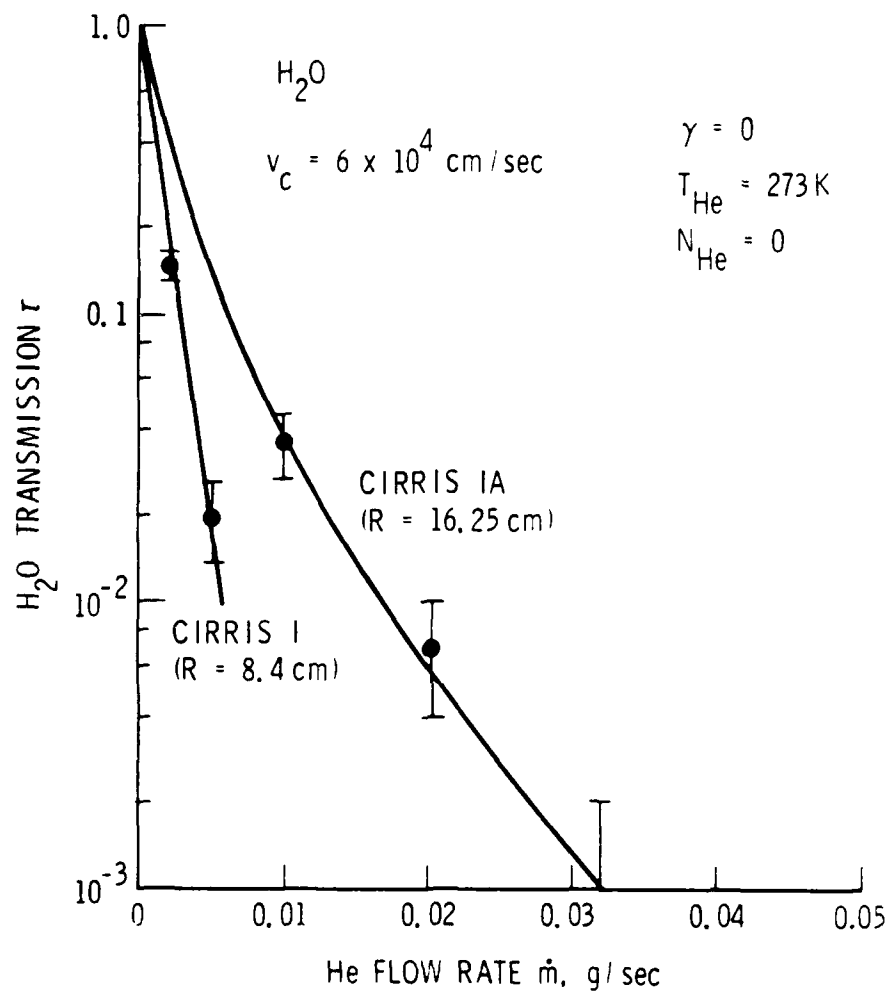


Fig. 8. Transmission of H_2O Contaminant as a Function of He Flow Rate \dot{m} , for Runs 34, 43, 44, 56, and 57

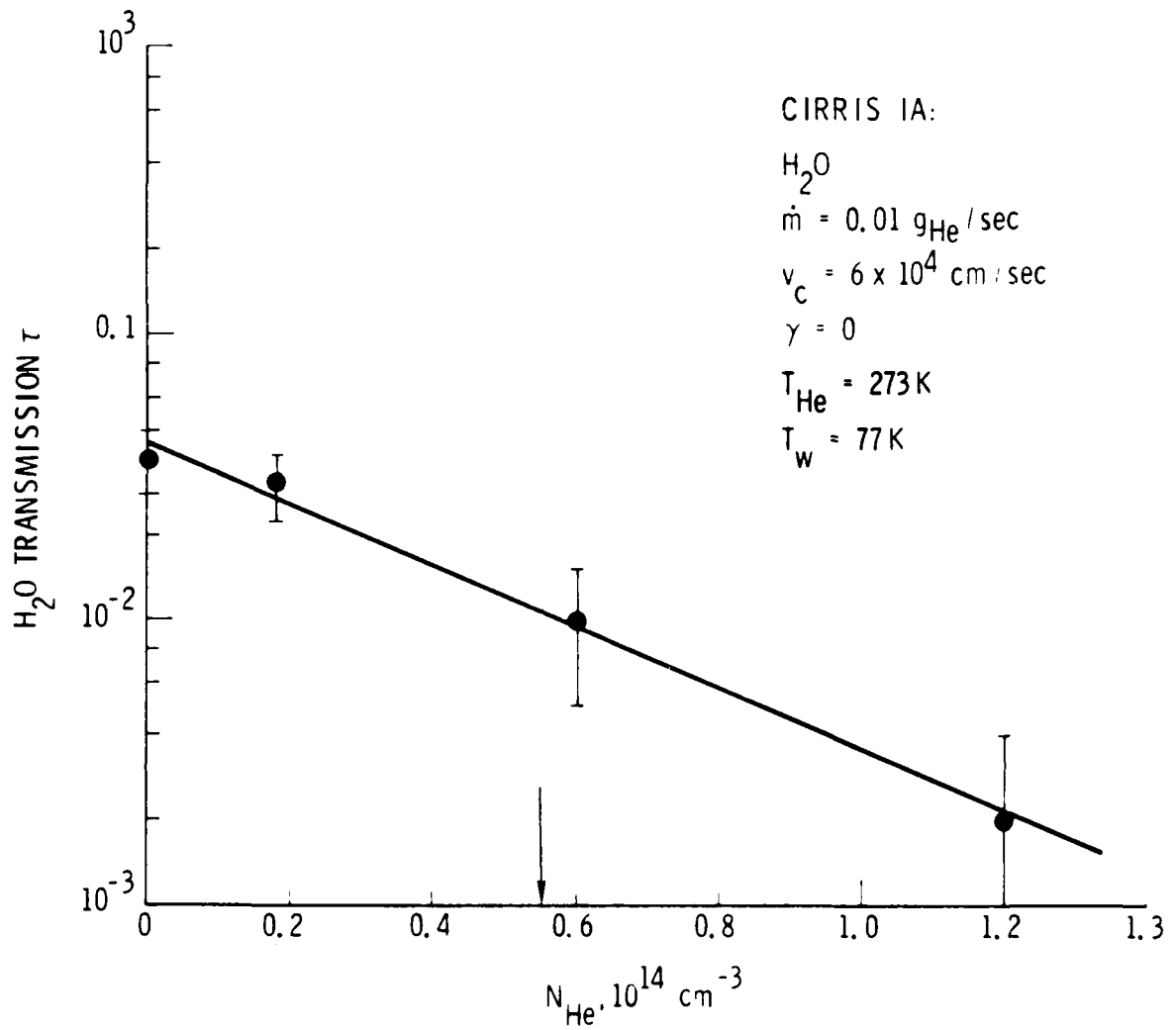


Fig. 9. Transmission of H_2O Contaminant as a Function of Steady-State He Density in the Sensor for Runs 44 through 47. The arrow indicates that $N_{\text{He}} = 0.55 \times 10^{14} \text{ cm}^{-3}$ for true effusion of He out of the ejector ring.

effusion of He from the ejection ring into the sensor actually predicts $N_{\text{He}} = 0.55 \times 10^{14} \text{ cm}^{-3}$, so that the true value is likely to be somewhere between this number and zero. Contaminant buildup rates that are estimated later represent the conservative analysis where N_{He} is taken as zero. In reality, the buildup of H_2O should be significantly slower than the estimates for H_2O provided later in this report, as a result of a finite N_{He} . The buildup rate of N_2 , however, should show very little or no dependence on N_{He} , because the He must deflect the N_2 before it enters the sensor. There might be a small dependence associated with the small increase in He density in front of the sensor, as a result of effusion from the sensor for a finite N_{He} .

The transmission of H_2O is plotted versus He flow rate for two speeds of contaminant approach in Fig. 10. This illustrates that τ exhibits an initial, Beer's-law exponential decrease with increasing \dot{m} , but that significant deviations from this simple dependence appear in the $v_c = 6 \times 10^4$ cm/sec results, where the attenuations are clearly well beyond the single-collision regime. Figure 11 illustrates the very strong dependence of τ on speed of approach for H_2O . This is reproduced in Fig. 12, where results for N_2 and H_2O are compared. This illustrates that the contaminant transmission is more sensitive to impact speed v_c than to molecular identity. For this reason, the investigation of sensitivity to collision cross sections was not pursued beyond that represented by runs 7, 48, and 54. Comparisons of runs 54 and 33 are interesting, however. Run 54 was done for a total cross section independent of v , with a value equal to that for H_2O at $v = 8 \times 10^5$ cm/sec but with an isotropic, hard-sphere differential cross section. In contrast, run 33 refers to the correct H_2O cross sections, so that the total cross section increases after the first collision has slowed the H_2O down. Nevertheless, run 54 produced much larger attenuations than did run 33 ($\tau = 0.12$ and 0.43 , respectively), which indicates that an assumed hard-sphere, isotropic differential cross section severely overestimates the role of hard, wide-angle collisions.

As noted earlier, H_2O is expected to return with an approximate thermal-speed distribution characteristic of the outgas source for $\beta > 90^\circ$. In orbit, Orbiter surface temperatures can vary from ~ 200 to 375 K, depending

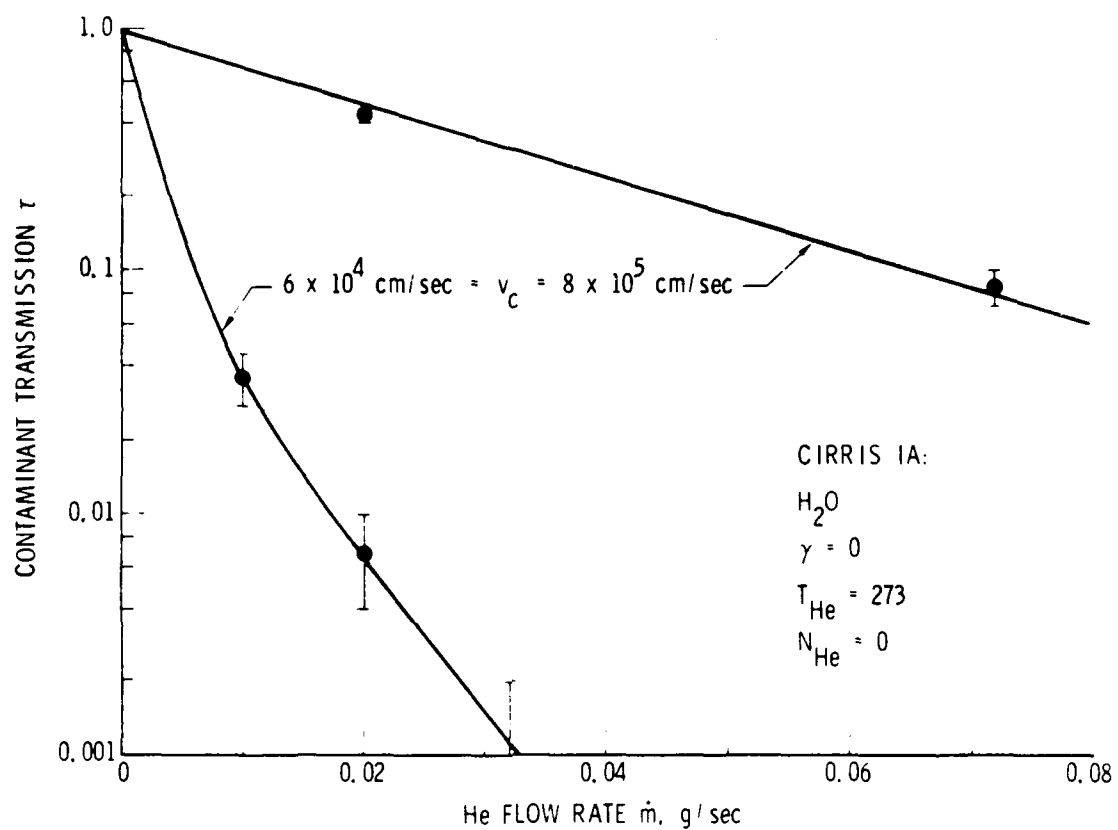


Fig. 10. Transmission of H_2O Contaminant as a Function of He Flow Rate for Two Impingement Speeds v_c , for Runs 33 through 36, 43, and 44

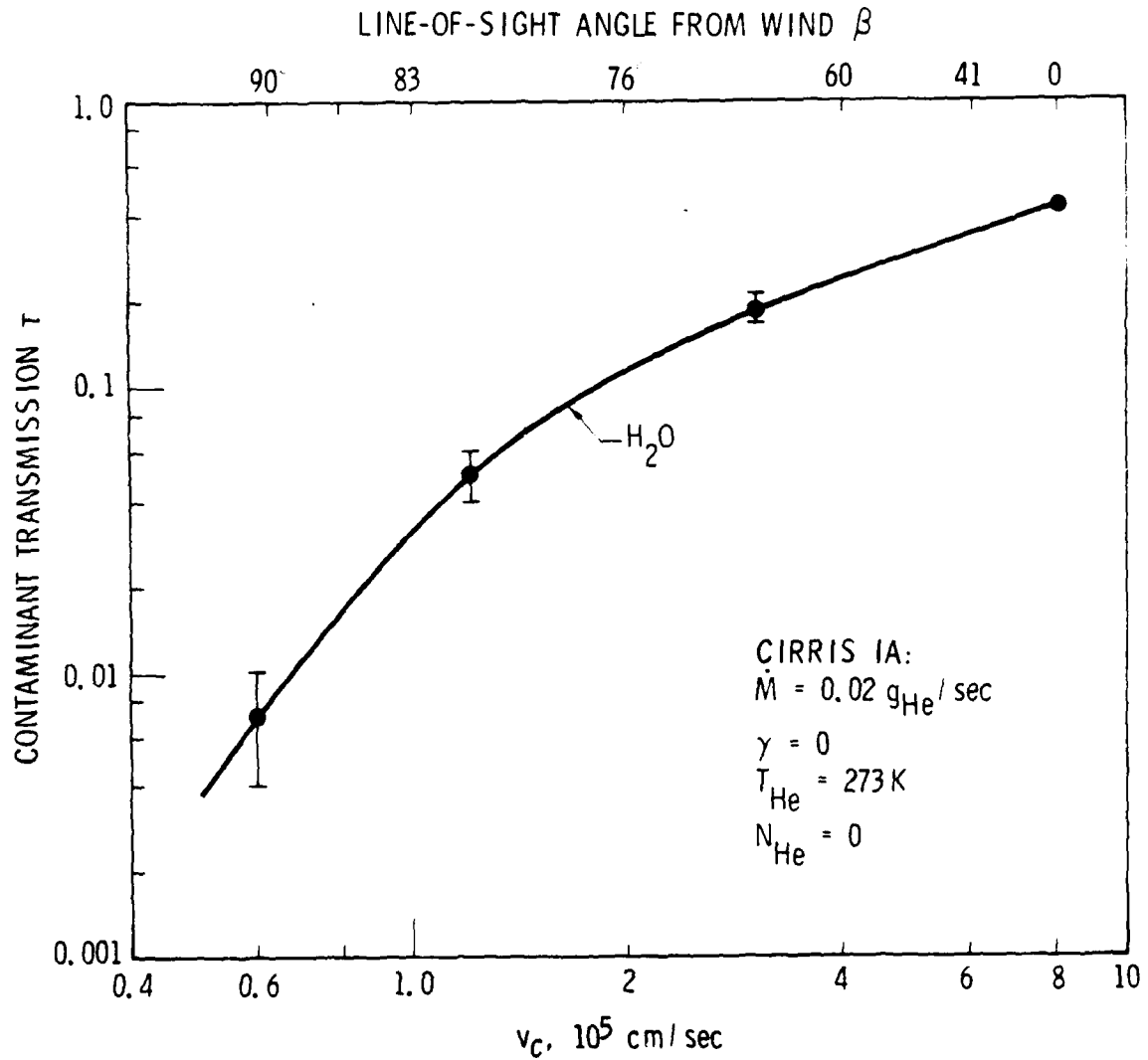


Fig. 11. Transmission of H₂O versus v_c , for Runs 33, 34, 37, 38, 50, and 58. The corresponding angle β , calculated from Eq. (12), is plotted along the top axis.

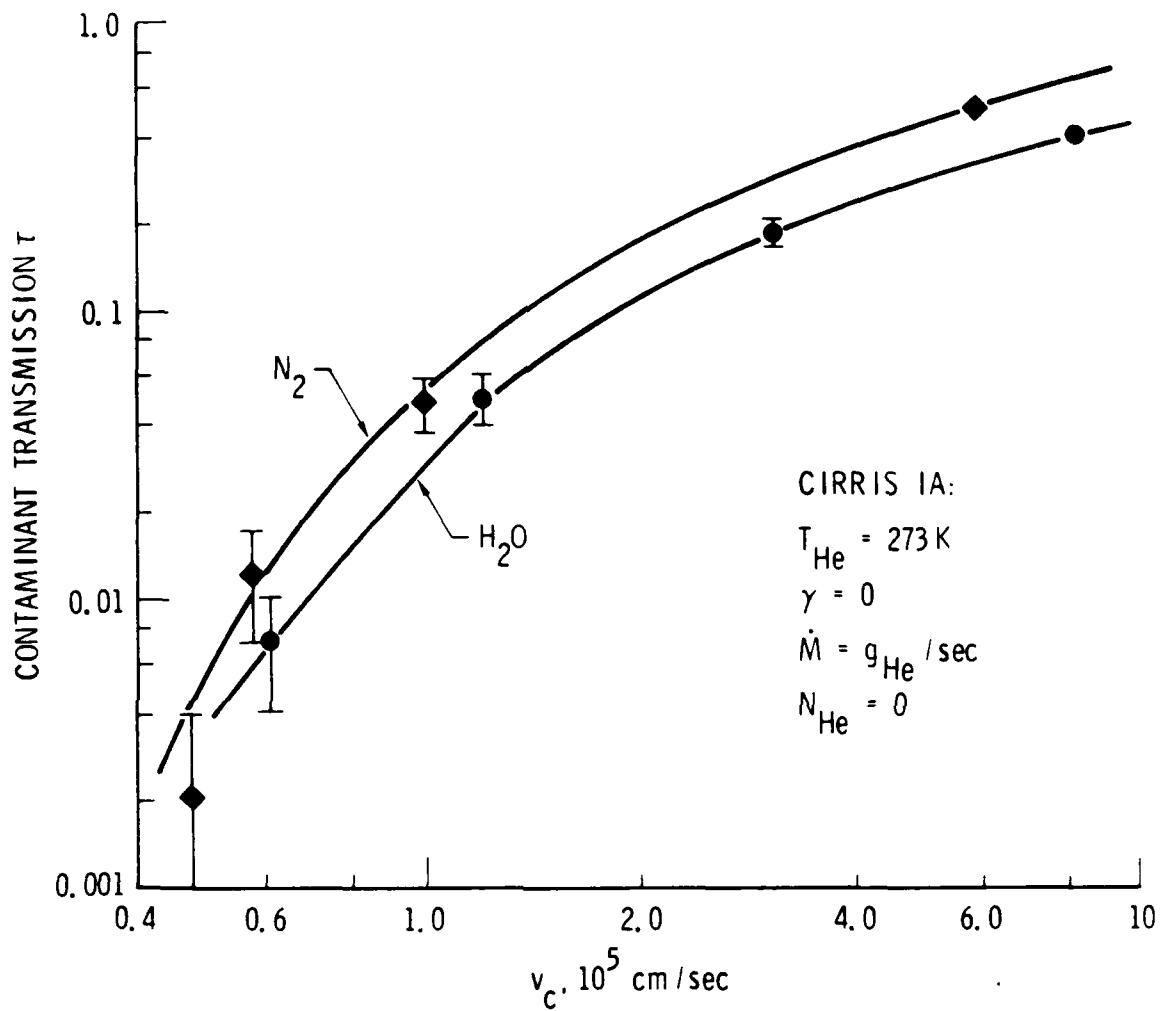


Fig. 12. Transmission versus v_c for H_2O and N_2 . The H_2O results are the same as in Fig. 11; the N_2 results are from runs 39, 49, 52, and 53.

on solar illumination. Figure 11 indicates small transmissions, <0.01 , for average thermal return speeds corresponding to these surface temperatures. In order to test for sensitivity to the high-velocity tail of the Boltzman speed distribution, however, the $\tau(v_c)$ behavior shown in Fig. 11 was averaged over a thermal speed distribution to obtain a thermally averaged transmission $\bar{\tau}$. The results shown in Fig. 13 indicate $\bar{\tau} \lesssim 0.01$ for $T < 375$ K.

In order to evaluate Eqs. (16) and (19), τ and n were evaluated as a function of γ . The results are shown in Figs. 14 and 15 for H_2O and N_2 . Integration of the $\tau(\gamma)$ for H_2O at $v_c = 8 \times 10^5$ cm/sec, shown in Fig. 14, yielded

$$B_{H_2O} = 0.18 \quad (21)$$

The calculations of $\tau(\gamma)$ and B were not carried out at lower H_2O impact speeds because of the very large computation time that would have been required to achieve good statistics. Instead, the value of B given in Eq. (21) was used in evaluating Eqs. (15a) and (17) for the buildup rate of H_2O contaminant film at all v_c values. Again, this should be a conservative estimate, since B would be expected to decrease with decreasing v_c . Runs 33 versus 67 and 34 versus 68 in Table 2 support this expectation, although the statistics are poor. It is also of interest to compare Eq. (21) with a rough estimate of $B = A/L^2$. For the CIRRI IA model employed here, this rough estimate gives $B = 0.09$, whereas it gives $B = 0.04$ if the real CIRRI IA area is used. Again, these comparisons serve to emphasize that the results calculated here overestimate conservatively the actual contamination buildup.

The N_2 acceptance results shown in Fig. 15 indicate a much weaker dependence on γ . Indeed, the He purge has very little effect on acceptance at the highest velocity studied, 5.8×10^5 cm/sec; in the absence of He, the behavior would have been $1.0 \cos \gamma$. Acceptance results for H_2O are included in Fig. 14 to illustrate that this behavior in Fig. 15 is not peculiar to N_2 . Indeed, the results in Fig. 14 illustrate that He does little to prevent fast-impinging contaminants from entering the sensor, but that it does serve to

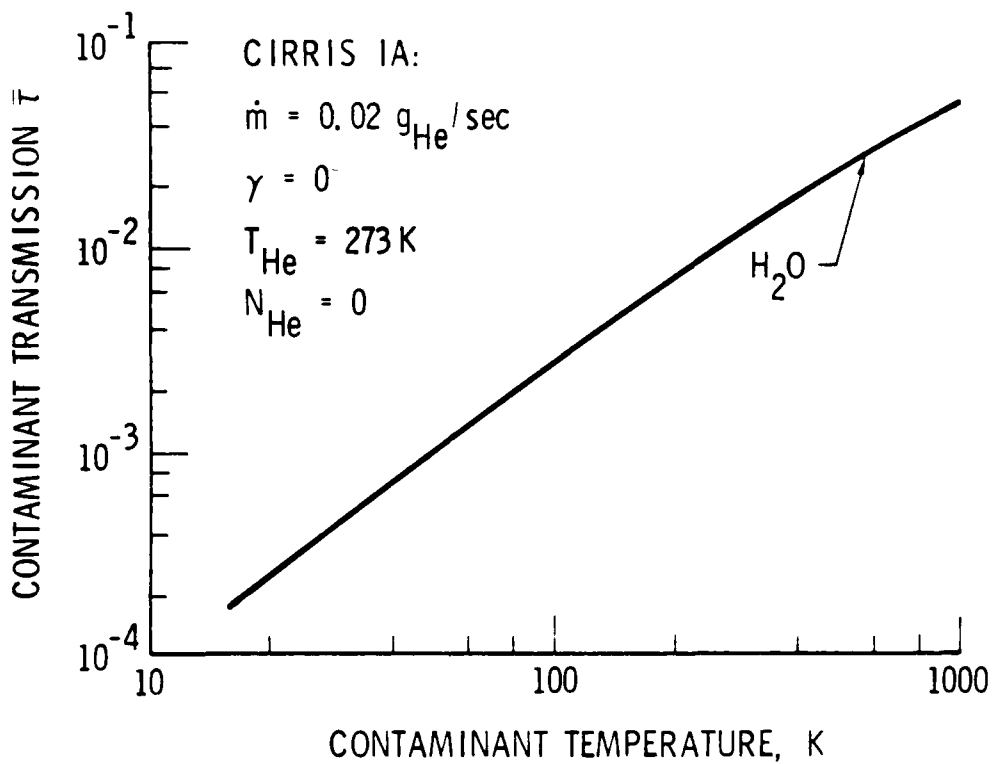


Fig. 13. Thermally Averaged $\bar{\tau}$ for H_2O , Obtained by Averaging the $\tau(v_c)$ Behavior Shown in Fig. 11 over a Thermal Speed Distribution

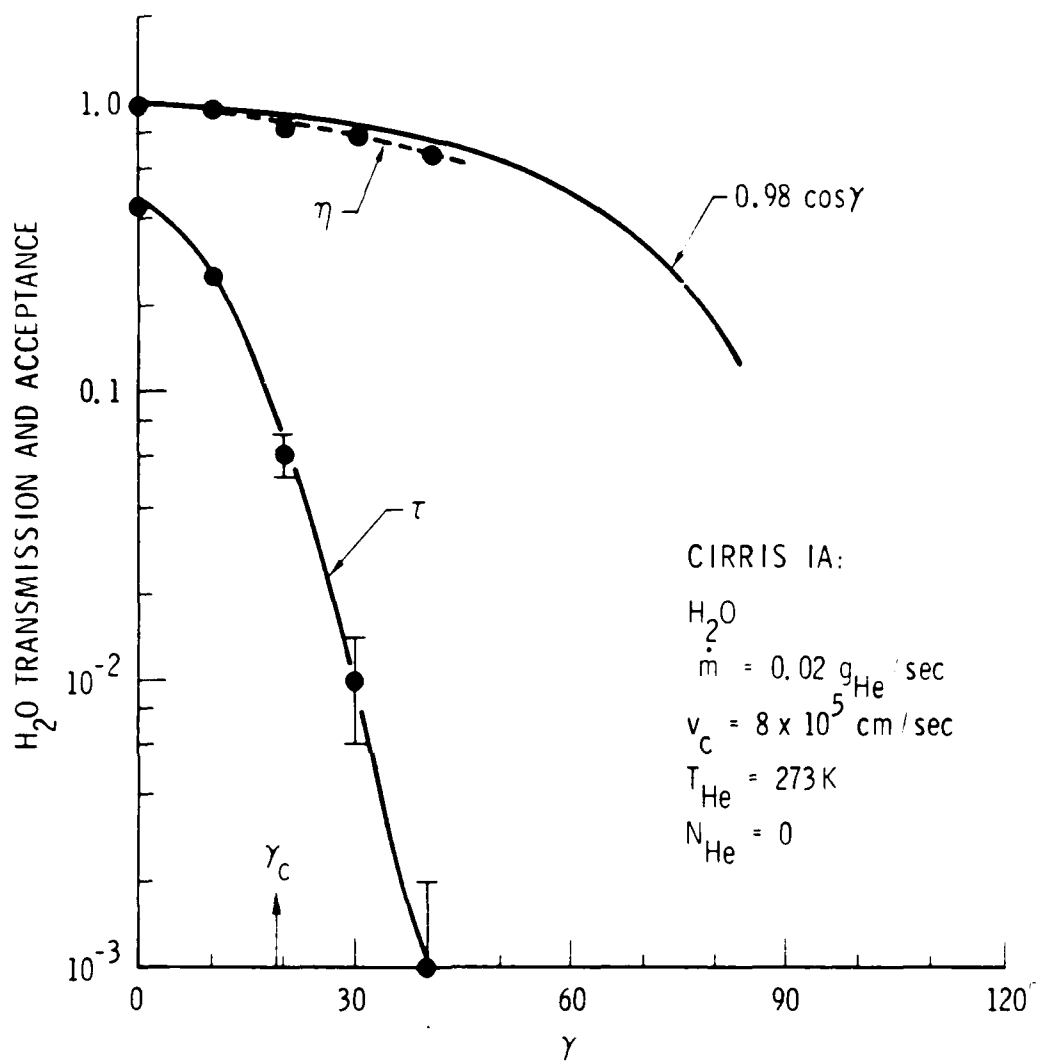


Fig. 14. Transmission and Acceptance versus γ for H_2O for Runs 33 and 64 through 67

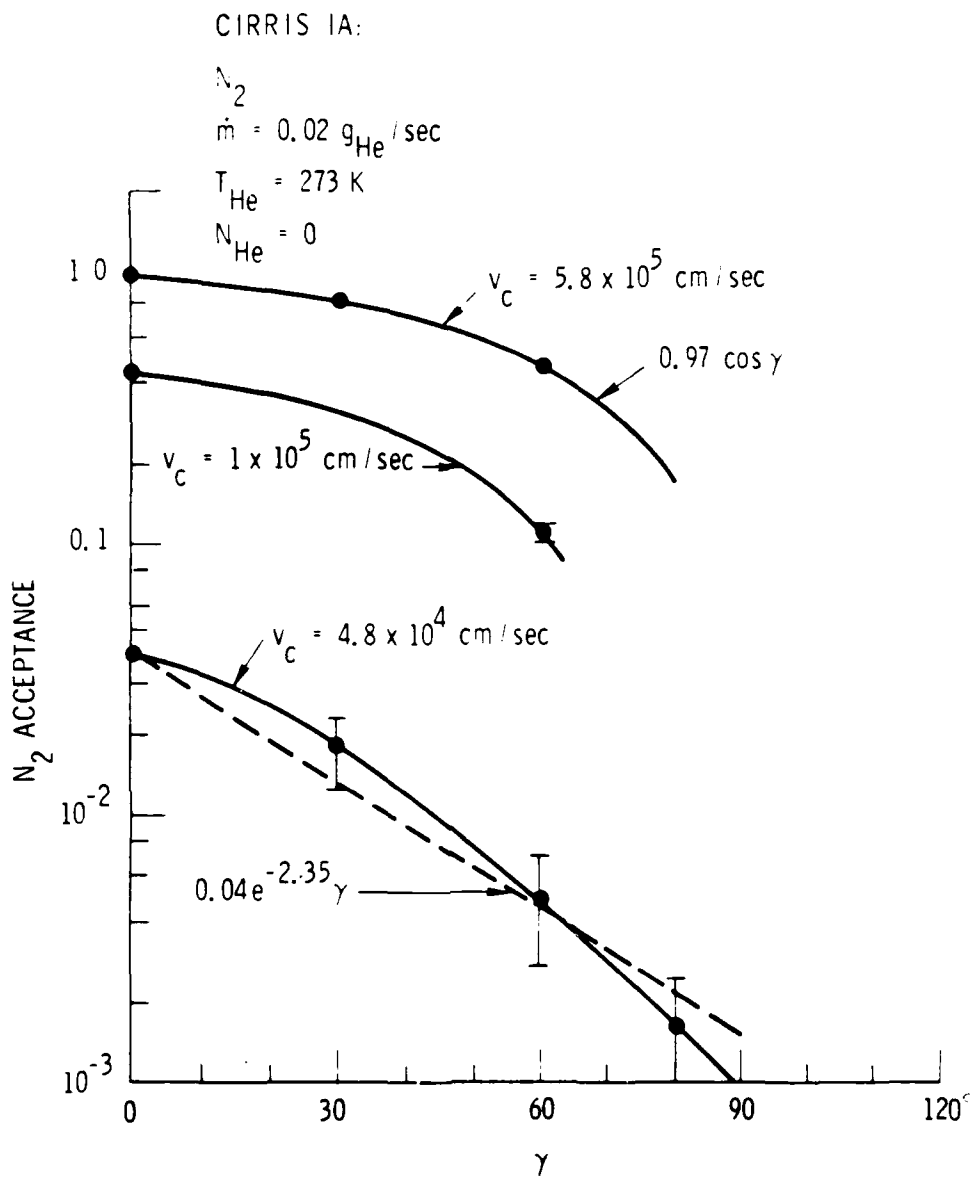


Fig. 15. Acceptance versus γ for N_2 , for Runs 39, 52, 53, 59 through 63, and 69. The dashed line is a fit to the $v_c = 4.8 \times 10^4 \text{ cm/sec}$ data that were used to evaluate Eq. (19).

deflect most of them into the walls. The results in Fig. 15 clearly show that B' of Eq. (19) is 2π at $v_c = 5.8 \times 10^5$ cm/sec. The dashed line fit to the results for $v_c = 4.8 \times 10^4$ cm/sec gives $B' = 0.9$. A functional form was assumed to join these two limits:

$$B'_{N_2} = 0.9 + (5.4 \cos \beta) \quad (22)$$

where β is calculated from Eq. (12).

V. CONTAMINANT BUILDUP RATE AND CONCLUSIONS

Figure 16 shows the buildup of H_2O computed from Eq. (17) with the Orbiter worst-case H_2O environment specified in Eq. (13). For a total H_2O thickness goal of $< \sim 0.01 \mu m$ and a ~ 100 -hr period during which CIRRIS IA will be uncapped on orbit, growth rates of $\dot{t} \lesssim 10^{-4} \mu m/hr$ should be acceptable. Thus, Fig. 16 indicates there is no problem associated with H_2O buildup for the current CIRRIS IA mission plan: $\dot{m} = 0.02 \text{ g}_{He}/\text{sec}$, $\beta = 90$ to 180° , and there are no VCS motor firings. Figure 16 also illustrates that H_2O contamination would increase significantly if the sensor were pointing into the hemisphere containing the incoming wind. The second curve is included in Fig. 16 to illustrate what part of this increase in \dot{t}_{H_2O} with decreasing β is due to the v_c dependence of τ , rather than to the β dependence of f_{H_2O} . The functional dependence of $f_{H_2O}(\beta)$ is essentially unknown except at $\beta = 0$ and 90° . Thus, the true \dot{t} probably lies between the two curves shown in Fig. 16, although it must approach the curve labeled \dot{t} as β goes to 0° . Clearly the CIRRIS IA mission plan is wise; it would be unwise to plan to collect all data at any angle $\beta < 90^\circ$. If, however, it might be desirable to collect some limited data at $\beta < 90^\circ$, Fig. 16 can be used to estimate the corresponding contamination penalty. It is evident that some data collection at angles $\beta < 90^\circ$ would be acceptable.

The acceptance η of N_2 is plotted versus v_c in Fig. 17. This was used in conjunction with $f_{N_2}(\beta)$ from Eq. (14) and $B'_{N_2}(\beta)$ from Eq. (22) to calculate the N_2 steady-state densities (shown in Fig. 18) within CIRRIS IA from Eq. (18). For a CIRRIS IA primary mirror temperature of 20 K, condensation begins at $n_{ss} = 5 \times 10^6 \text{ N}_2 \text{ molecules cm}^{-3}$, or $\beta = 87^\circ$. This figure also indicates that condensation would not take place under any condition at a wall temperature greater than 24 K. Thus, condensation takes place only at the mirror except for some small part of the wall near the mirror which may have temperatures of 20 to 24 K. For small β values, the N_2 film thickness growth rate, calculated from Eq. (20), is shown in Fig. 19. The estimated-safe N_2

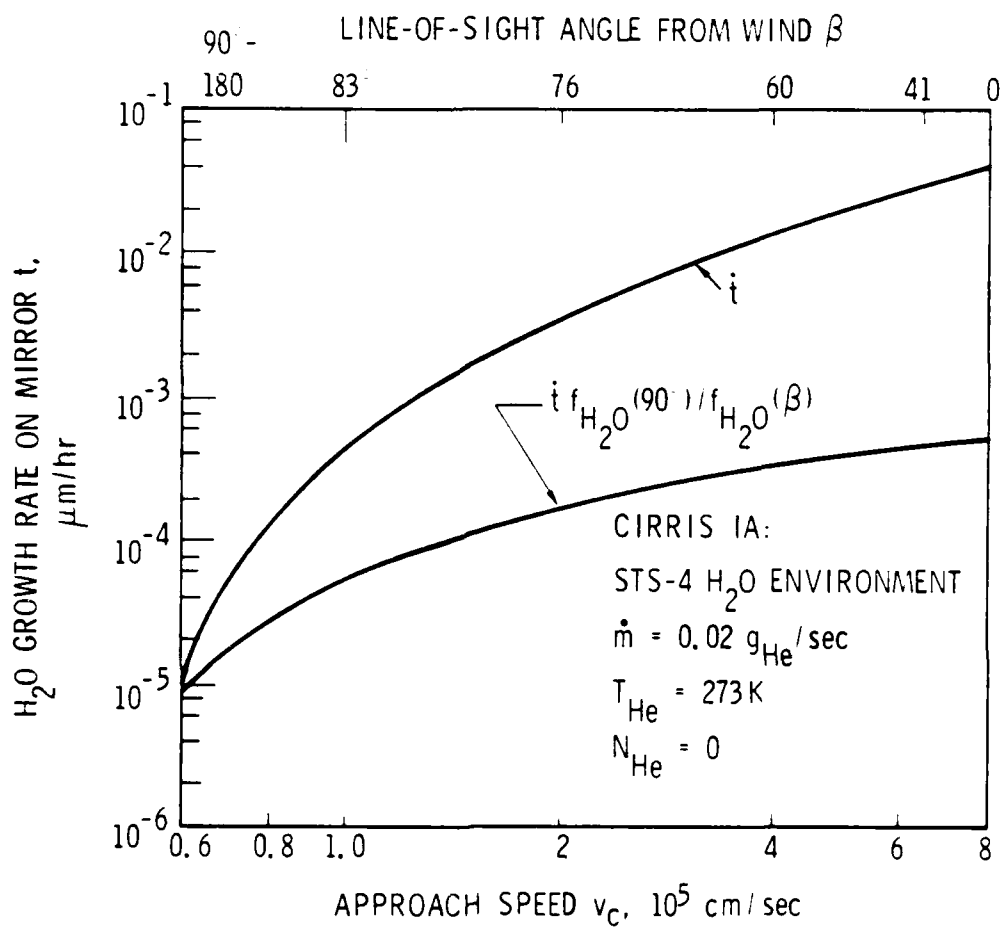


Fig. 16. Buildup of H₂O Contaminant-Film Thickness, Calculated from Eq. (17) for the STS-4 Worst-Case Environment Specified in Eq. (13) and Shown as t . The other curve shows that part of the β dependence which is due to the v_c dependence of τ .

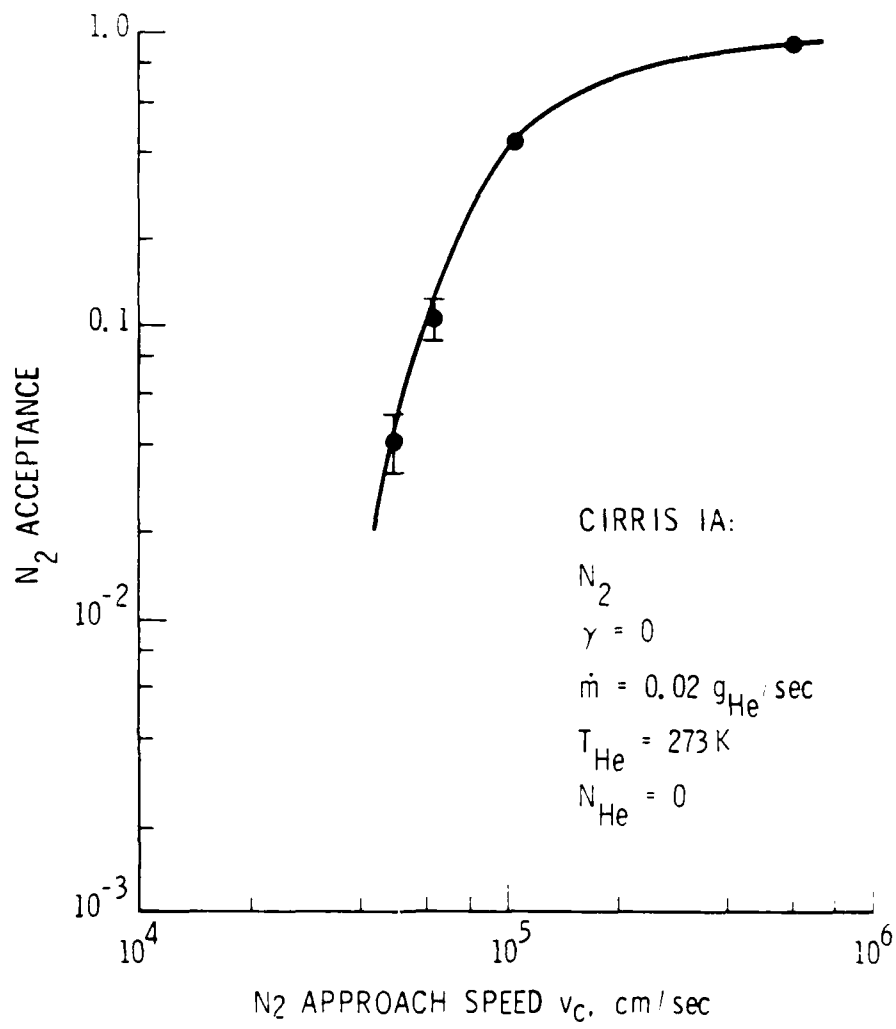


Fig. 17. The Acceptance η for N_2 versus v_c for Runs 39, 49, 52, and 53

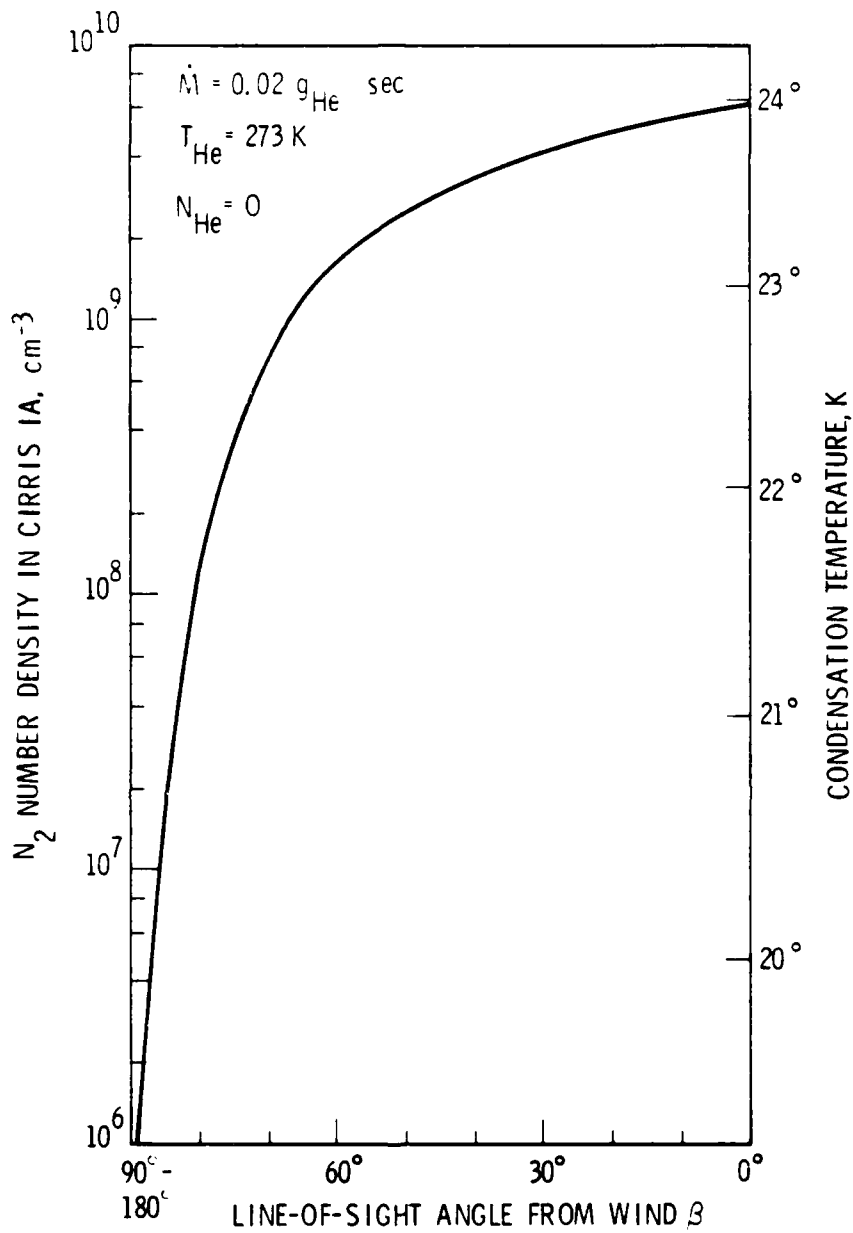


Fig. 18. Steady-State N_2 Density within CIRRIS IA versus β from Eq. (12) for $f_{N_2}(\beta)$ from Eq. (14) and $B_{N_2}(\beta)$ from Eq. (22). The right vertical axis shows the maximum temperature at which the corresponding number density shown on the left axis would produce condensation.

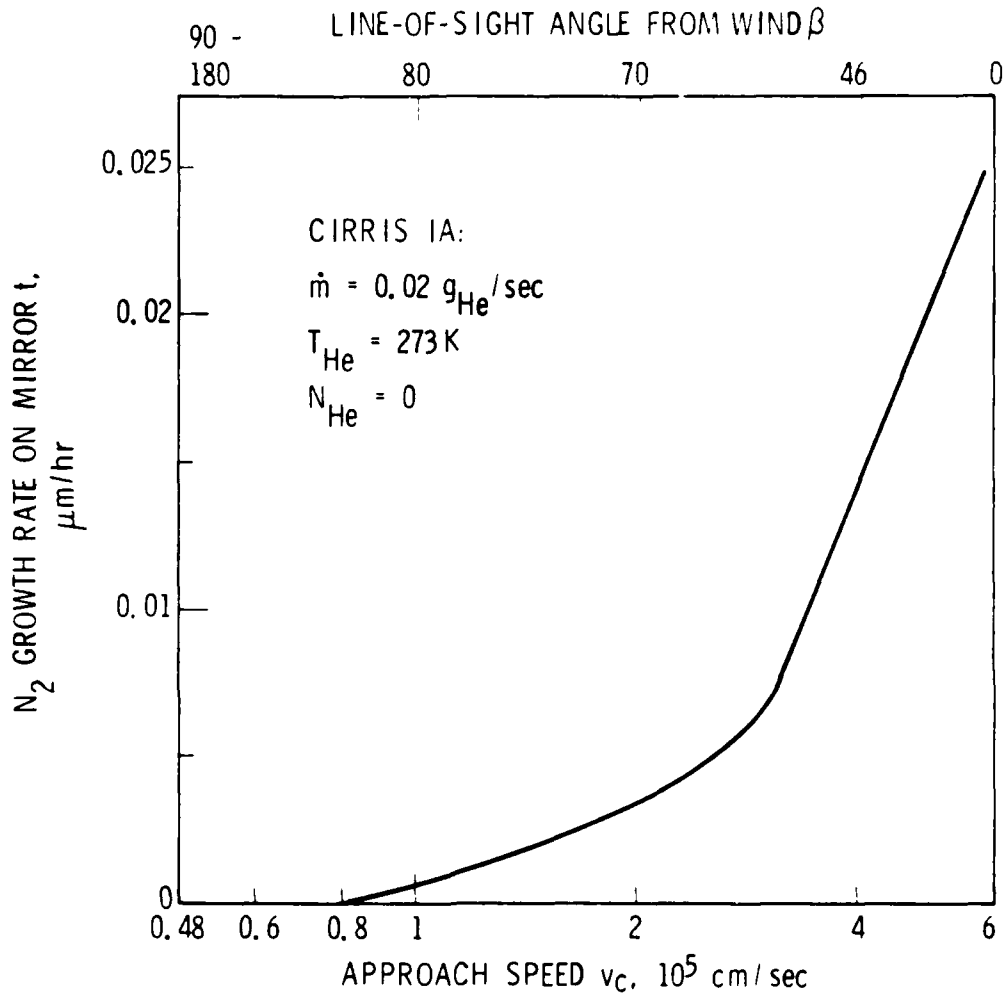


Fig. 19. Growth Rate of N_2 on the CIRRI IA Primary Mirror, Calculated from Eq. (20), for the n_{ss} Dependence Plotted in Fig. 18

thickness discussed earlier was $0.05 \mu\text{m}$, so that \dot{t} should be less than $5 \times 10^{-4} \mu\text{m/hr}$ for a 100-hr mission. Again, the mission constraint of $\beta > 90^\circ$ is well-advised. Figure 19 may be used to estimate the contamination consequences if any data are collected at smaller β angles.

Buildup rates of H_2O and N_2 contaminant films that would be produced by continuous firing of a VCS engine are given in Table 3 for the worst-case return-flux estimates based on observations reported in Ref. 17. As discussed earlier, there is considerable uncertainty, given a large range of possible return speeds and H_2O and N_2 fluxes. As shown in Table 3, this produces a large range of uncertainty in possible contaminant-film buildup rates. The VCS engines are used when the Shuttle Orbiter is not in the stable gravity gradient mode; they are operated in a pulsed mode with a duty factor D_f much less than unity. The corresponding film buildup rate is obtained by multiplying the entry in Table 3 by D_f . For a typical $D_f = 0.01$, the thickness buildup rates \dot{t} given in Table 3 may be read as total buildup^a during the 100 hr that CIRRI IA is uncapped. Even these worst-case estimates indicate that H_2O buildup is not a problem, but that N_2 buildup may be a problem.

A more careful analysis of N_2 buildup requires a detailed consideration of geometry, because v_c and f depend on the location and thrust direction of the VCS engine in relation to the Shuttle Orbiter's attitude and the sensor's line of sight. Table 4 provides such an analysis versus β for a typical case, a CIRRI IA line of sight straight up out of the cargo bay. Return speeds were calculated from conservation of linear momentum and energy for an N_2 plume molecule that returned as a result of a single collision with an O atom. These are only estimates. In reality, a spread of return speeds would be produced because of multiple collision effects and a spread in the intersection angle of the collision partners. Combining the v_c values with the transient N_2 signals reported in Ref. 17 gives the worst-case f_{N_2} and \dot{t} entries in Table 4. Even these worst-case entries indicate that VCS engines

^aIt should be noted that N_2 evaporation while the motor is off is too slow, given the 20 K temperature of the primary mirror, to be of any consequence.

Table 3. Worst-Case Estimates of H₂O and N₂ Growth Rates on the CIRRI IA Primary Mirror Due to the 25-lb-Thrust VCS Engine^a

Species	v_c , 10 ⁵ cm/sec ^b	f , 10 ¹⁴ cm ⁻² sr ⁻¹ sec ⁻¹ ^b	Thickness Buildup \dot{t} , μm/hr
H ₂ O	0.6	0.4	6 × 10 ⁻⁵
H ₂ O	5	4	3 × 10 ⁻²
N ₂	0.5	0.4	2 × 10 ⁻³
N ₂	4	3	1

^aThickness buildup rate refers to continuous engine burn:

$$\dot{m} = 0.02 \text{ g}_{\text{He}}/\text{sec}; T_{\text{He}} = 273 \text{ K}; N_{\text{He}} = 0$$

^bAs discussed in the text, this is the estimated range of possible return speeds and worst-case fluxes.

Table 4. Best Estimates of N_2 Growth Rates on the CIRRIS IA Primary Mirror Due to the 25-1b-Thrust VCS Engine^a

β , deg	$10^5 v_c$, cm/sec ^b	f, Molecules N_2 $10^{13} \text{ cm}^{-2} \text{ sr}^{-1} \text{ sec}^{-1}$		Thickness Buildup \dot{t} , $\mu\text{m/hr}$	
		Worst Case ^c	Best Estimate ^d	Worst Case ^e	Best Estimate ^d
90	3.4	28	1.2	0.8	1×10^{-2}
120	2.5	21	0.4	4.1×10^{-1}	2.5×10^{-3}
150	1.0	8	0.14	5.2×10^{-2}	2.8×10^{-4}
180	-	4	0.09	1.2×10^{-3}	8.4×10^{-6}

^aThickness buildup rate refers to a contiguous single-engine burn for line of sight straight up out of cargo bay: $m = 0.02 \text{ g}_{\text{He}}/\text{sec}$, $T_{\text{He}} = 273 \text{ K}$, $N_{\text{He}} = 0$.

^bEstimate for single plume O-atom collision. v_c actually depends on the location of the particular VCS engine relative to the velocity vector. Entries given are for the engine that gives the largest v_c . A single collision cannot return N_2 along $\beta = 180^\circ$. $v_c = 5 \times 10^4 \text{ cm/sec}$ was used for $\beta = 180^\circ$.

^cf is based upon the transient N_2 signal measured in Ref. 17.

^df is calculated from Refs. 20 and 27, as described in the text.

can be safely fired at $D_f = 0.01$ during the entire CIRRIS IA mission so long as $\beta \gtrsim 150^\circ$. Moreover, the best-estimate entries in Table 4 indicate that contamination buildup due to VCS engine firings at a typical $D_f = 0.01$ will be inconsequential so long as the sensor is looking into the aft hemisphere, i.e., if $\beta > 90^\circ$. These best estimates were calculated by extrapolating the $\beta = 0$ to 80° calculations reported in Ref. 20 with the approximate $\beta = 0$ to 180° return flux angular distribution reported in Ref. 27. Work reported in Ref. 28 indicates that even this should overestimate the N_2 return flux at these large β angles, because N_2 is heavier than the O atom collision partner.

REFERENCES

1. See, for example, J. P. Simpson and F. C. Witteborn, "Effects of the Shuttle Contaminant Environment on a Sensitive Infrared Telescope," Appl. Opt. 16, 2051 (1977).
2. A. Guttman, R. D. Furber, and E. P. Muntz, "Protection of Satellite Infrared Experiment (SIRE) Cryogenic Infrared (IR) Optics in Shuttle Orbiter," in Optics in Adverse Environment, M. A. Kahan, ed., Proceedings SPIE, Vol. 216 (1980), pp. 174-185.
3. N. M. Harvey and R. R. Herm, "Helium Purge-Flow Prevention of Atmospheric Contamination of the Cryogenically Cooled Optics of Orbiting Infrared Telescopes: Calculations of He-O Differential Cross Section," USAF Space Division Report SD-TR-81-53 (5 June 1981); Int. J. Engng. Sci. 21, 349 (1983).
4. E. P. Muntz and M. Hanson, "Studies of the Purging Flow Protection of Infrared Telescopes," AIAA Paper 82-0294, AIAA 20th Aerospace Sciences Meeting, Orlando, Fla. (11-14 January 1982); "Purging-Flow Protection of Infrared Telescopes," AIAA Journal 22, 696 (1984).
5. A. Guttman and R. D. Furber, "Technical Operating Report (TOR) on Contamination Control for SIRE: Final Report," Report FR-82-77-562, Hughes Aircraft Company, Culver City, Calif. (February 1982).
6. M. Keil, J. T. Slankas, and A. Kuppermann, "Scattering of Thermal He Beams by Crossed Atomic and Molecular Beams. III. Anisotropic Interaction Potentials for He + N₂, O₂, CO, and NO," J. Chem. Phys. 70, 541 (1979).
7. J. T. Slankas, M. Keil, and A. Kuppermann, "Scattering of Thermal He Beams by Crossed Atomic and Molecular Beams. IV. Spherically Symmetric Intermolecular Potentials for He + CH₄, NH₃, H₂O, SF₆," J. Chem. Phys. 70, 1482 (1979).
8. G. A. Parker, M. Keil, and A. Kupperman, "Scattering of Thermal He Beams by Crossed Atomic and Molecular Beams. V. Anisotropic Intermolecular Potentials for He + CO₂, N₂O, C₂N₂," J. Chem. Phys. 78, 1145 (1983).
9. G. A. Parker and R. T. Pack, "Rotationally and Vibrationally Inelastic Scattering in the Rotational IOS Approximation: Ultrasimple Calculation of Total (Differential, Integral, and Transport) Cross Sections for Nonspherical Molecules," J. Chem. Phys. 68, 1585 (1978).
10. J. M. Hammersley and D. C. Handscomb, Monte Carlo Methods, Chapman and Hall (London, 1979).

11. J. Spanier and E. M. Gelbard, Monte Carlo Principles and Neutron Transport Problems, Addison-Wesley (Reading, Mass., 1969).
12. K. Binder and H. K. V. Lotsch, Monte Carlo Methods in Statistical Physics, Springer-Verlag (New York, 1979).
13. G. A. Bird, Molecular Gas Dynamics, Clarendon Press (London, 1976).
14. R. O'Neill and R. Nadile, Private communication (6 July 1983).
15. B. R. Johnson, S. J. Young, and R. R. Herm, to be published.
16. G. R. Carignan and E. R. Miller, "Mass Spectrometer," in STS-2, -3, -4 Induced Environment Contamination Monitor Summary Report, NASA TM-82524 (February 1983), pp. 87-101.
17. R. Narcisi, E. Trzcinski, G. Federico, L. Wlodyka, and D. Delorey, "The Gaseous and Plasma Environment around Space Shuttle," AIAA Shuttle Environment and Operations Meeting, Washington, DC (31 Oct. - 2 Nov. 1983), AIAA Paper 83-2659, pp. 183-190.
18. L. Leger, S. Jacobs, and H. K. F. Ehlers, "Space Shuttle Contamination Overview," J. Environ. Sci. (September/October 1978), pp. 28-33.
19. J. A. Muscari, D. Mah, and R. Somers, "Satellite Contamination. II. SIRE Modeling," Martin Marietta Aerospace, MCR-80-629 (October 1980).
20. H. K. F. Ehlers, "An Analysis of Return Flux from the Space Shuttle Orbiter RCS Engines," AIAA Paper 84-0551, AIAA 22nd Aerospace Sciences Meeting, Reno, Nevada (9-12 January 1984).
21. J. J. Scialdone, "Shuttle Measured Contaminant Environment and Modeling for Payloads," AIAA Shuttle Environment and Operations Meeting, Washington, DC, (31 Oct. - 2 Nov. 1983), AIAA Paper 83-2583-CP.
22. R. E. Honig and H. O. Hook, "Vapor Pressure Data for Some Common Gases," RCA Review 21, 360 (1960).
23. J. M. Dowling, Private communication.
24. M. Ahmadjian, D. R. Smith, A. T. Stair, and K. Baker, "CIRRIS - A Cryogenic Infrared (IR) Radiance Instrument for Shuttle," in Infrared Astronomy-Scientific/Military Thrusts & Instrumentation, N. W. Bogges and H. J. Stears, eds., Vol. 280, SPIE Proceedings (1981), pp. 45-53.
25. F. Arnold, "Degradation of Low-Scatter Metal Mirrors by Cryodeposit Contamination," AEDC-TR-75-128 (11 October 1975).
26. Y. Wang and W. L. Wolfe, "Scattering from Microrough Surfaces: Comparison of Theory and Experiment," J. Opt. Soc. Am. 73, 1596 (1983).

27. S. J. Robertson, "Bhatnagar-Gross-Krook Model Solution of Back-Scattering of Outgas Flow from Spherical Spacecraft," in Progress in Astronautics and Aeronautics, Vol. 51, Part 1, AIAA (New York, 1977), pp. 479-489.
28. G. A. Bird, "Spacecraft Outgas Ambient Flow Interaction," J. Spacecraft 18, 31 (1981).

APPENDIX

Differential cross sections have been calculated by the method described in Ref. 3 for the scattering of He atoms by H₂O, N₂, CO, and CO₂. Results are presented here as plots of $\sigma(\theta, v)$, in units of Å²/sr, as a function of polar scattering angle θ . Some plots are presented versus collision energy, $E = \mu v^2/2$, rather than collision speed. For completeness, results on He-O are also included here. The He-O potential function given here is correct; there is an error in the potential function that appears in Ref. 3.

Potential Energy Functions

For He + O(³P):

$$V(r) = \tanh(ar^{-6}) V^F(r) + \tanh(br^6) V^A(r)$$

where:

$$V^F(r) = Ae^{-\beta r}$$

$$V^A(r) = \epsilon \left[\frac{6}{\alpha - 6} \exp\{-a[(r/r_m)-1]\} - \frac{\alpha}{\alpha - 6} \left(\frac{r}{r_m}\right)^{-6} \right]$$

and where

$$\begin{aligned} a &= 102.0 \text{ bohr}^6 \\ b &= 0.001 \text{ bohr}^{-6} \\ A &= 378 \text{ eV} \\ \beta &= 3.744 \text{ \AA}^{-1} \\ \epsilon &= 2.48 \times 10^{-3} \text{ eV} \\ \alpha &= 13.772 \\ r_m &= 3.08 \text{ \AA} \end{aligned}$$

For He + CO and He + N₂:

Both potentials⁶ are a parametrized form called the Simons-Parr-Finlan-Dunham (SPFD) potential given by

$$V(r) = \epsilon \left[b_0 \left(\frac{r - r_m}{r_m} \right)^2 \sum_{i=1}^3 b_i \left(\frac{r - r_m}{r_m} \right)^i - 1 \right]; \frac{r}{r_m} < 1.6$$
$$= - \epsilon C_6 \left(\frac{r}{r_m} \right)^{-6} \quad \frac{r}{r_m} > 1.6$$

The parameters are

	<u>He + CO</u>	<u>He + N₂</u>
r_m	3.70 Å	3.65 Å
ϵ	2.28×10^{-3} eV	2.27×10^{-3} eV
b_0	39.2	31.9
b_1	- 5.10	- 4.72
b_2	11.31155006	10.05959840
b_3	- 9.73209667	- 8.52603029
C_6	1.52	2.10

(b_2 and b_3 are determined by smoothness conditions.)

For He + H₂:

This is also an SPFD potential⁷ with the following parameters:

r_m	3.38 Å
ϵ	2.27×10^{-3} eV
b_0	31.4
b_1	- 6.15
b_2	17.6202007
b_3	-18.5110554
C_6	2.30

For He + CO₂:

This potential is a Morse-Spline-Van der Waals (MSV) potential⁸ with parameters that are functions of the angle γ , as follows:

$$V(r, \gamma) = \epsilon \exp[-\beta(r - r_m)/r_m] \{ \exp[-\beta(r - r_m)/r_m] - 2 \} \quad (r < r_1)$$

$$V(r, \gamma) = (r_2 - r) [S_1(r_2 - r)^2 + S_3] + (r - r_1) [S_2(r - r_1)^2 + S_4] \quad (r_1 < r < r_2)$$

$$V(r, \gamma) = -\frac{C_6}{r^6} - \frac{C_8}{r^8} \quad (r > r_2)$$

where

$$\epsilon = \epsilon_0 + \epsilon_2 P_2(\cos \gamma)$$

$$r_m = r_{m0} + r_{m2} P_2(\cos \gamma)$$

$$C_6 = C_6(0) + C_6(2) P_2(\cos \gamma)$$

$$C_8 = C_8(0) + C_8(2) P_2(\cos \gamma)$$

The function $P_2(\cos \gamma)$ is the second-order Legendre polynomial and the values of the parameters are

$$\epsilon_0 = 1.05 \text{ meV}$$

$$\epsilon_2 = -0.67 \text{ meV}$$

$$r_{m0} = 3.84 \text{ \AA}$$

$$r_{m2} = 0.99 \text{ \AA}$$

$$C_6(0) = 9.98 \text{ eV \AA}^6$$

$$C_6(2) = 2.31 \text{ eV \AA}^6$$

$$C_8(0) = 46.4 \text{ eV \AA}^8$$

$$C_8(2) = 48.4 \text{ eV \AA}^8$$

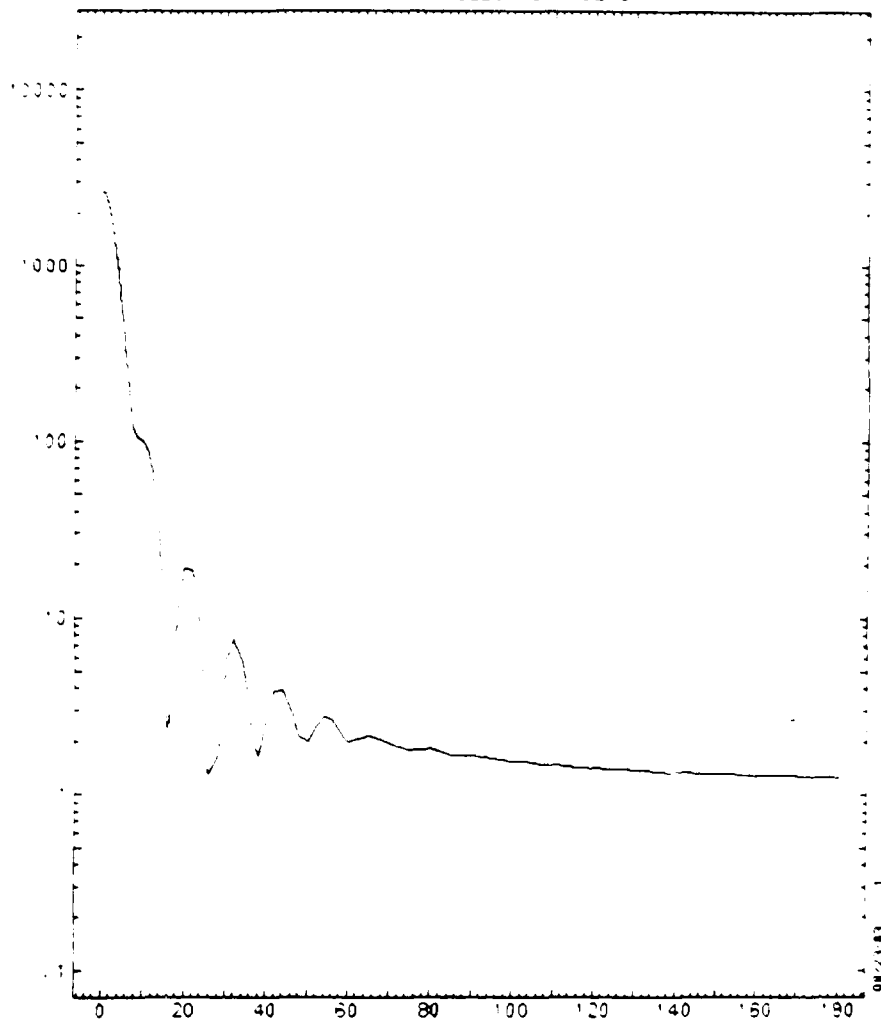
$$\beta = 4.59$$

$$r_1 = \left(1 + \frac{\ln(2)}{\beta}\right) r_m$$

$$r_2 = 1.6 r_m$$

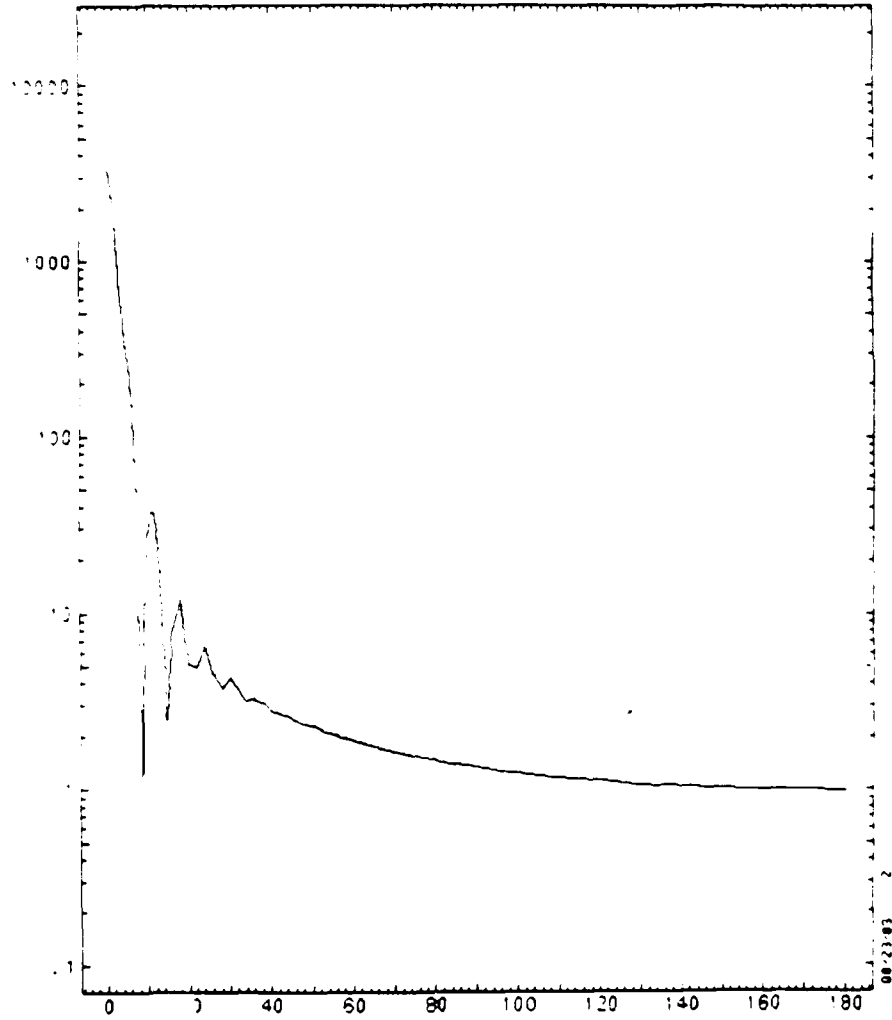
The spline parameters S_1 , S_2 , S_3 , and S_4 are determined by smoothness conditions at r_1 and r_2 ; i.e., the potential and its first derivative are continuous at these points.

EN = 102 ELECTRON VOLTS



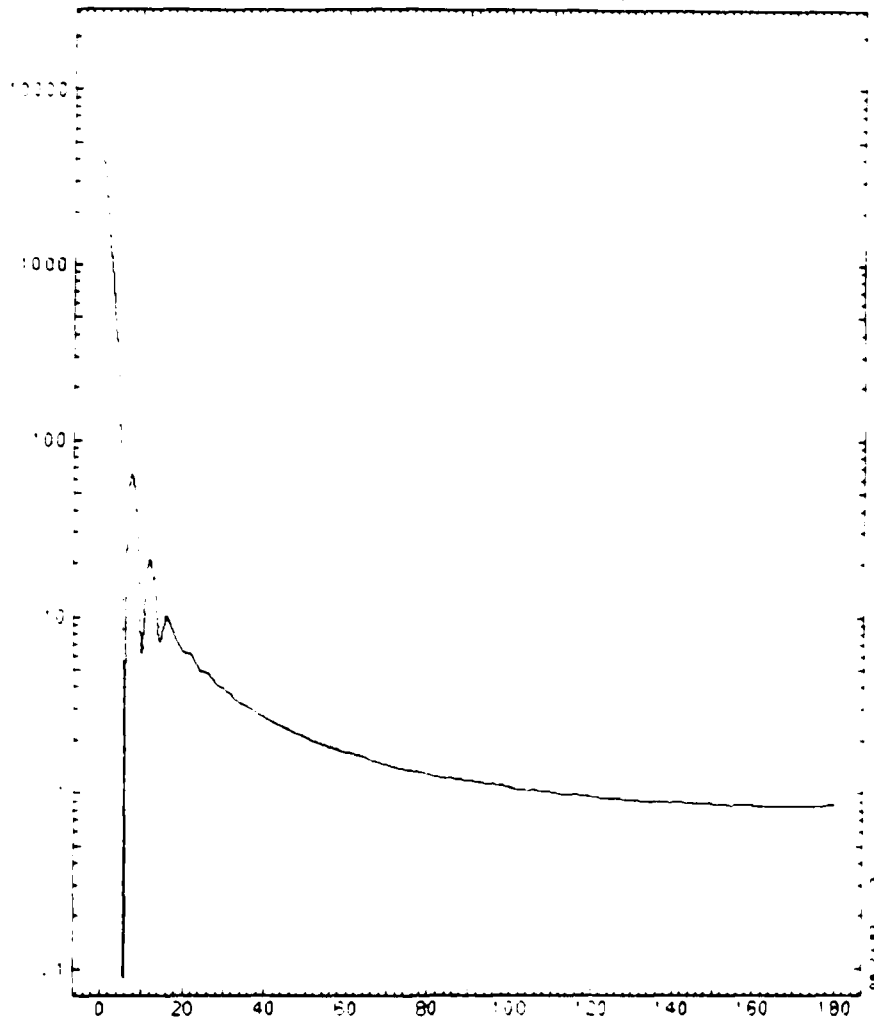
HELIUM - OXYGEN DIFFERENTIAL CROSS SECTION

EN = .07 ELECTRON VOLTS



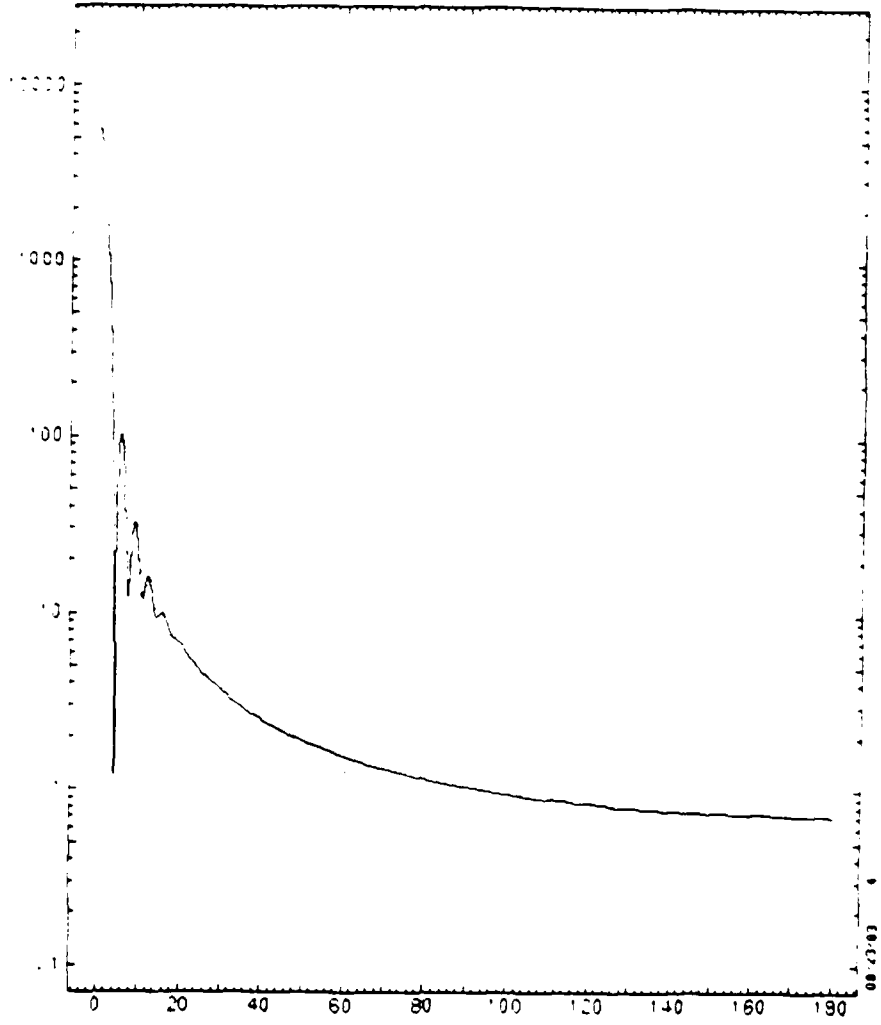
HELIUM - OXYGEN DIFFERENTIAL CROSS SECTION

EN = .15 ELECTRON VOLTS

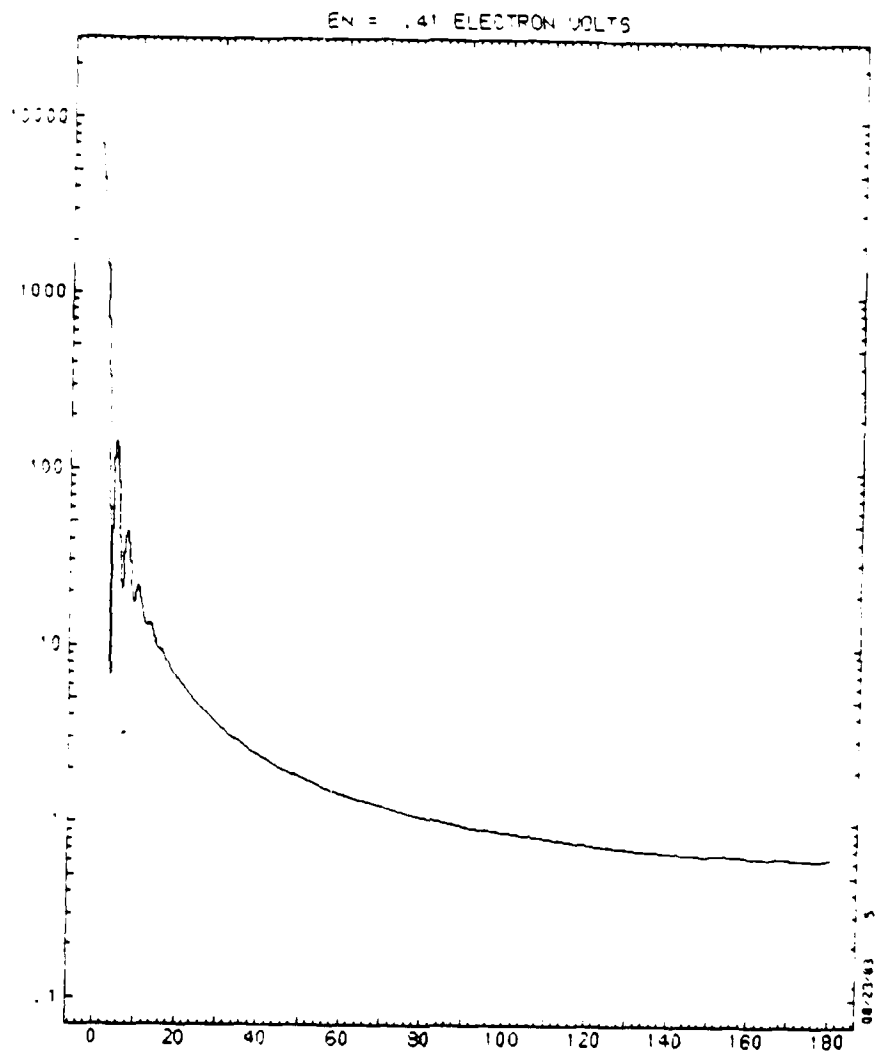


HELIUM - OXYGEN DIFFERENTIAL CROSS SECTION

EN = 1.27 ELECTRON VOLTS

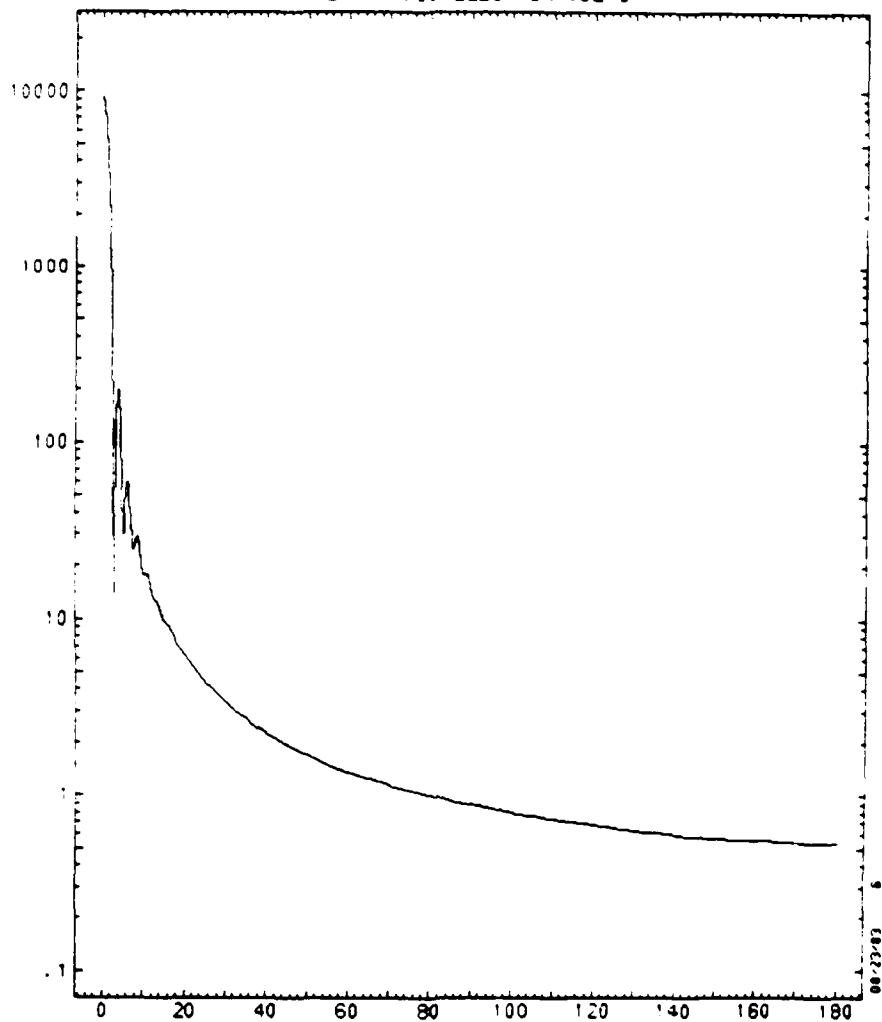


HELIUM - OXYGEN DIFFERENTIAL CROSS SECTION



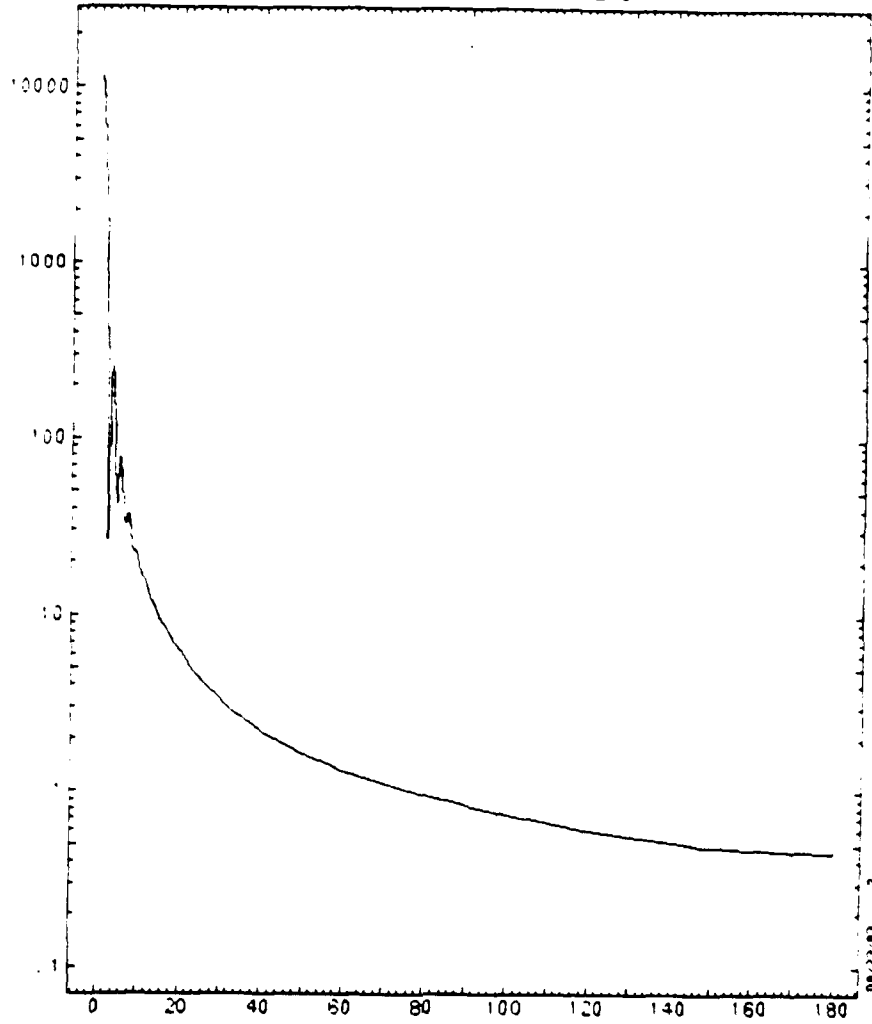
HELIUM - OXYGEN DIFFERENTIAL CROSS SECTION

EN = .60 ELECTRON VOLTS



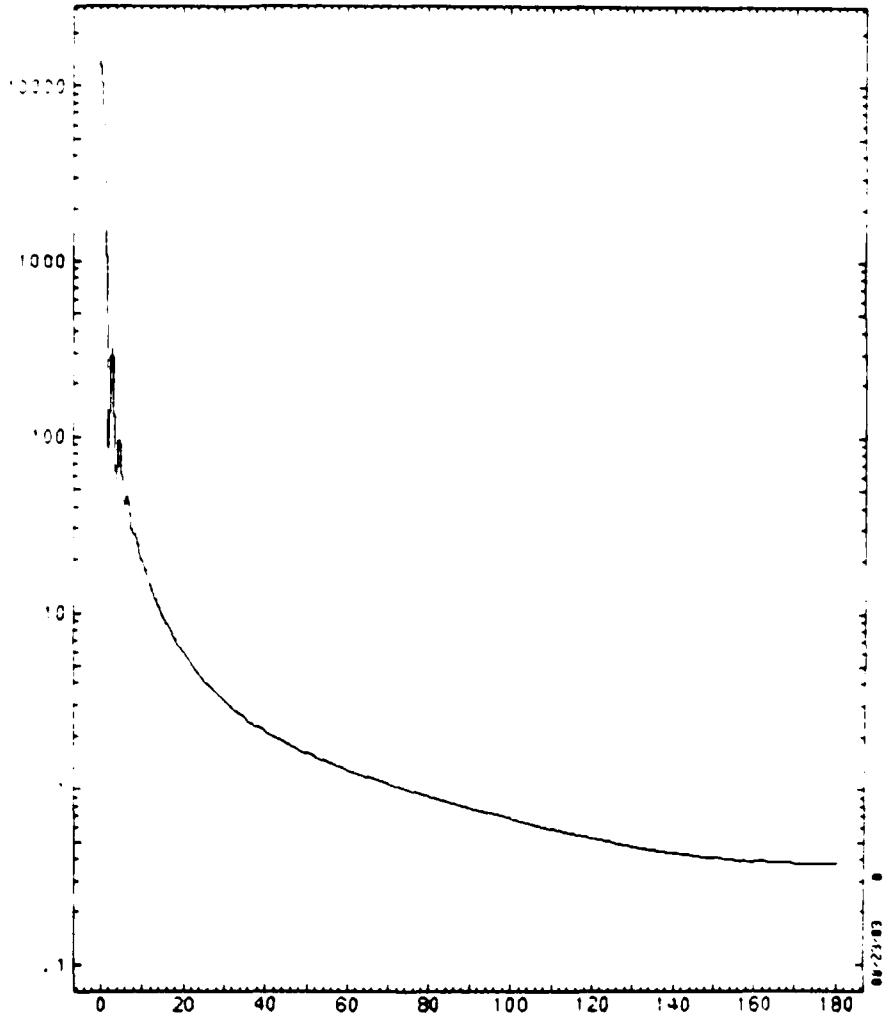
HELIUM - OXYGEN DIFFERENTIAL CROSS SECTION

EN = .81 ELECTRON VOLTS



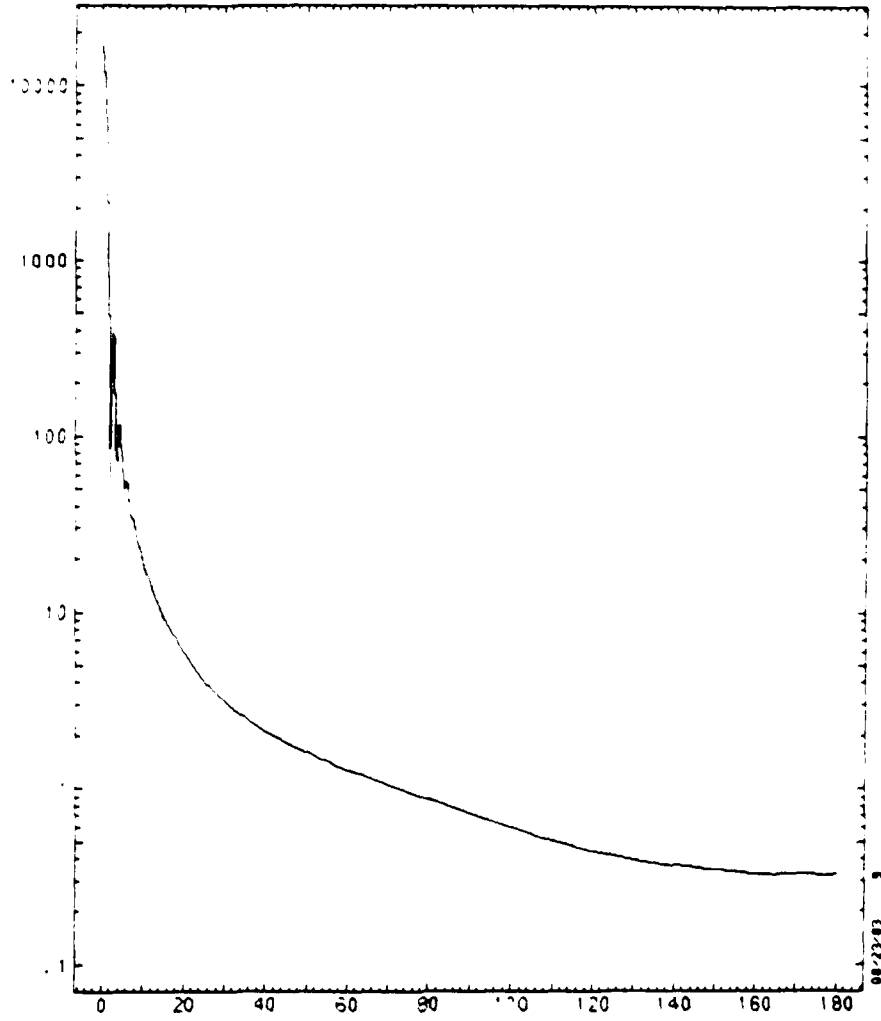
HELIUM - OXYGEN DIFFERENTIAL CROSS SECTION

EN = 1.06 ELECTRON VOLTS



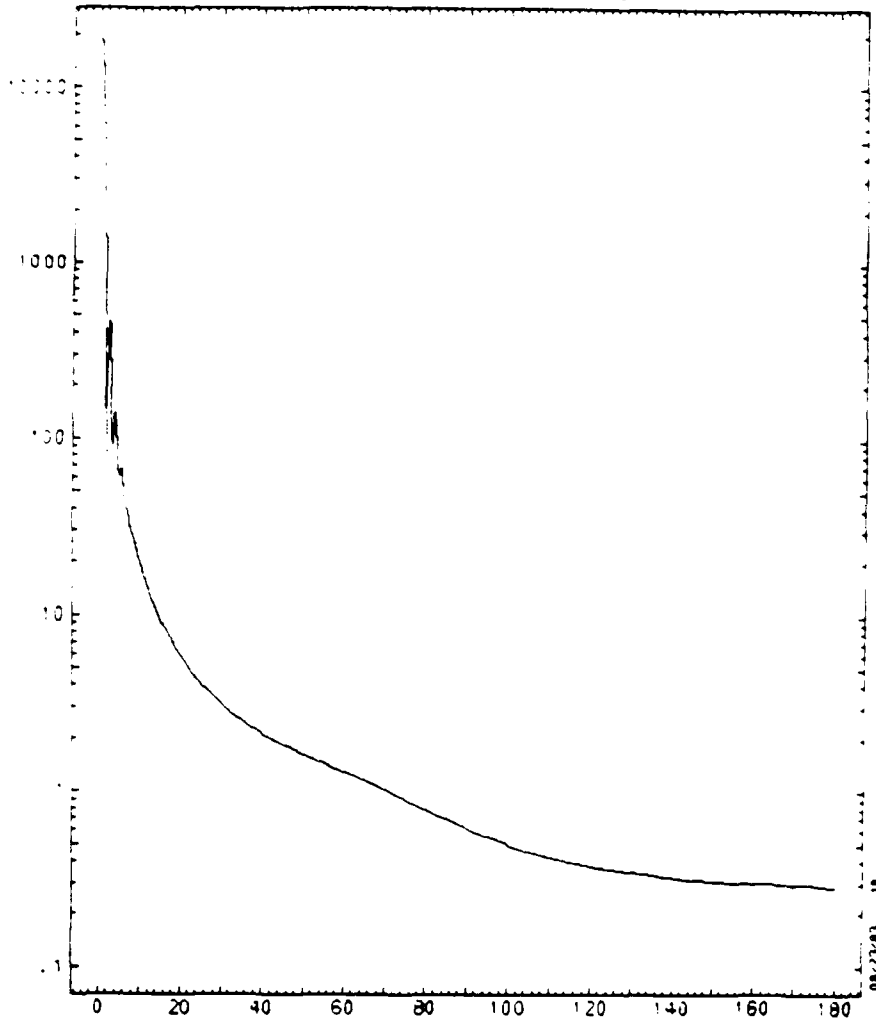
HELIUM - OXYGEN DIFFERENTIAL CROSS SECTION

EN = 1.34 ELECTRON VOLTS

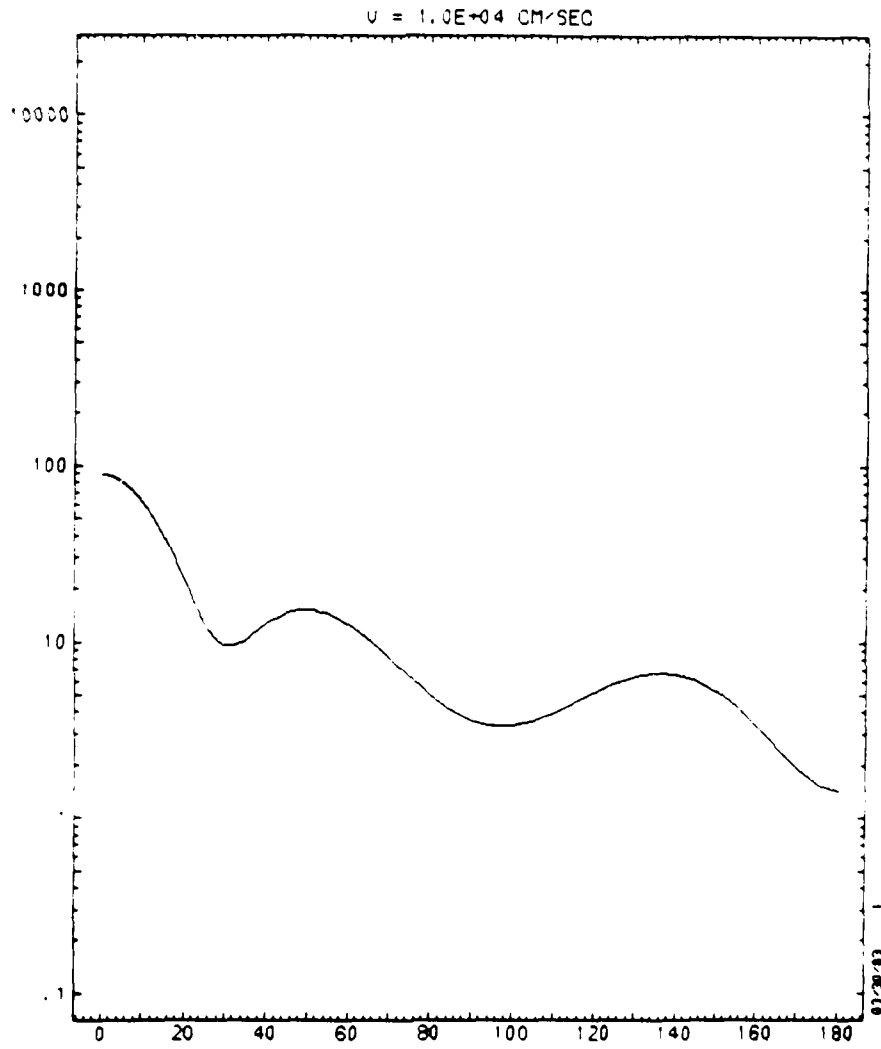


HELIUM - OXYGEN DIFFERENTIAL CROSS SECTION

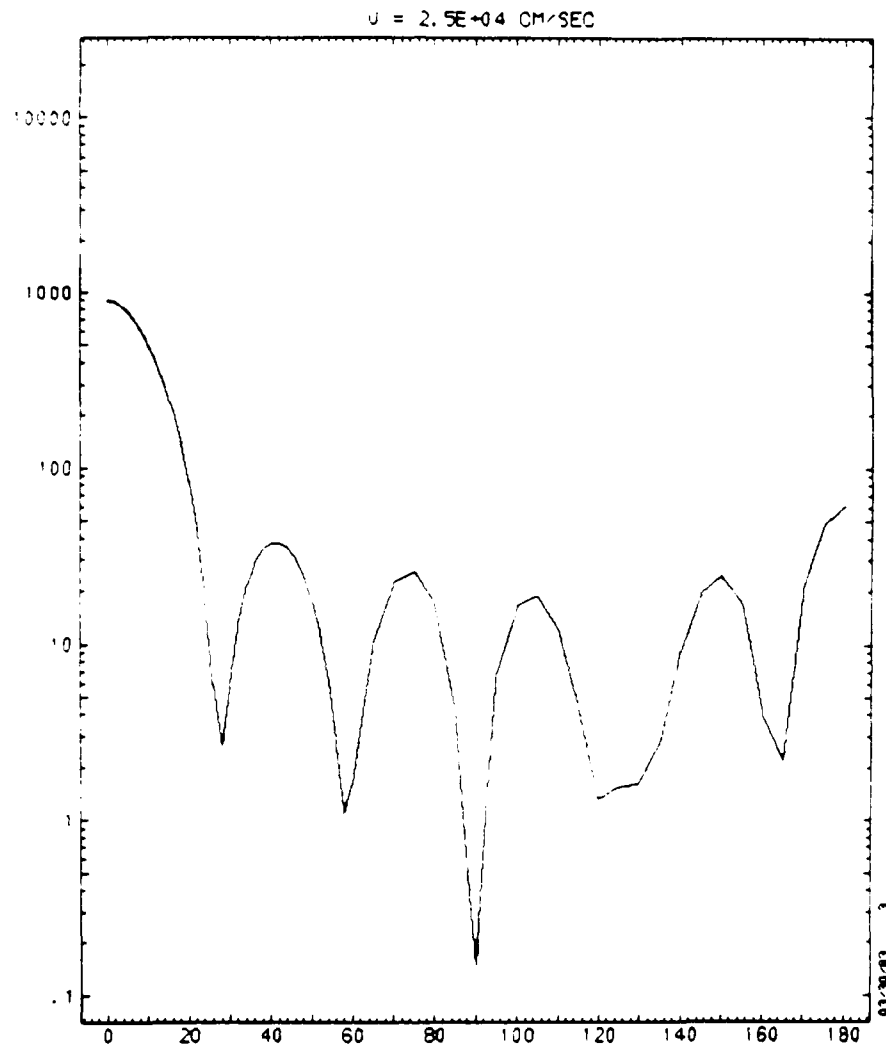
EN = 1.86 ELECTRON VOLTS



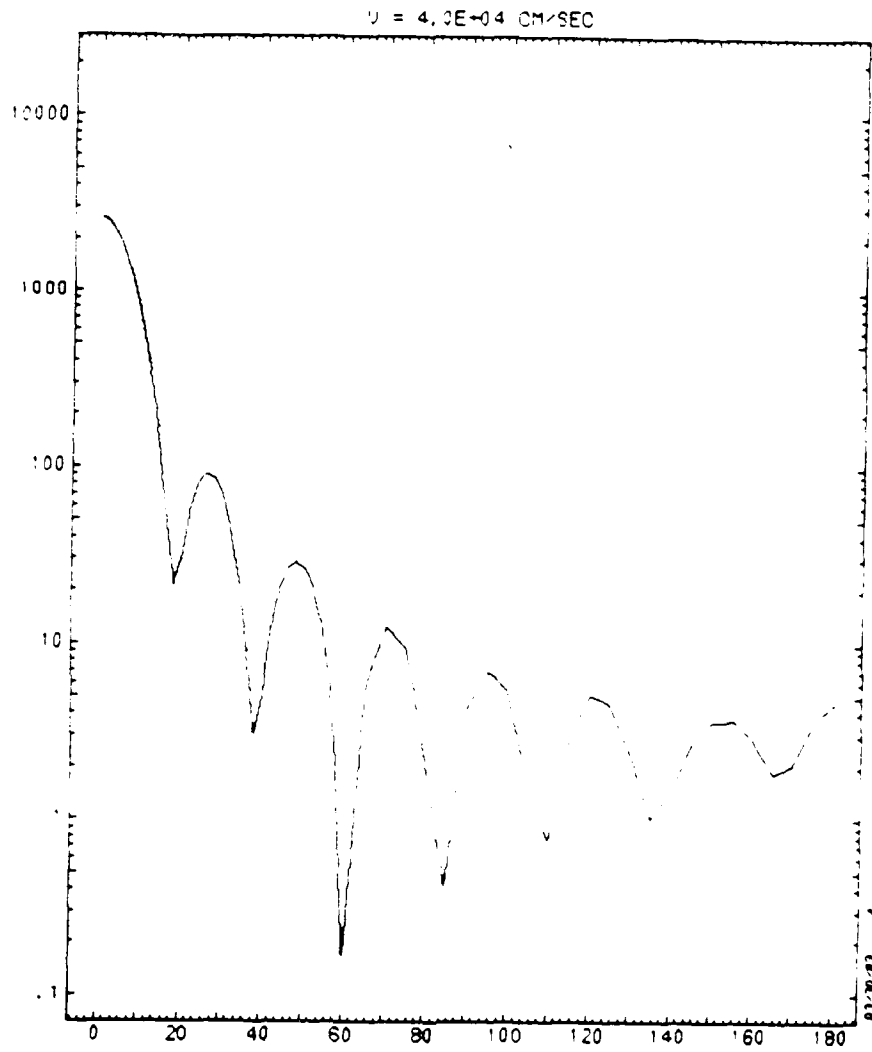
HELIUM - OXYGEN DIFFERENTIAL CROSS SECTION



HELIUM - H₂O DIFFERENTIAL CROSS SECTION

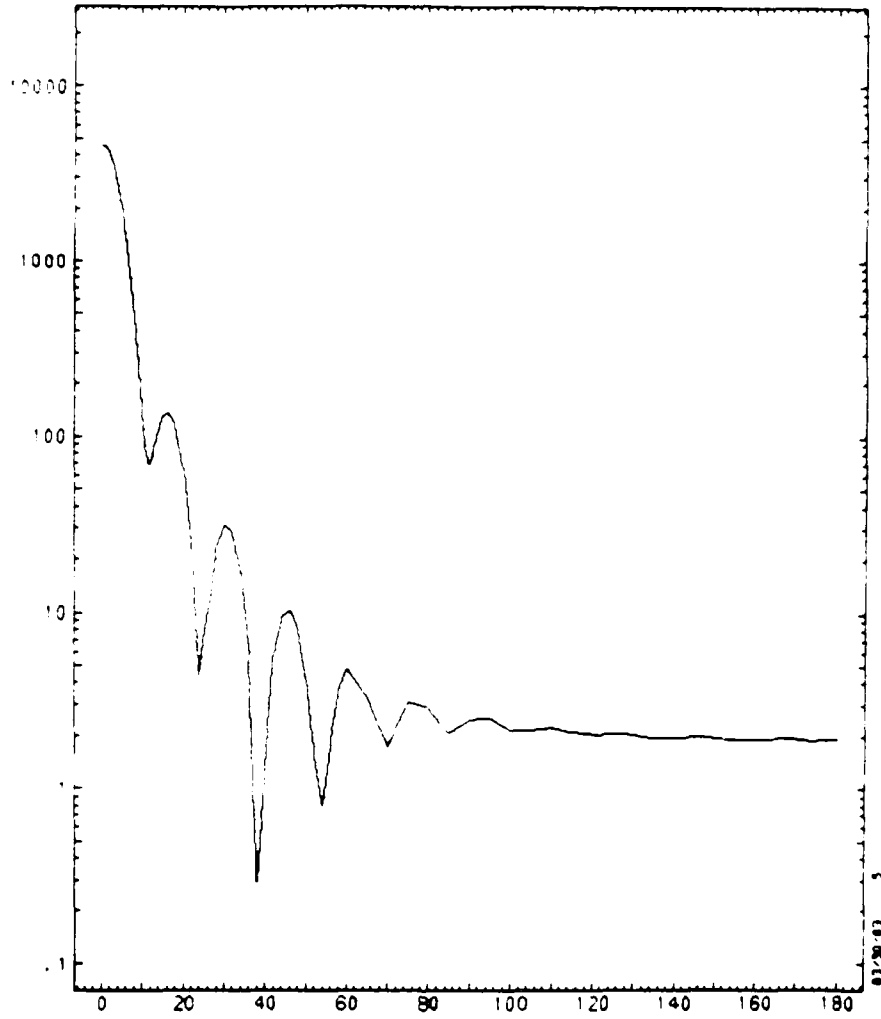


HELIUM - H2O DIFFERENTIAL CROSS SECTION

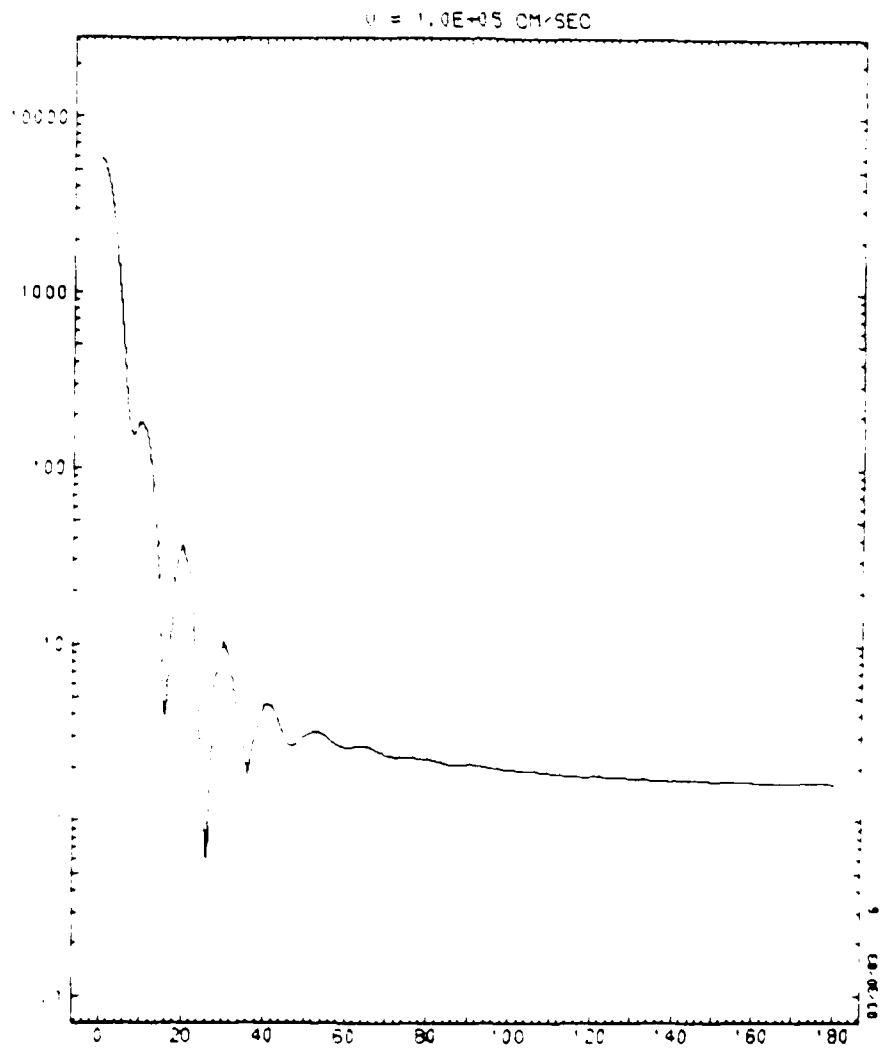


HELIUM - H2O DIFFERENTIAL CROSS SECTION

$U = 6.5E-14$ CM-SEC

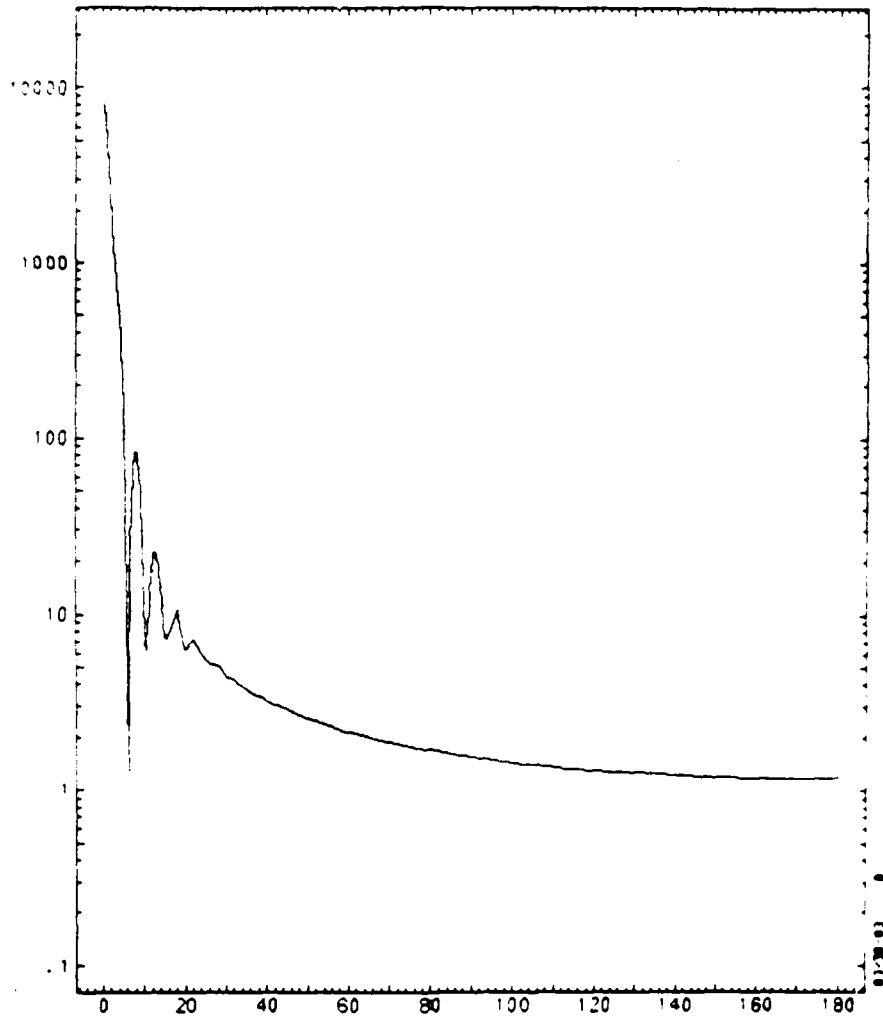


HELIUM - H2O DIFFERENTIAL CROSS SECTION



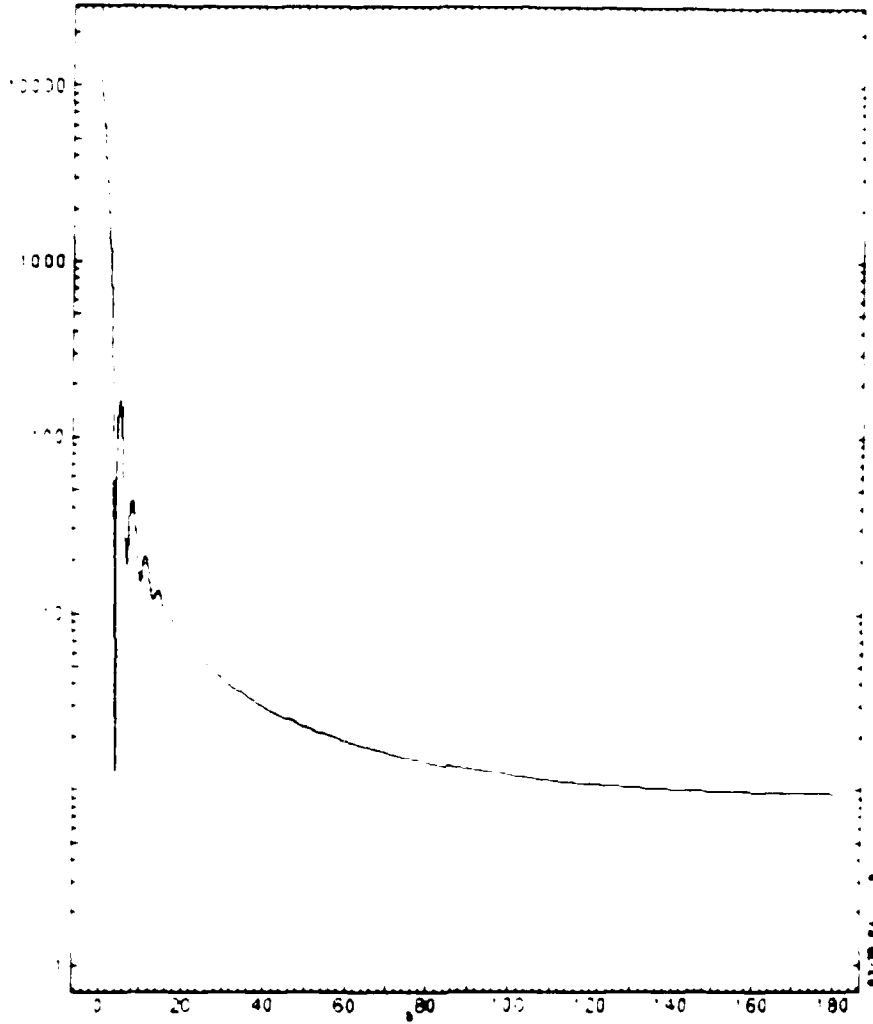
HELIUM-4 + H2O DIFFERENTIAL CROSS SECTION

$U = 2.5E-05$ CM/SEC



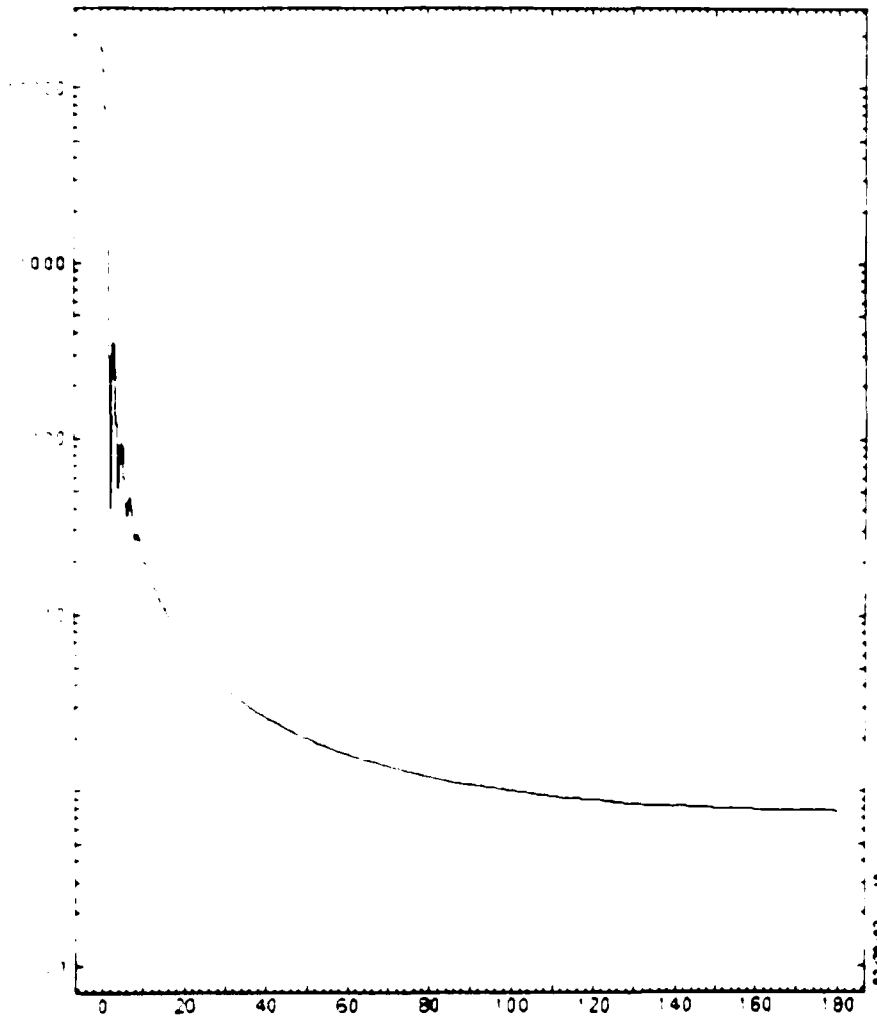
HELIUM - H2O DIFFERENTIAL CROSS SECTION

$v = 4.0 \times 10^{-5}$ CM SEC

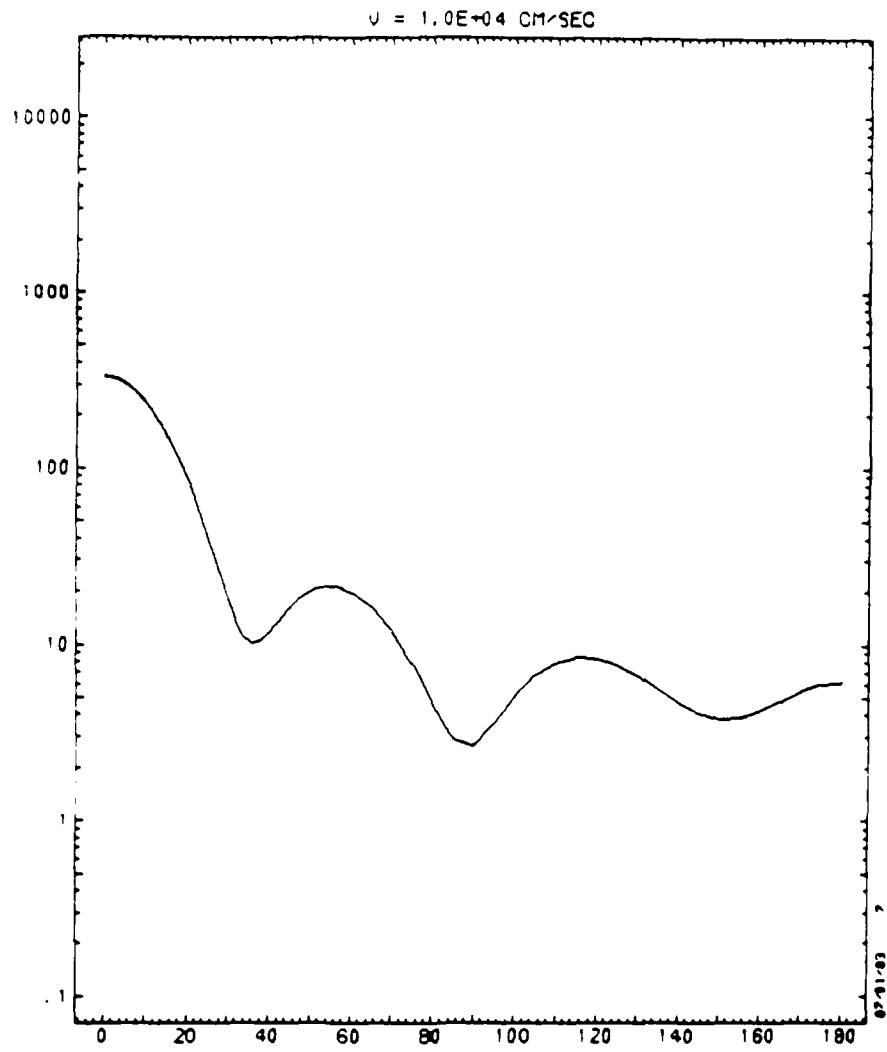


HELIUM + H₂O DIFFERENTIAL CROSS SECTION

$v = 6.5E-05$ CM-SEC

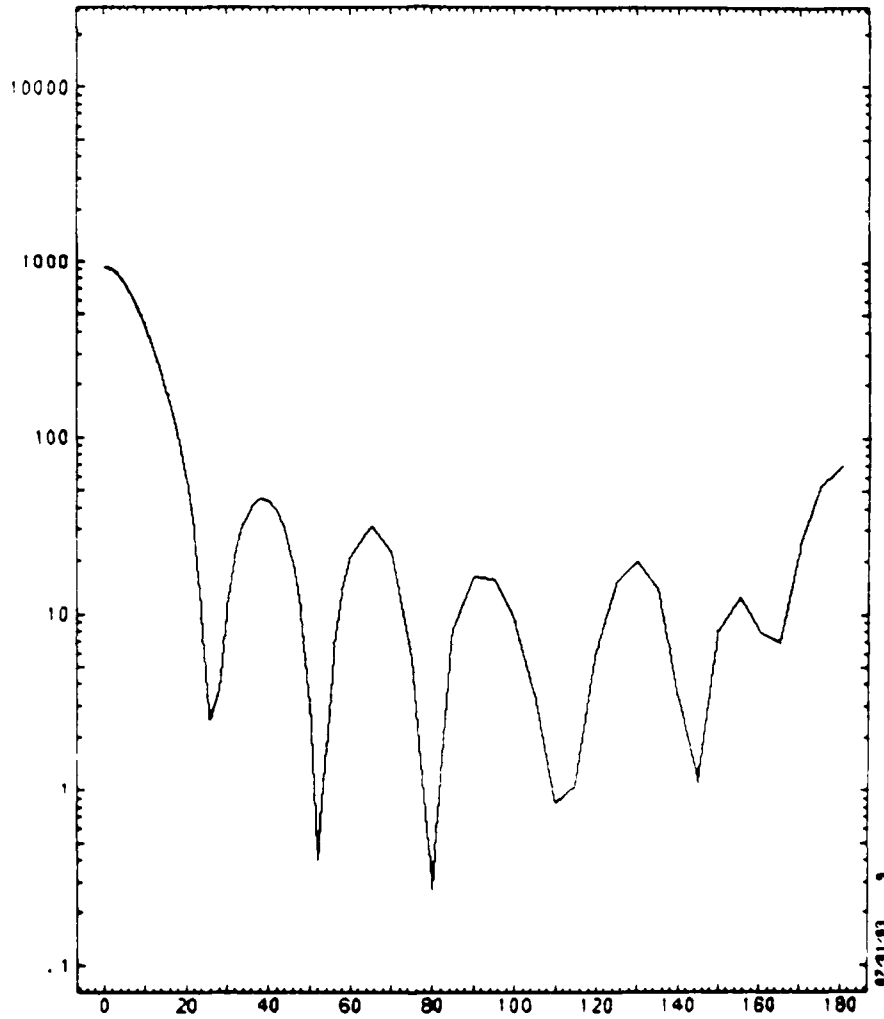


HELIUM - H2O DIFFERENTIAL CROSS SECTION

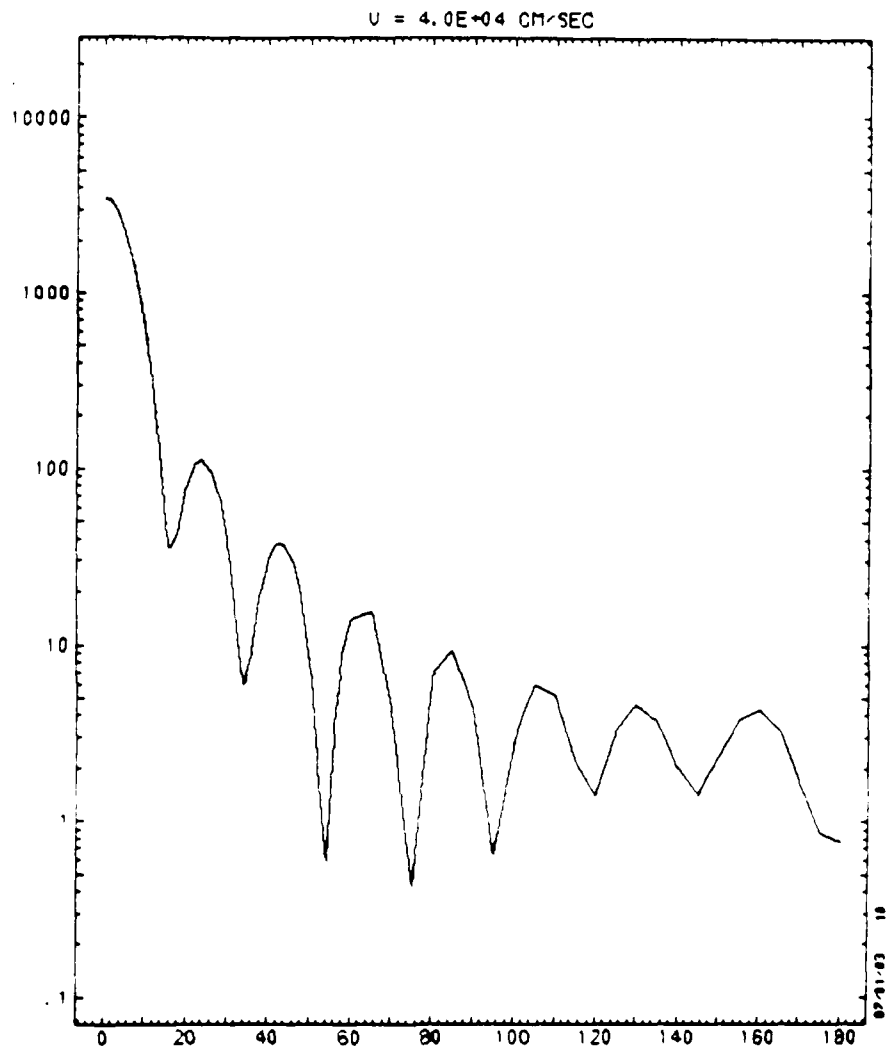


HELIUM - N2 DIFFERENTIAL CROSS SECTION

$U = 2.5E-04$ CM/SEC

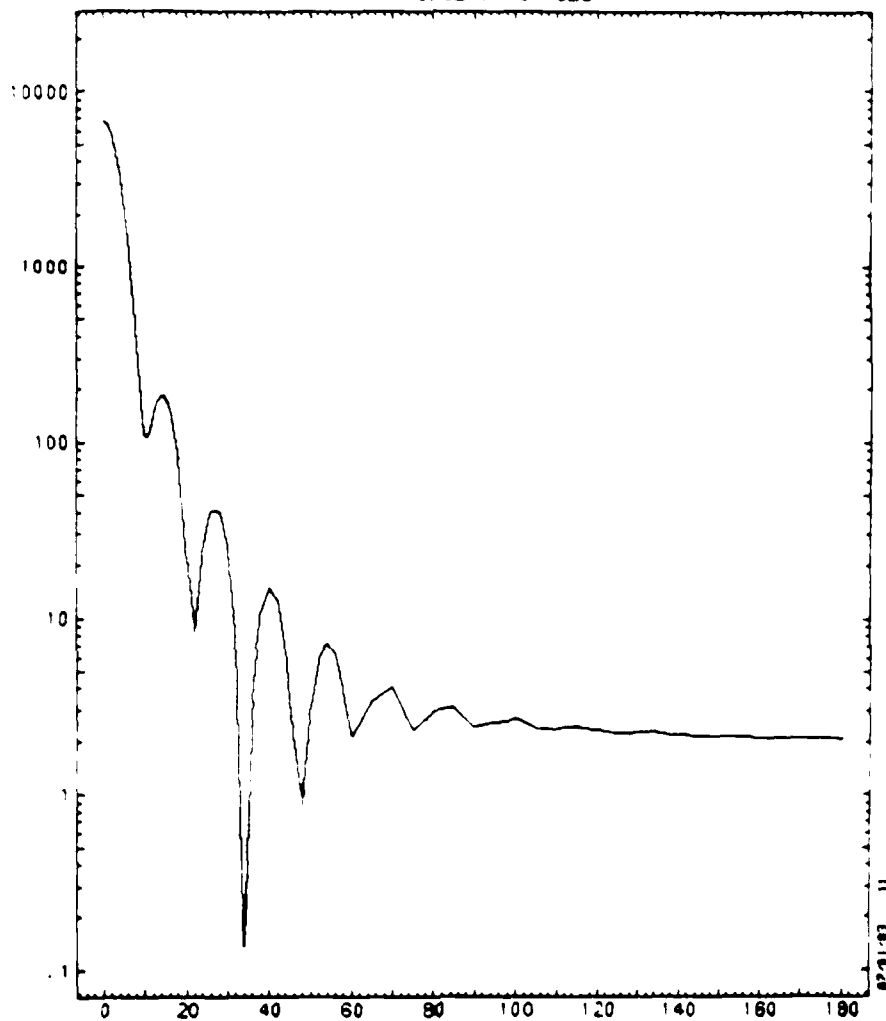


HELIUM - N2 DIFFERENTIAL CROSS SECTION



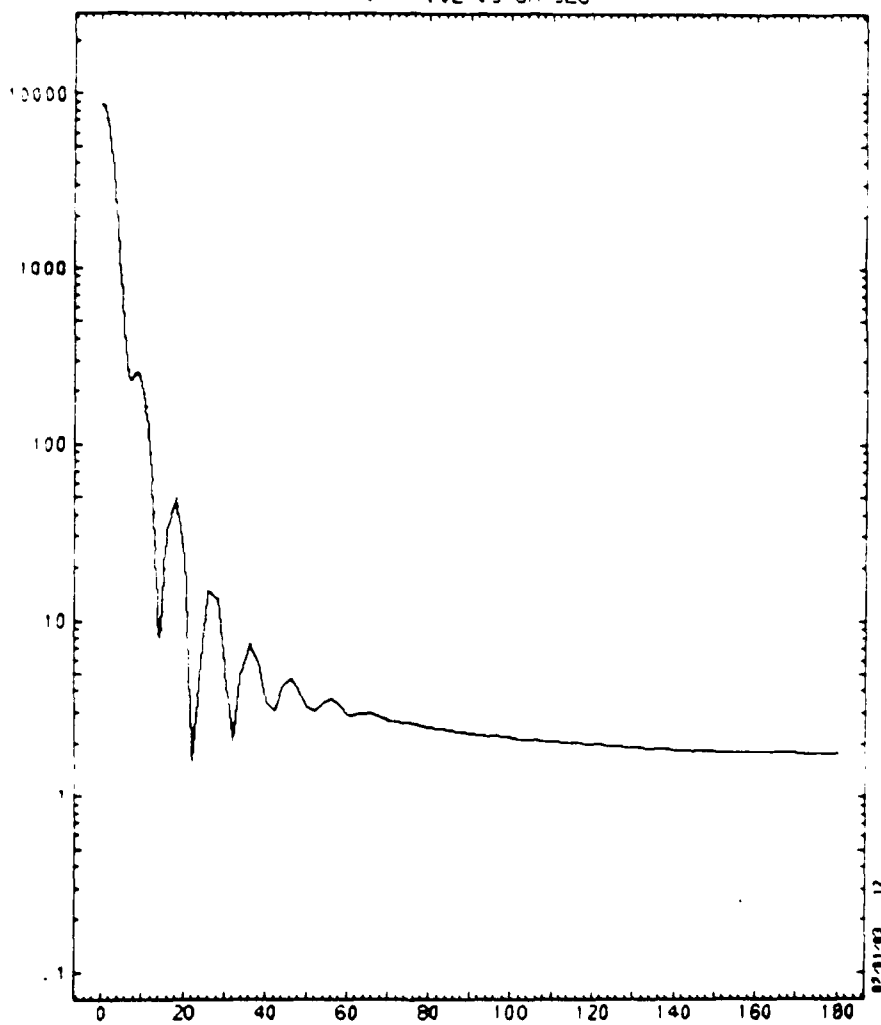
HELIUM - N2 DIFFERENTIAL CROSS SECTION

$U = 6.5E-04$ CM/SEC



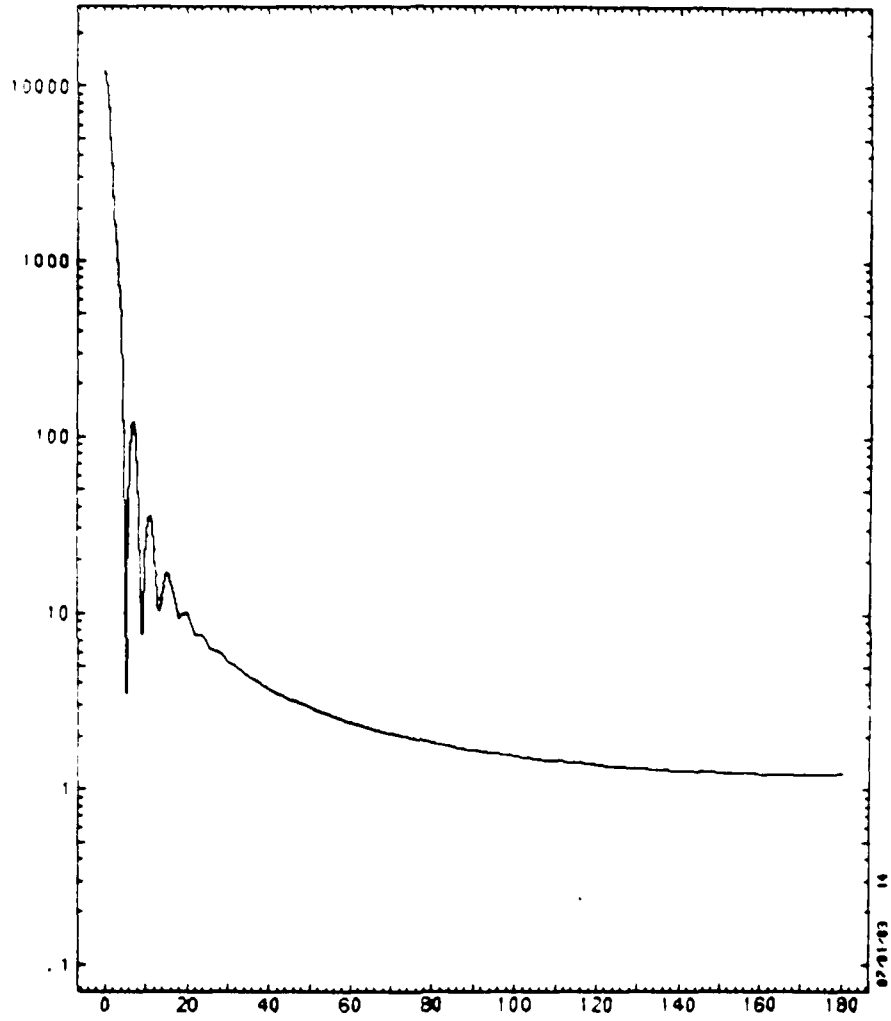
HELIUM - N2 DIFFERENTIAL CROSS SECTION

$v = 1.0E+05$ CM/SEC



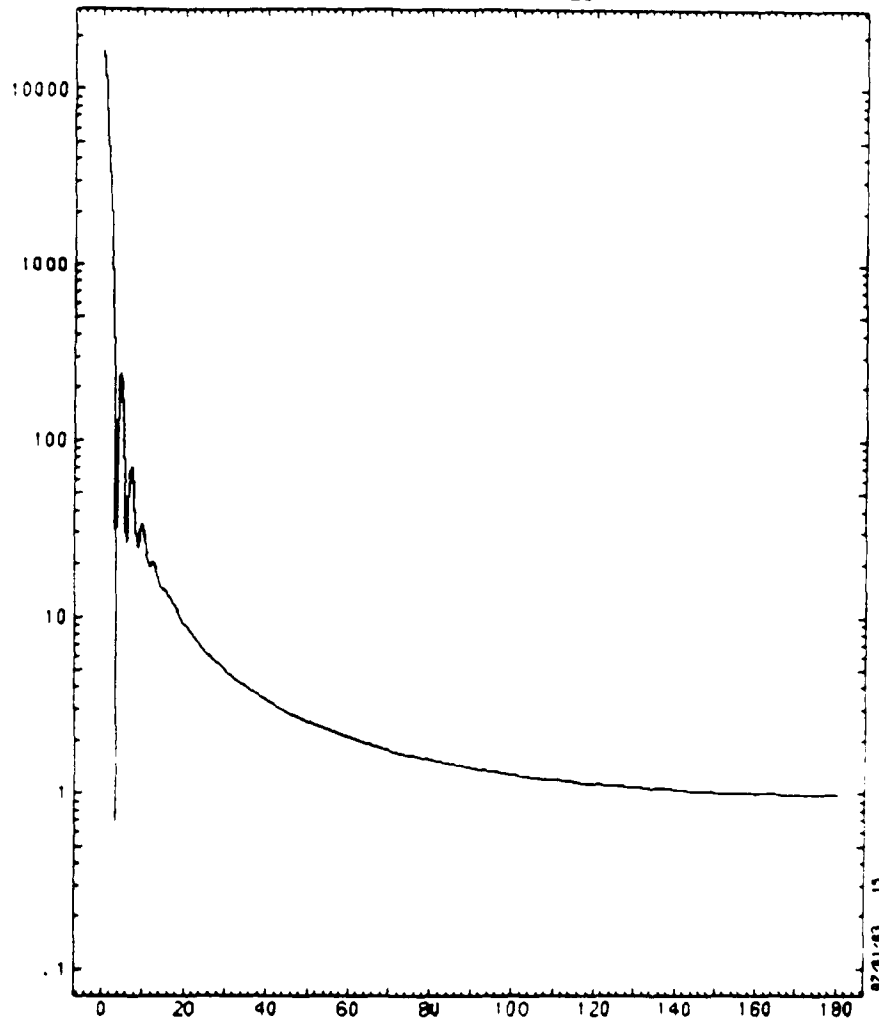
HELIUM - N2 DIFFERENTIAL CROSS SECTION

$U = 2.5E+05$ CM-SEC



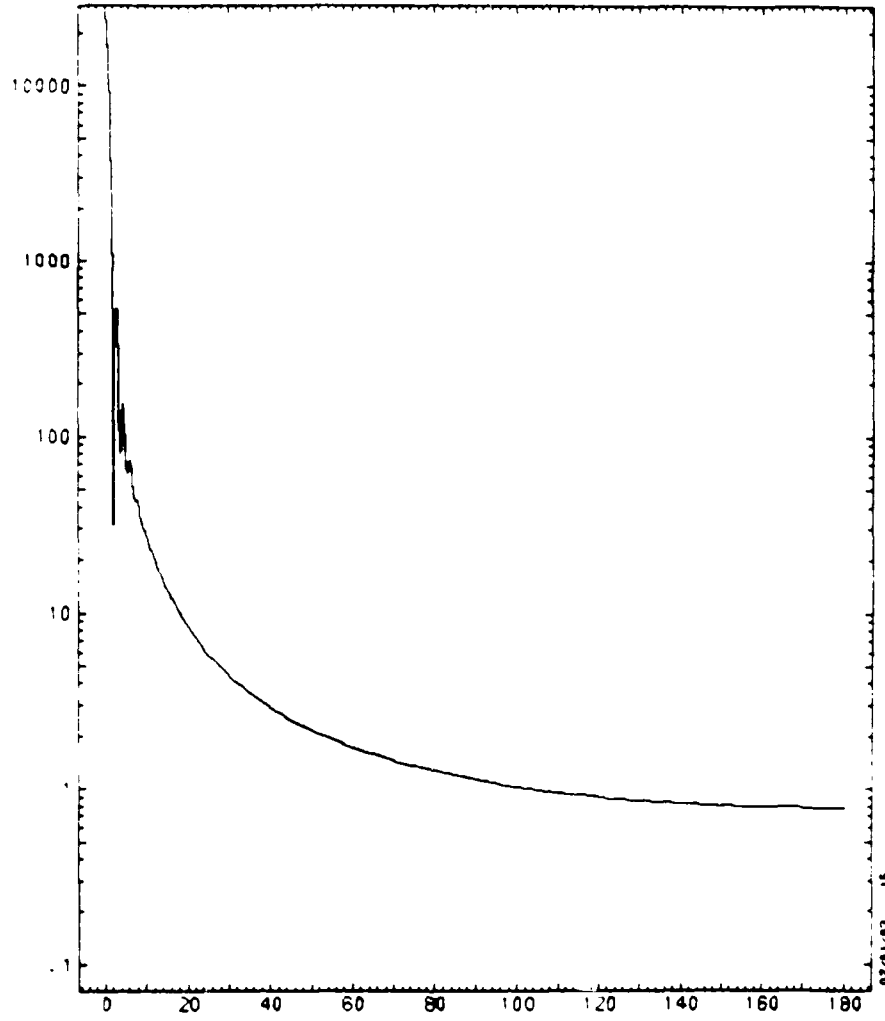
HELIUM - N2 DIFFERENTIAL CROSS SECTION

$U = 4.0E+05$ CM/SEC

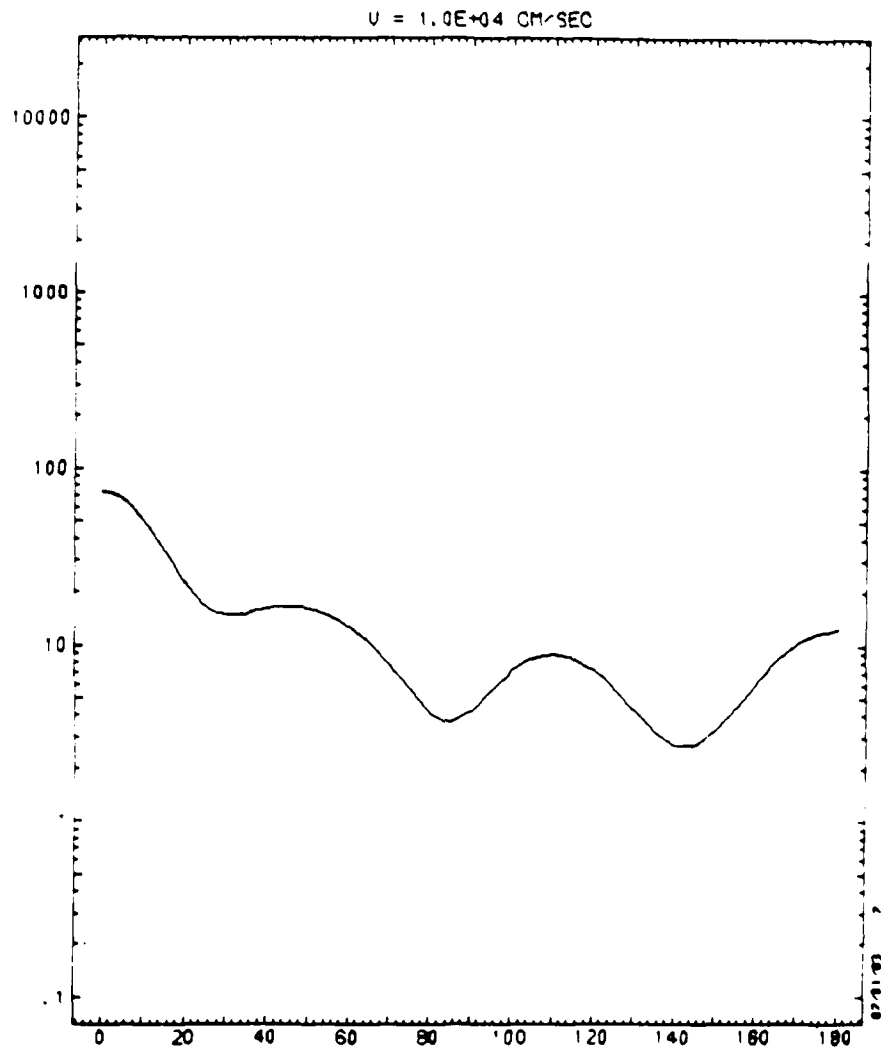


HELIUM - N2 DIFFERENTIAL CROSS SECTION

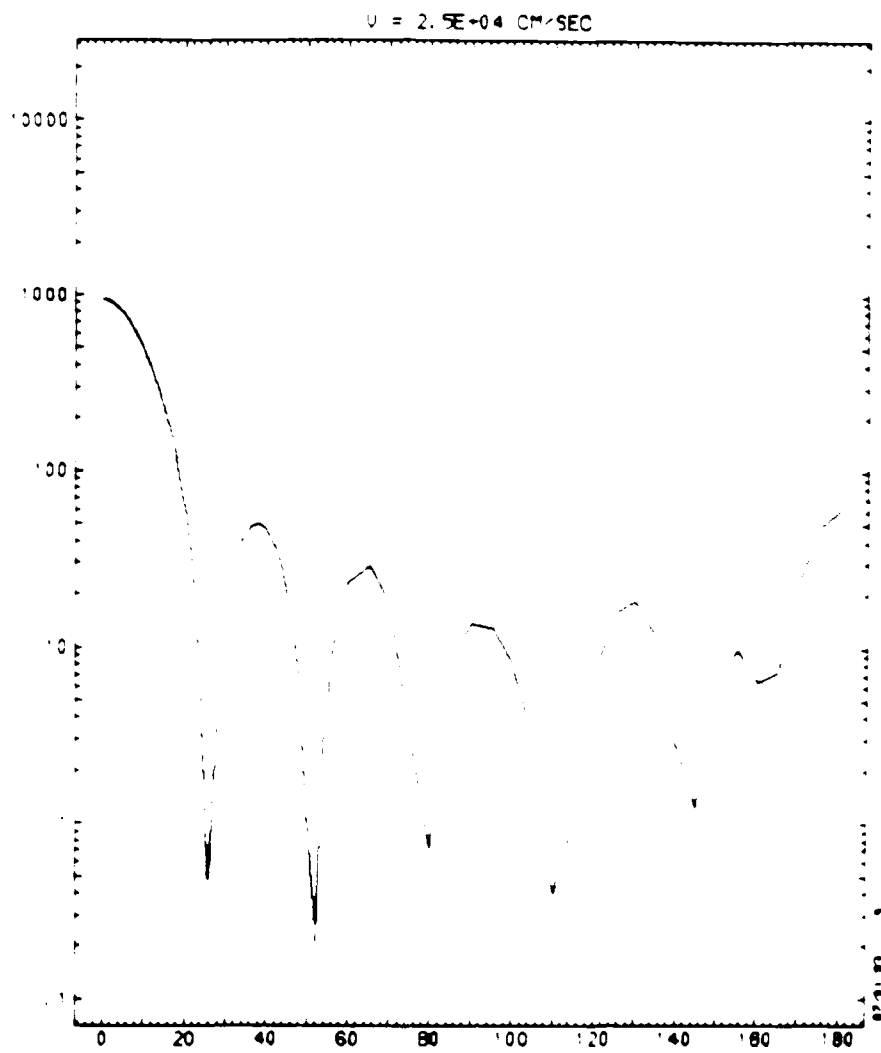
$U = 6.5E+05$ CM/SEC



HELIUM - N2 DIFFERENTIAL CROSS SECTION

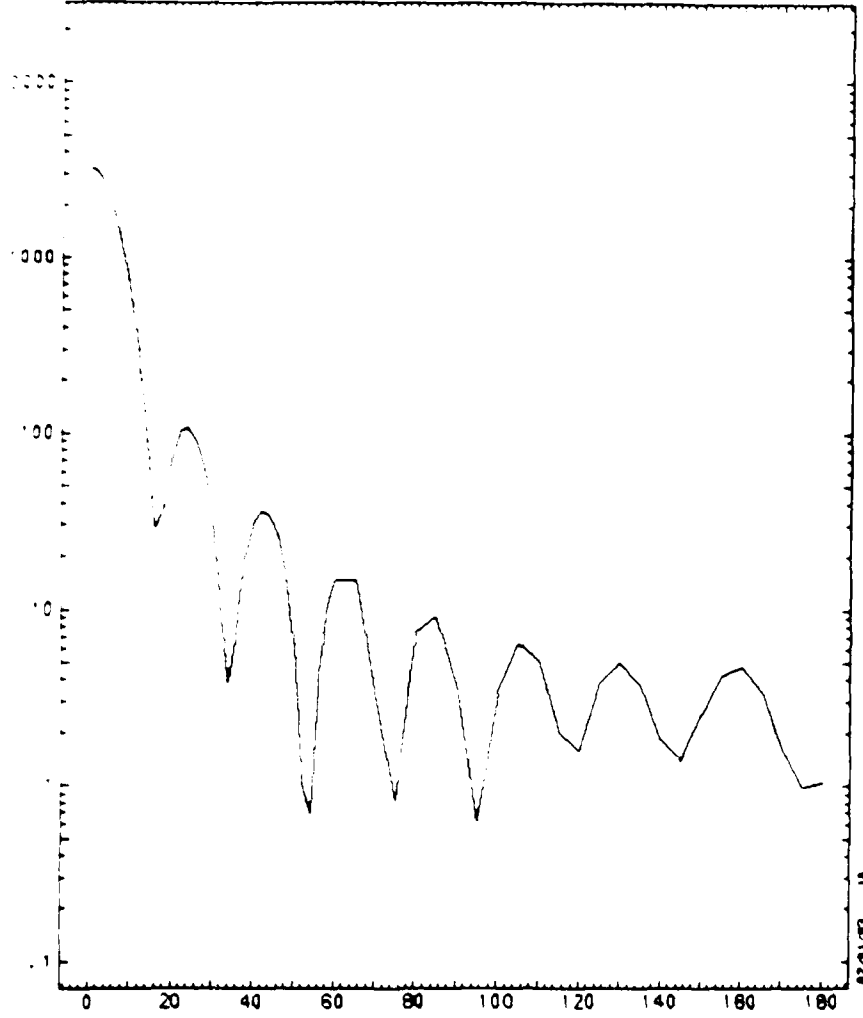


HELIUM - CO DIFFERENTIAL CROSS SECTION



HELIUM - CO DIFFERENTIAL CROSS SECTION

$v = 4.0E+04$ CM-SEC



HELIUM - CO DIFFERENTIAL CROSS SECTION

AD-A188 131

PREVENTION OF PRIMARY MIRROR CONTAMINATION BY HELIUM
PURGING (U) AEROSPACE CORP EL SEGUNDO CA CHEMISTRY AND
PHYSICS LAB R R HERN ET AL 27 FEB 87
TR-0086A(2945-88)-1 SD-TR-87-17

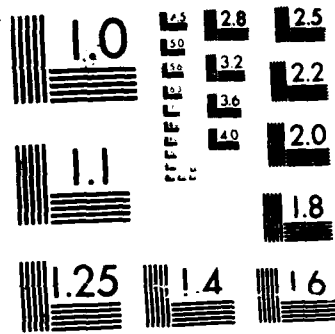
2/2

UNCLASSIFIED

F/G 17/5

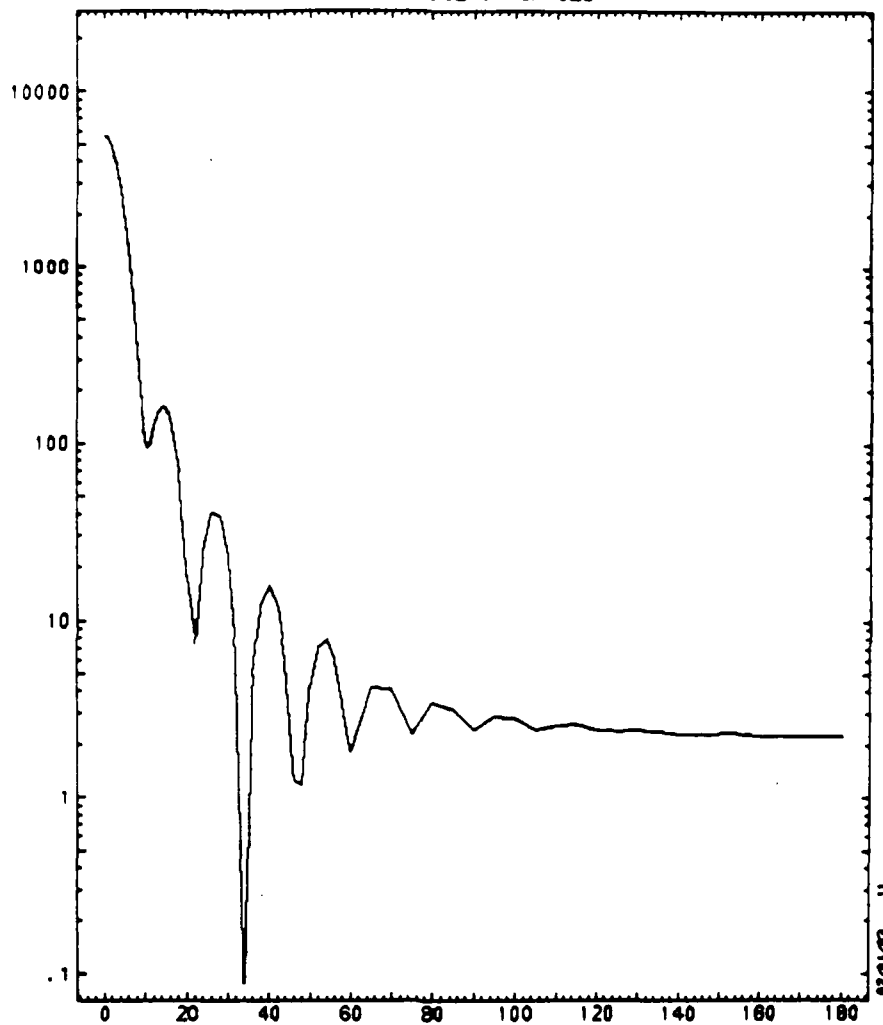
NL





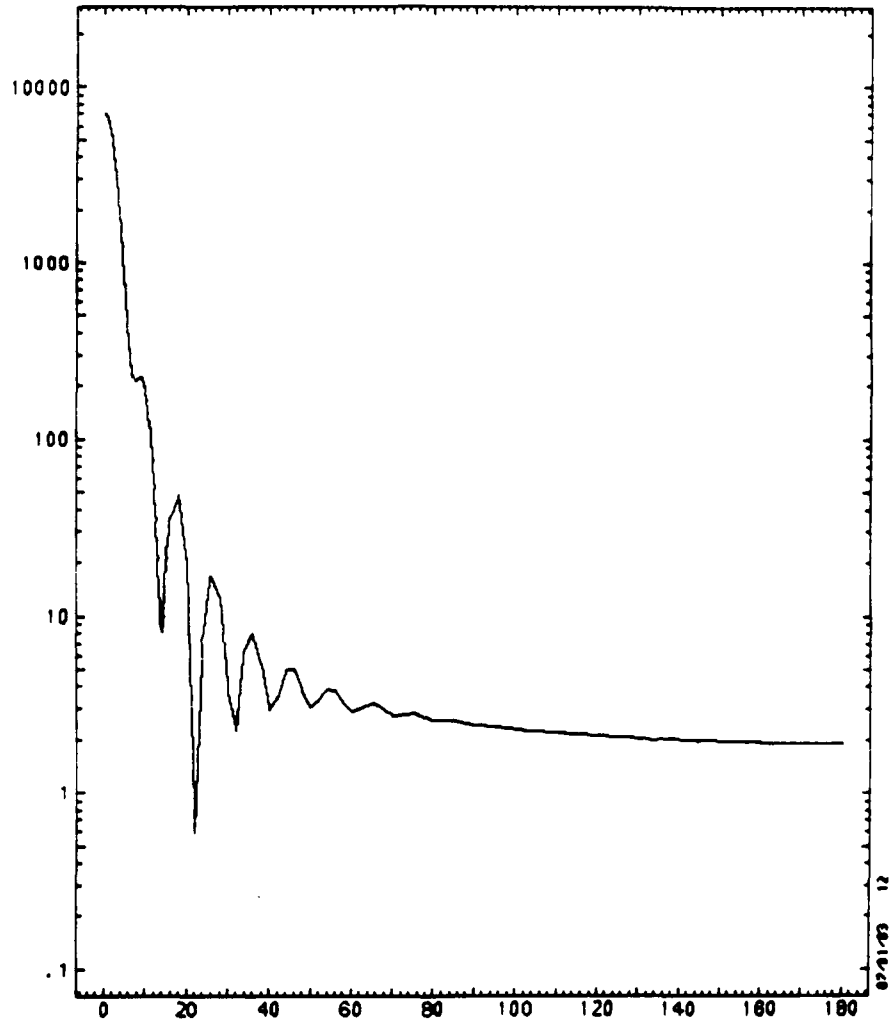
MICROCOPY RESOLUTION TEST CHART
NATIONAL BUREAU OF STANDARDS 1963-A

$U = 6.5E+04$ CM/SEC



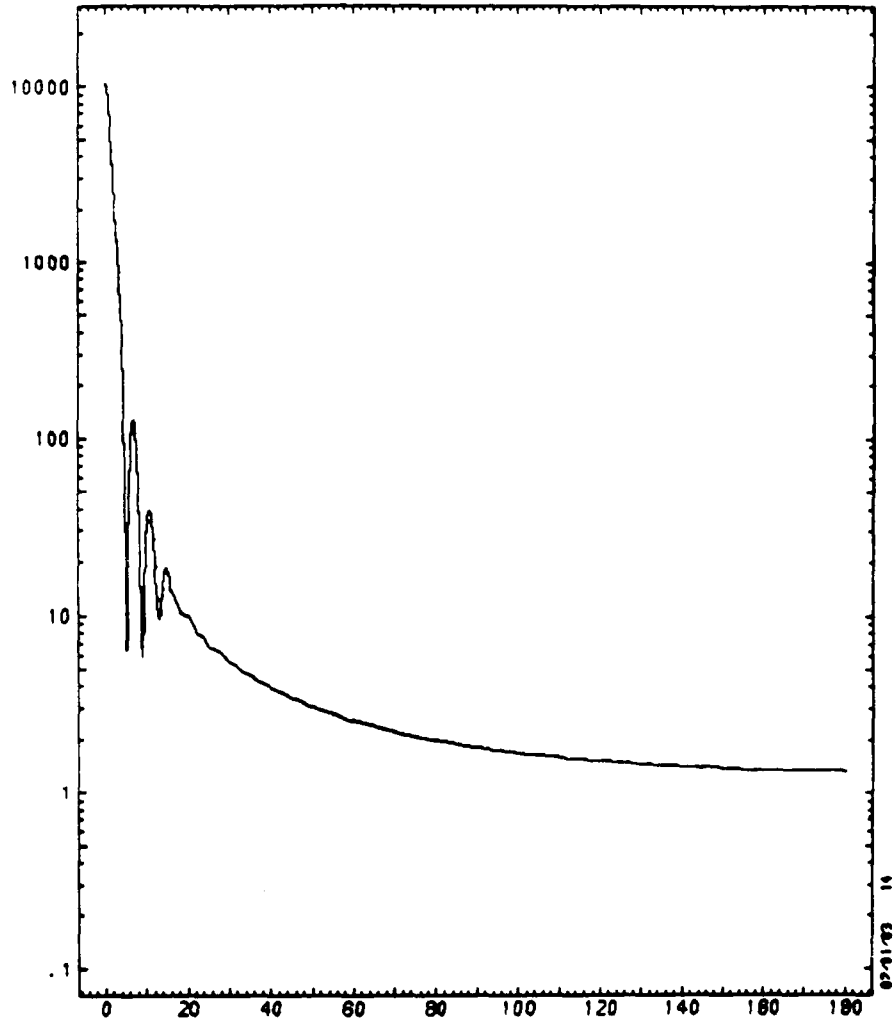
HELIUM - CO DIFFERENTIAL CROSS SECTION

$U = 1.0E+05$ CM/SEC



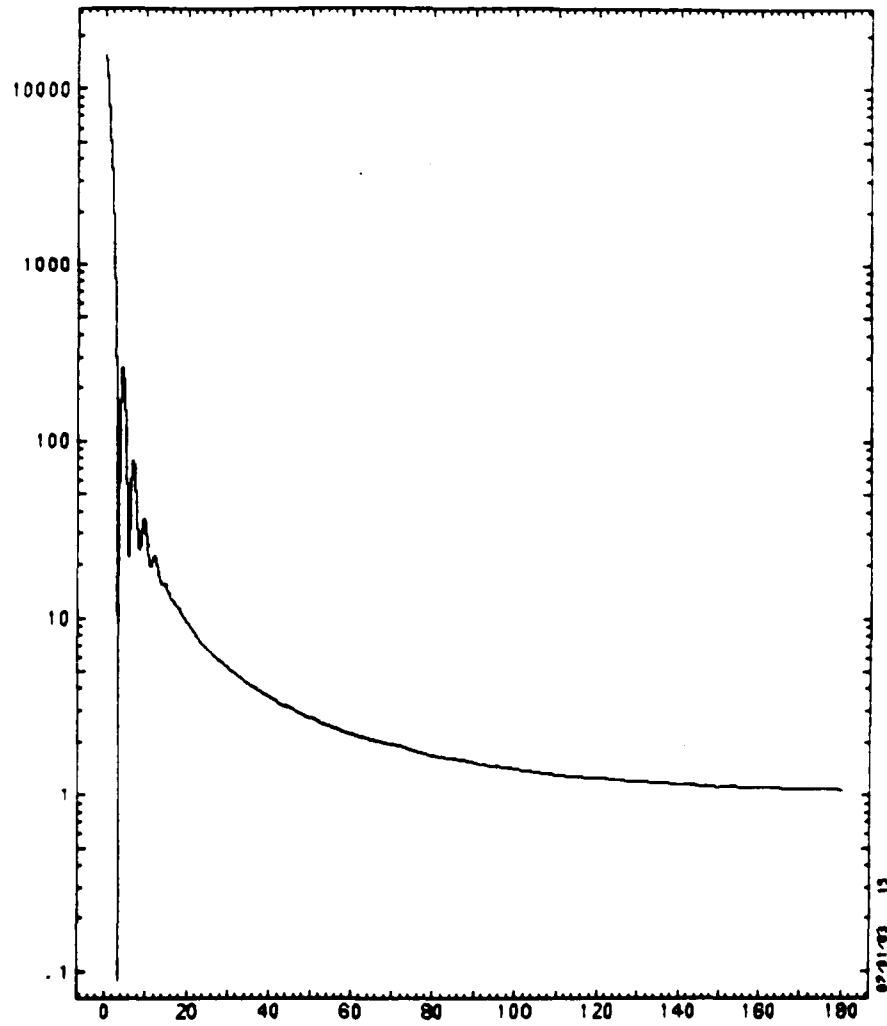
HELIUM - CO DIFFERENTIAL CROSS SECTION

$U = 2.5E+05$ CM/SEC



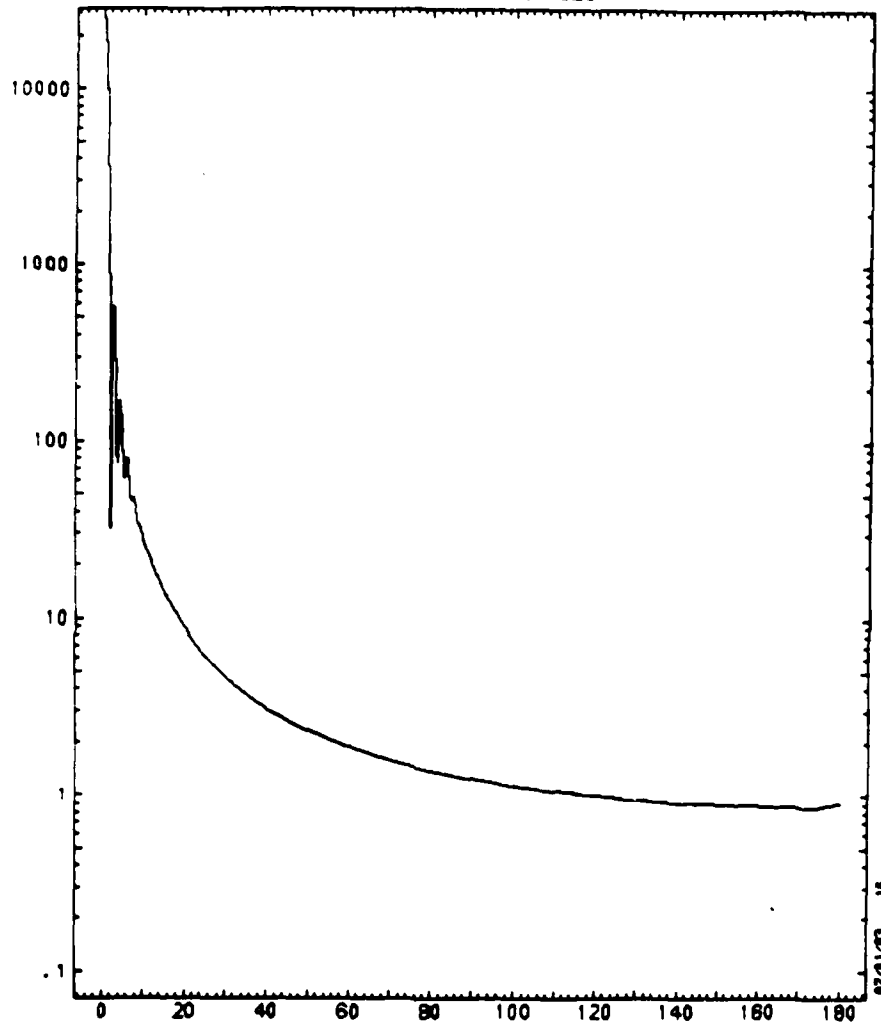
HELIUM - CO DIFFERENTIAL CROSS SECTION

U = 4.0E+05 CM/SEC

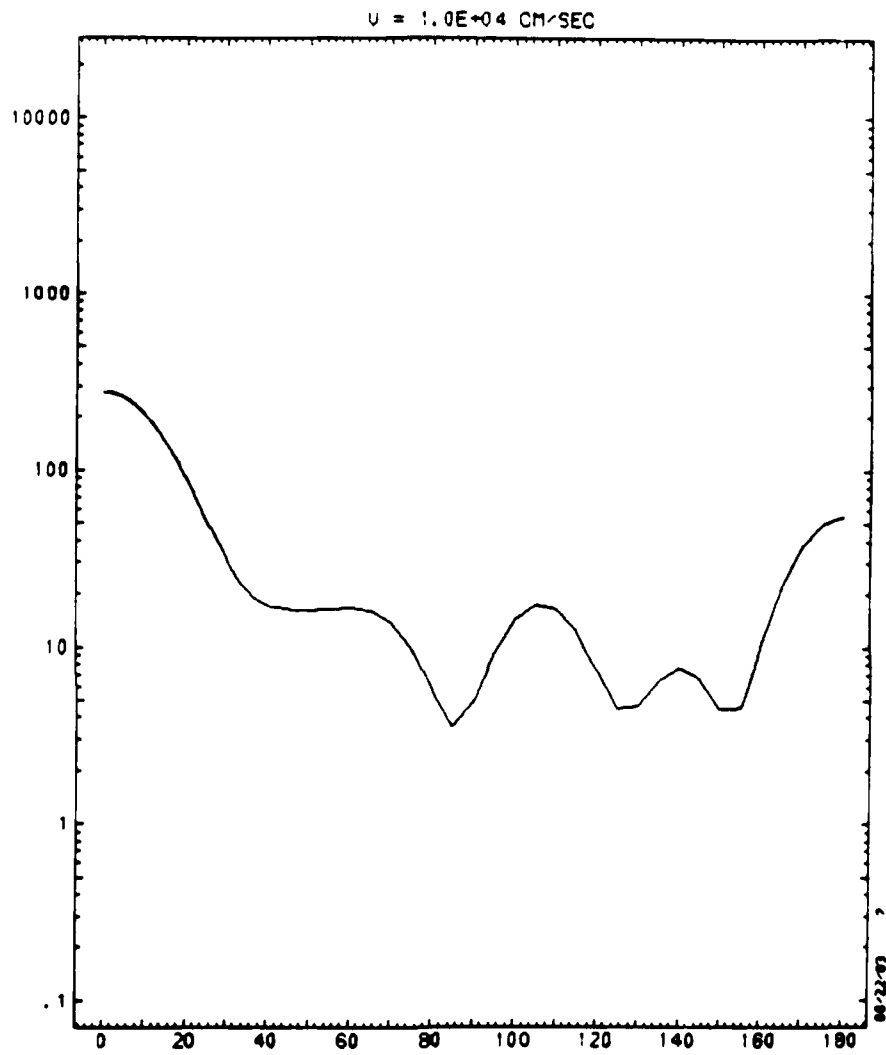


HELIUM - CO DIFFERENTIAL CROSS SECTION

$U = 6.5E+05$ CM/SEC

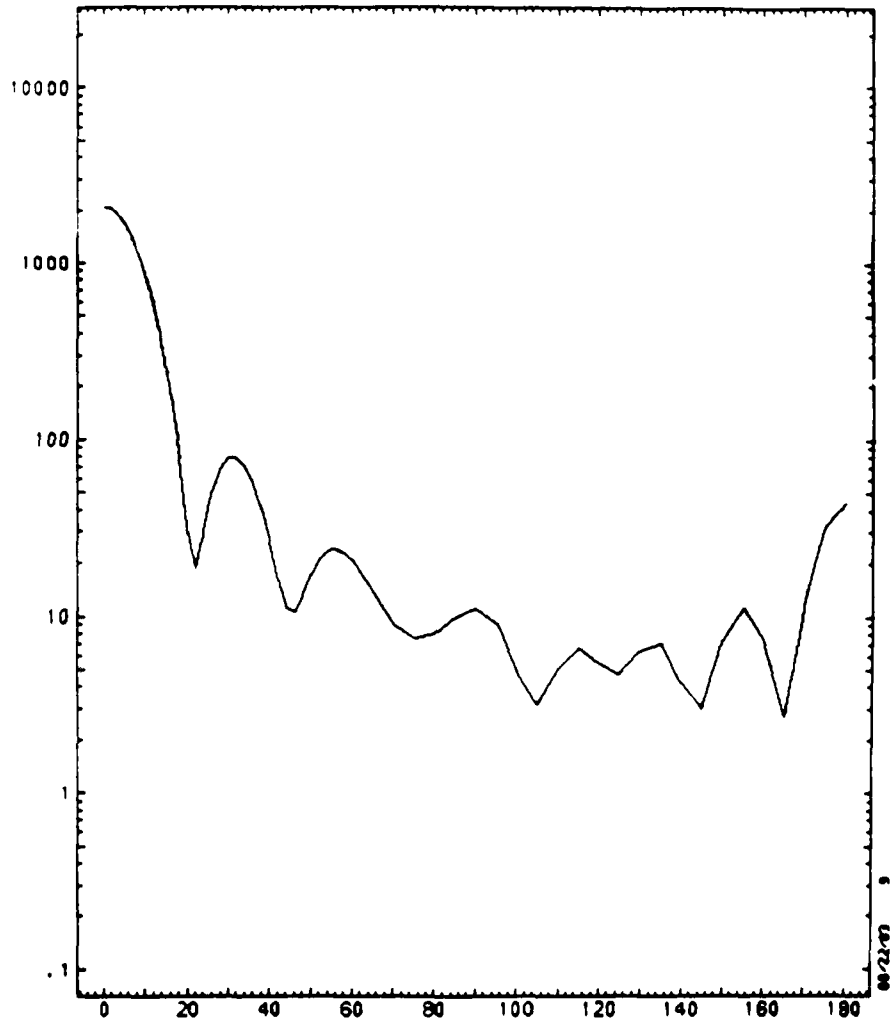


HELIUM - CO DIFFERENTIAL CROSS SECTION



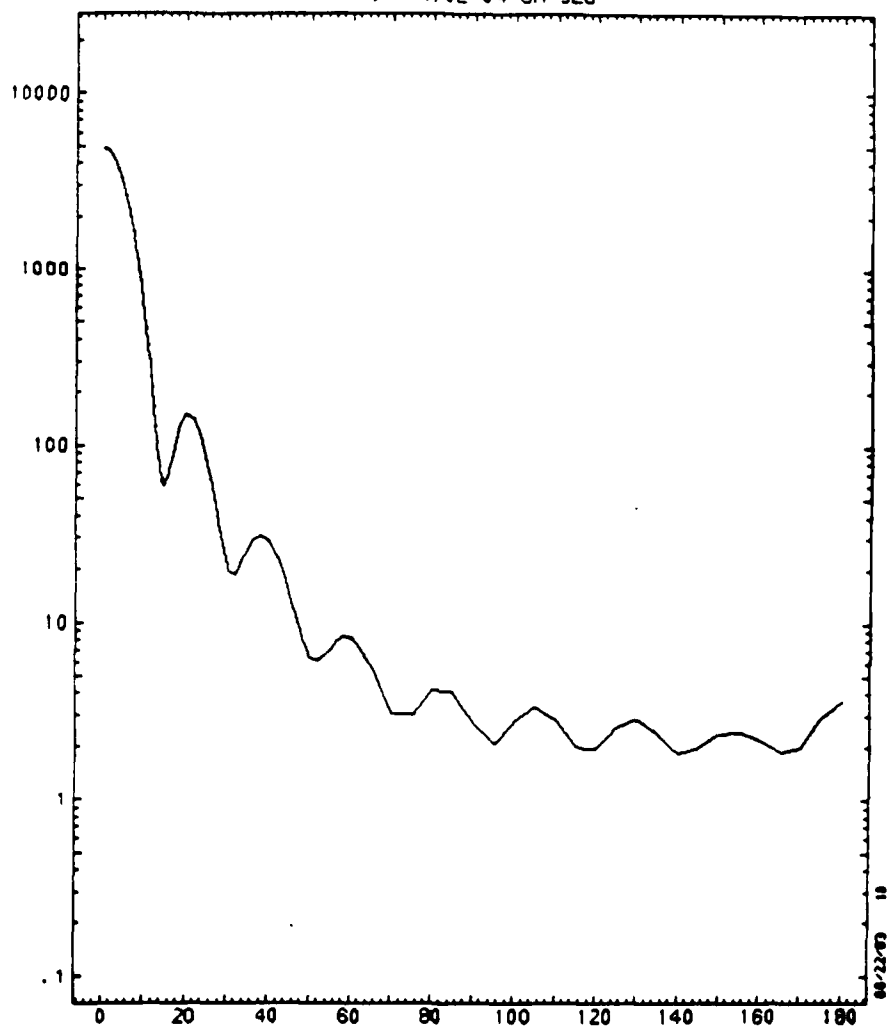
HELIUM - CO2 DIFFERENTIAL CROSS SECTION

$U = 2.5E-04$ CM/SEC



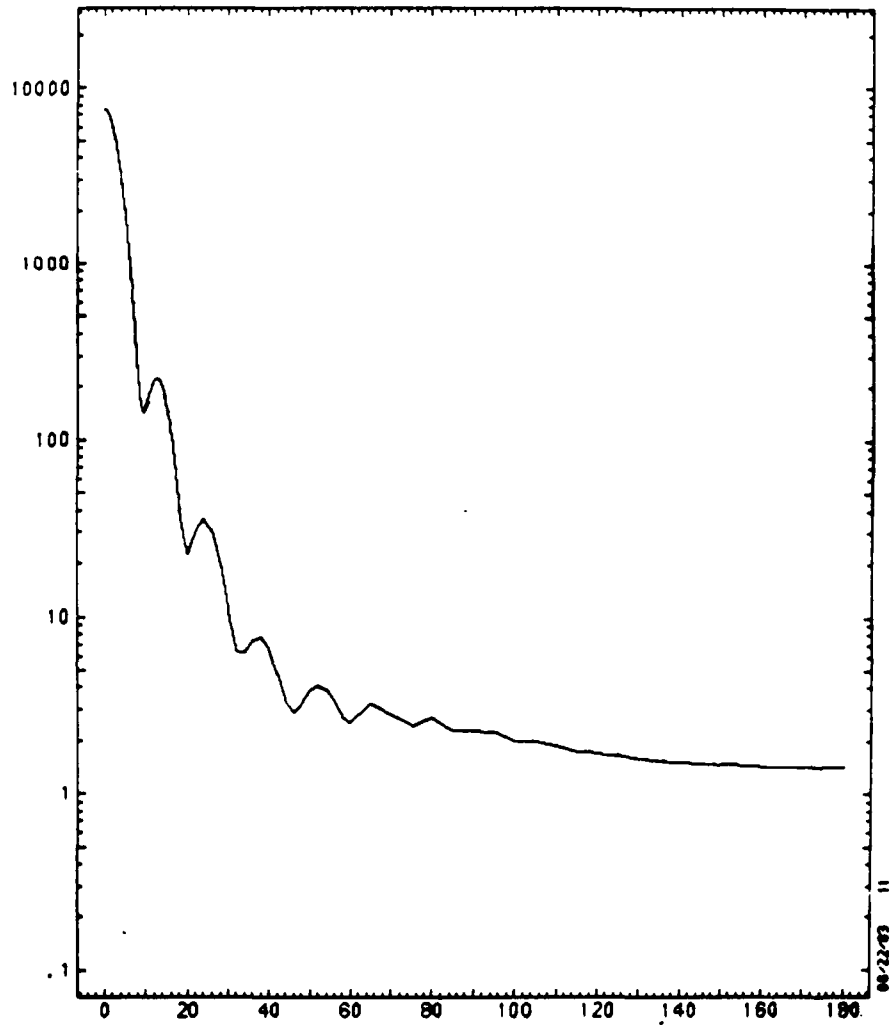
HELIUM - CO2 DIFFERENTIAL CROSS SECTION

$U = 4.0E+04$ CM/SEC



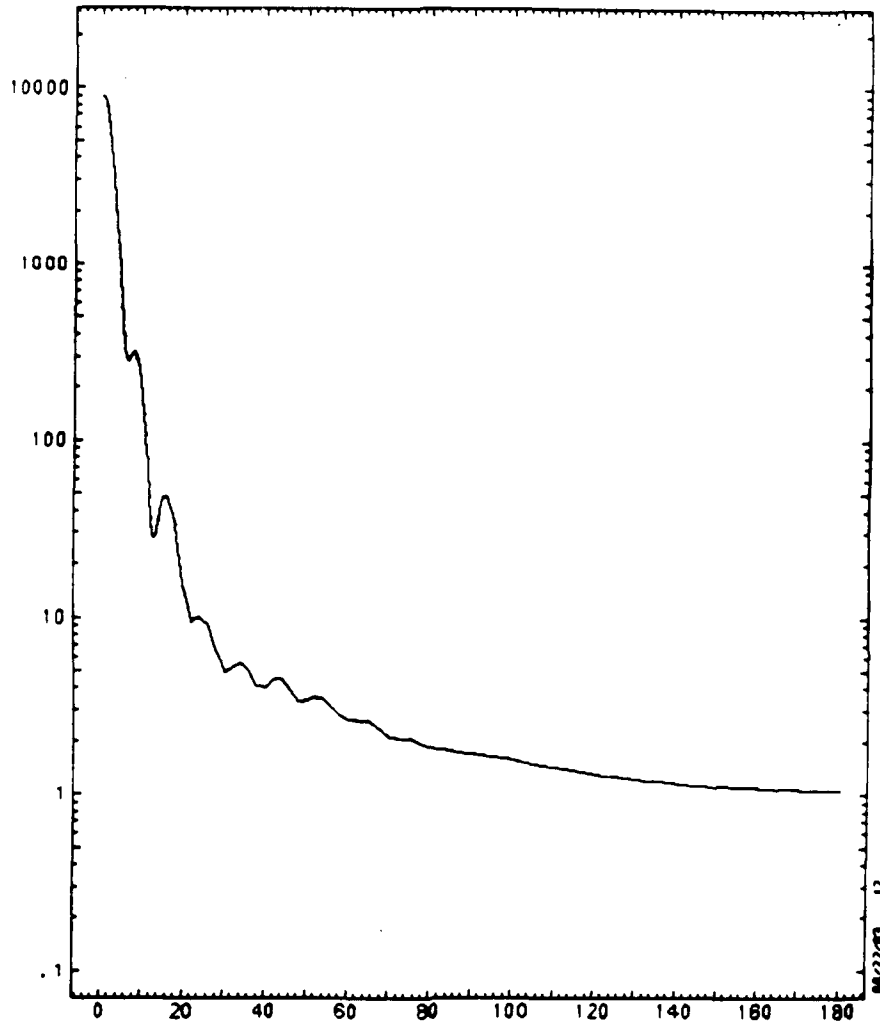
HELIUM - CO2 DIFFERENTIAL CROSS SECTION

$U = 6.5E+04$ CM/SEC



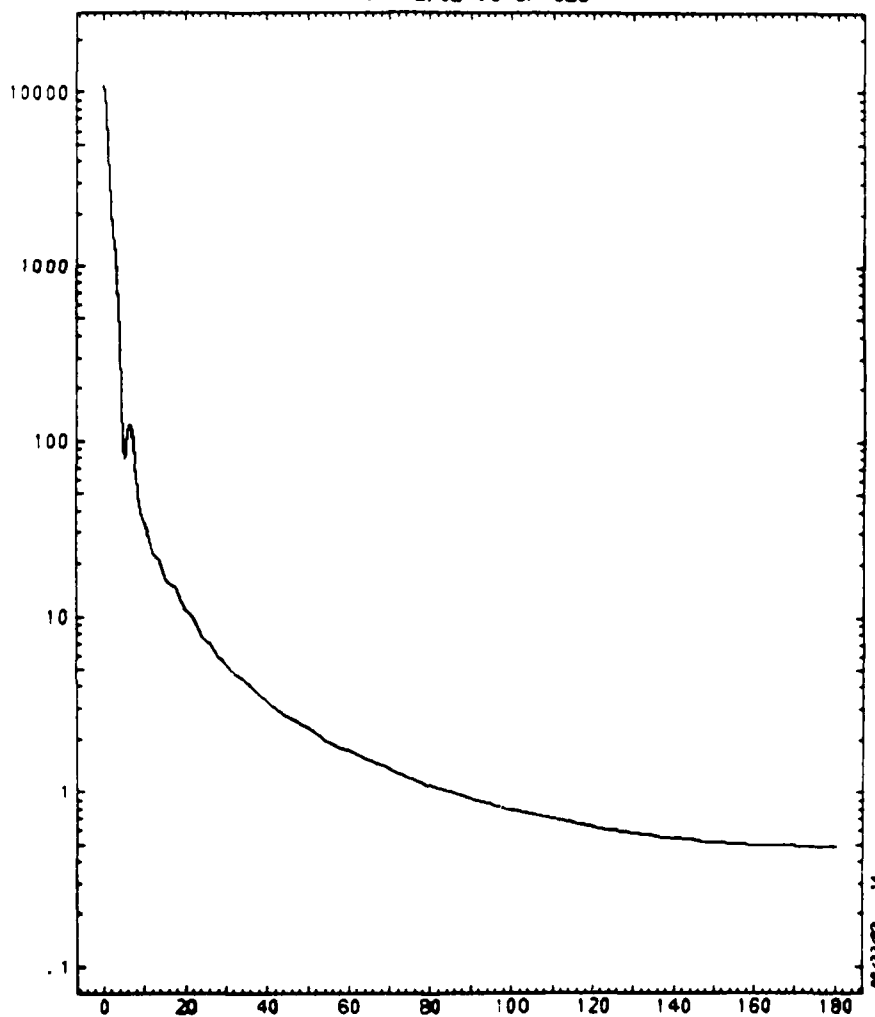
HELIUM - CO2 DIFFERENTIAL CROSS SECTION

$U = 1.0E-05$ CM-SEC

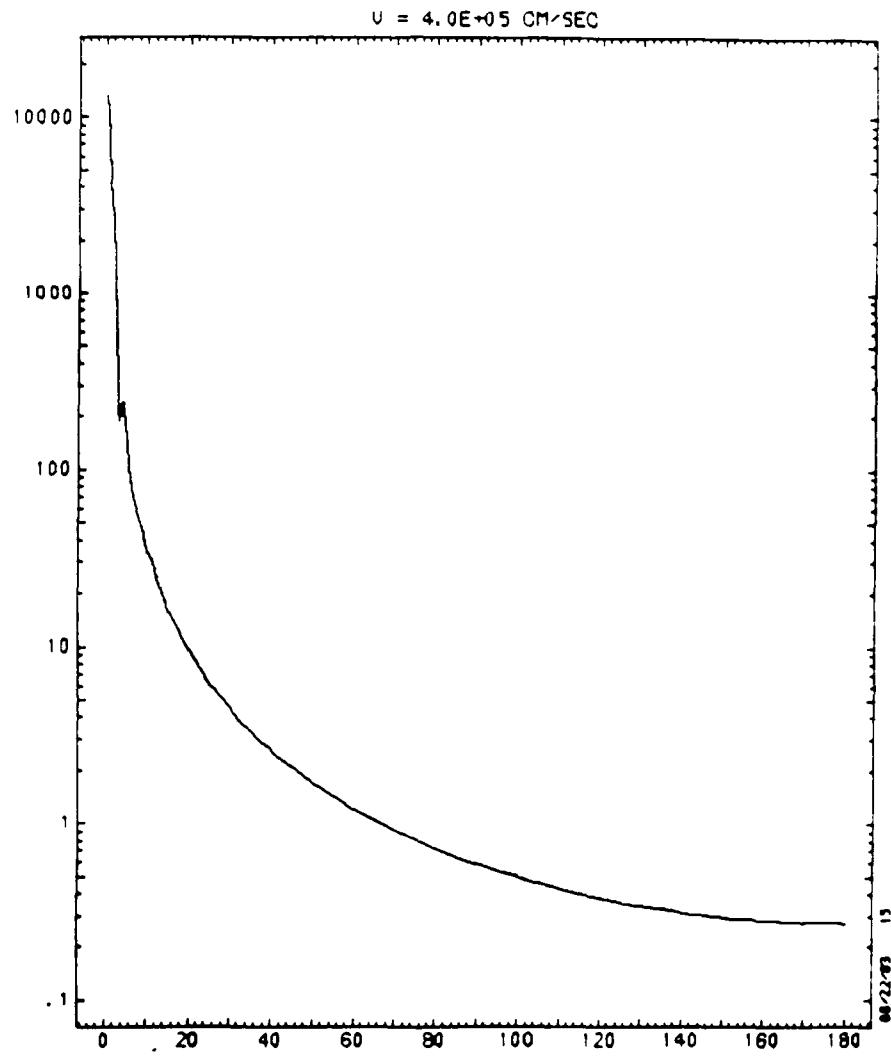


HELIUM - CO2 DIFFERENTIAL CROSS SECTION

$U = 2.5 \times 10^{-5}$ CM/SEC

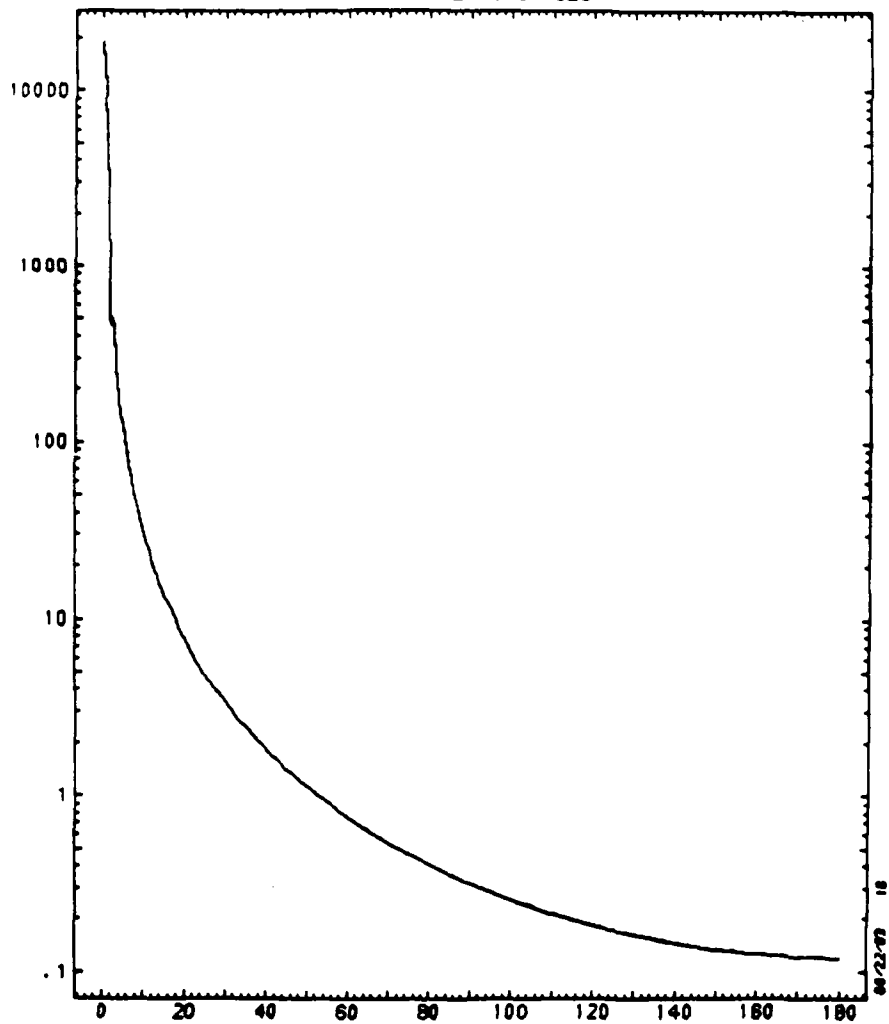


HELIUM - CO2 DIFFERENTIAL CROSS SECTION



HELIUM - CO2 DIFFERENTIAL CROSS SECTION

$U = 6.5E-05$ CM/SEC



HELIUM - CO2 DIFFERENTIAL CROSS SECTION

LABORATORY OPERATIONS

The Aerospace Corporation functions as an "architect-engineer" for national security projects, specializing in advanced military space systems. Providing research support, the corporation's Laboratory Operations conducts experimental and theoretical investigations that focus on the application of scientific and technical advances to such systems. Vital to the success of these investigations is the technical staff's wide-ranging expertise and its ability to stay current with new developments. This expertise is enhanced by a research program aimed at dealing with the many problems associated with rapidly evolving space systems. Contributing their capabilities to the research effort are these individual laboratories:

Aerophysics Laboratory: Launch vehicle and reentry fluid mechanics, heat transfer and flight dynamics; chemical and electric propulsion, propellant chemistry, chemical dynamics, environmental chemistry, trace detection; spacecraft structural mechanics, contamination, thermal and structural control; high temperature thermomechanics, gas kinetics and radiation; cw and pulsed chemical and excimer laser development including chemical kinetics, spectroscopy, optical resonators, beam control, atmospheric propagation, laser effects and countermeasures.

Chemistry and Physics Laboratory: Atmospheric chemical reactions, atmospheric optics, light scattering, state-specific chemical reactions and radiative signatures of missile plumes, sensor out-of-field-of-view rejection, applied laser spectroscopy, laser chemistry, laser optoelectronics, solar cell physics, battery electrochemistry, space vacuum and radiation effects on materials, lubrication and surface phenomena, thermionic emission, photosensitive materials and detectors, atomic frequency standards, and environmental chemistry.

Computer Science Laboratory: Program verification, program translation, performance-sensitive system design, distributed architectures for spaceborne computers, fault-tolerant computer systems, artificial intelligence, microelectronics applications, communication protocols, and computer security.

Electronics Research Laboratory: Microelectronics, solid-state device physics, compound semiconductors, radiation hardening; electro-optics, quantum electronics, solid-state lasers, optical propagation and communications; microwave semiconductor devices, microwave/millimeter wave measurements, diagnostics and radiometry, microwave/millimeter wave thermionic devices; atomic time and frequency standards; antennas, rf systems, electromagnetic propagation phenomena, space communication systems.

Materials Sciences Laboratory: Development of new materials: metals, alloys, ceramics, polymers and their composites, and new forms of carbon; non-destructive evaluation, component failure analysis and reliability; fracture mechanics and stress corrosion; analysis and evaluation of materials at cryogenic and elevated temperatures as well as in space and enemy-induced environments.

Space Sciences Laboratory: Magnetospheric, auroral and cosmic ray physics, wave-particle interactions, magnetospheric plasma waves; atmospheric and ionospheric physics, density and composition of the upper atmosphere, remote sensing using atmospheric radiation; solar physics, infrared astronomy, infrared signature analysis; effects of solar activity, magnetic storms and nuclear explosions on the earth's atmosphere, ionosphere and magnetosphere; effects of electromagnetic and particulate radiations on space systems; space instrumentation.

FWD

6-87

DTIC